2017

Variable Structure Feedback Control with Application to Spacecraft with Small Thrust Propulsion Systems

Samuel J. Kitchen-McKinley

Variable Structure Feedback Control with Application to Spacecraft with Small Thrust Propulsion Systems

by

Samuel J. Kitchen-McKinley

A Dissertation Submitted to the Physical Sciences Department

in Partial Fulfillment of the Requirements

for the Degree of

DOCTOR OF PHILOSOPHY

(Engineering Physics)

Embry-Riddle Aeronautical University

Daytona Beach, FL 32114

2017

Variable Structure Feedback Control with Application to Spacecraft with Small Thrust Propulsion Systems

By

Samuel J. Kitchen-McKinley

This Dissertation was prepared under the direction of the candidate's Dissertation Committee Chair, Dr. Sergey V. Drakunov and has been approved by the members of his dissertation committee. It was submitted to the College of Arts and Sciences and was accepted in partial fulfillment of the requirements for the Degree of Doctor of Philosophy in Engineering Physics

Dr. Sergey V. Drakunov, Ph.D
Committee Chair

Dr. William MacKunis, Ph.D
Committee Member

Dr. Terry Oswalt, Ph.D
Department Chair, Physical Sciences

Dr. Stefan C. Mancas, Ph.D
Committee Member

Dr. Karen Frances Gaines, Ph.D
Dean, College of Arts and Sciences

Dr. John Hughes, Ph.D
Committee Member

Dr. Michael Hickey, Ph.D
Dean of Research and Graduate Studies

12/5/17
Date

Acknowledgments

First I would like to thank my advisor, Dr. Sergey V. Drakunov, for his support, dedication, enthusiasm, and expertise towards the subject matter and completion of my Ph.D. I would like to thank Dr. William MacKunis, Dr. Stefan C. Mancas, and Dr. John Hughes for sitting on my committee, giving their support, and helping to edit this dissertation. I would also like to thank my fellow Ph.D. students for their camaraderie and for our many existential conversations. I would like to thank Natalie for all her support and I would like my mum for her support throughout my education. Lastly, I would like to thank all my teachers and all the educational opportunities that brought me to this point.

Work in this dissertation was partially supported by NASA CIF contract for the Asteroid and Lava Tube In Situ Resource Utilization (ISRU) Prospecting Free Flyer Project and NASA SBIR/STTR Phase II grant for the Free-Flying Unmanned Robotic Spacecraft for Asteroid Resource Prospecting and Characterization project under contract NNX15CK07C.

Abstract

Small spacecrafts requiring small propulsion systems are becoming more popular for low Earth orbit. It is important for these research satellites to have accurate guidance and control systems. Small propulsion systems will also be beneficial for multiple small spacecrafts used future exploration expeditions beyond low Earth orbit. These small spacecrafts benefit from the simplicity of low thrust cold gas propulsion systems. Additionally, large spacecrafts using low thrust, high specific impulse propellants for main propulsion systems, such as ion engines, allow longer and more flexible missions, including Earth orbiting spacecraft and interplanetary spacecraft.

In order to extent the life of future planetary exploration missions, it becomes necessary to use In-Situ Resource Utilization (ISRU) to be able to extract resources such as water, oxygen, propellants, and building materials from the local target environment. Small free flying vehicles can be used for quickly surveying planetary surfaces in order to search for potential resource locations. These surveying vehicles can also use such extracted propellants if their propulsion system is designed for it. Cold gas propulsion provides a flexible system to use locally extracted or manufactured propellants.

This dissertation investigates nonlinear feedback control techniques for spacecraft with low thrust, cold gas thrust, and spacecraft with cold gas thrust. A model for a cold gas propulsion system is developed for designing control systems for multiple types cold gas thrusters. The model is also used for testing control algorithms in simulation. The cold gas model is validated from a cold gas propulsion hardware testing, and a control law is tested on hardware.

Contents

List of Tables

List of Figures

Chapter 1

Introduction

1.1 Motivation

Small spacecrafts with small propulsion systems, such as cold gas propulsion, and large spacecrafts using more efficient electric propulsion, are becoming more popular. These systems are replacing the traditional large thrust chemical propulsion systems for spacecraft once they have reached orbit. This work investigates control systems for such spacecraft with small thrust.

Cold gas propulsion is a relatively low-cost, low mass, and simple propulsion system that can be run with many kinds of benign propellants at low power consumption levels. Such a method of propulsion is a space proven technology that has been in use since the 1960's (Mueller, Hofer, & Ziemer, 2010). Cold gas propulsion has worked well for attitude control systems because of its low thrust and high response times.

A cold gas propulsion system is well suited to provide the required thrust for a small surveyor spacecraft operated near an asteroid or planetary surface. The cold

gas propellant can be obtained in-situ from local surface or atmospheric constituents.

As spacecrafts become smaller, cheaper and more numerous, cold gas propulsion is a simple option for main propulsion. CubeSats for example, are popular low-cost spacecrafts used for low-Earth orbit (LEO) missions. For CubeSats, cold gas propulsion offers low mass, low energy and benign propellants, giving the spacecrafts accurate orbital and attitude control. Cold gas microthrusters have been in development for such small sized spacecraft as seen in (Louwerse, 2009; Kvell et al., 2014).

For missions beyond LEO, small free-flying vehicles may be used for surveying planetary surfaces. In order to extend the life of future planetary exploration missions, it becomes necessary to use In-Situ Resource Utilization (ISRU). ISRU technology is currently in development for human and robotic missions to the Moon, Mars, and near-Earth asteroids, to be able to extract resources such as water, oxygen, propellants, and building materials from the local target environment. This not only saves cost from launch mass, but makes exploration missions more flexible and can prolong a mission's life indefinitely (G. Sanders, Larson, Sacksteder, & Mclemore, 2008; Sridhar, Finn, & Kliss, 2000; G. B. Sanders & Larson, 2013).

For a small spacecraft operating in a low gravity environment, a cold gas propulsion system can be used as the main propulsion system for translation and attitude control despite its relatively low thrust. Using only the gas pressure as the stored potential energy, cold gas propulsion expands the types of materials that can be locally collected as propellant. Because cold gas propellant can be collected locally, the low specific impulse of cold gas propulsion does not have to be a limiting factor for the lifetime of a mission (Kitchen-McKinley, Drakunov, Mueller, & DuPuis, 2016).

Electric propulsion for spacecraft has been considered for as long as chemical

rockets, but rocket engineering was refined much earlier because it was needed for launch vehicles, and the low thrust of an ion engine makes it only useful for spacecraft in orbit as on-board propulsion. As ion thruster technology improved, they started being used for attitude control and orbit boosting, especially in situations where smooth continuous thrust is preferred. Ion engines continue to be developed for Earth orbit, but are additionally being developed for use as primary propulsion systems for deep space missions. This is possible because ion engines have now been proven to be able to operate continuously for long periods of time in deep space. Their high efficiency and low propellant throughput allow more ambitious and complex missions to be designed, and allow for more flexibility in long term missions.

The low continuous thrust of an ion engine requires a departure from impulse-based orbital mechanics. Novel control laws are therefore needed for low continuous thrust spacecraft. This system can be categorized into a class of systems that have small control input.

1.2 Outline of the Dissertation

This dissertation focuses on control problems for spacecraft with small thrust, and is organized as follows. Chapter 1 gives the motivation and background for spacecraft with small thrust input. Chapter 2 gives an introduction to the various mathematical and control methods that are used to solve the control problems. Chapter 3 focuses on feedback control for spacecraft with small continuous thrust. This motivation is for spacecraft with electric propulsion. Chapters 4 through 7 focus on control techniques for cold gas propulsion systems. This motivation is for small spacecrafts,

such as CubeSats, or planetary surveying spacecrafts, that require compact, simplified propulsion systems, with propellants that can more easily be extracted from the local environment. Chapter 4 provides the fluid model for a cold gas propulsion system to be used for Chapters 5 through 7. Chapter 5 gives the design, testing and control of the cold gas propulsion system to be used on a small surveying spacecraft operated near an asteroid surface. This system was built and tested on hardware at NASA KSC. Chapter 6 gives the design of a feedback controller for a cold gas propulsion system with multiple thruster actuation types for small surveying spacecraft to be operated in a gravity field. Multiple controllers and observers are tested in simulation. Chapter 7 gives the design of a time optimal, feedback, control of a small spacecraft with a simplified cold gas propulsion system, where the thrust force is dependent on the pressure.

1.3 Applications

1.3.1 Cold Gas Propulsion

The primary components of a cold gas propulsion system include a high pressure propellant storage vessel, a regulator to down-step and control pressure, solenoid valves for fast on/off switching, and thrusters to accelerate gas flow (Makled, AL-Sanabawy, & Bakr, 2009; Anis, 2012; Furumo, 2013).

A cold gas fluid model is useful for feedback control design and numerical simulation. The cold gas fluid model is developed as a series of control volumes connected by orifices. The flow is considered to be isentropic and adiabatic. The cold gas system is represented by first order ordinary differential equations of pressure and mass

flow. The thrust characteristics are obtained using the rocket thrust equations. Such equations can be derived from the conservation and energy, conservation of momentum, and the conservation of mass laws. The following equations represent the main governing equations for a cold gas fluid model.

$$\dot{P}_i = \frac{R_s T_i}{V_i}\left(\sum \dot{m}_{\text{in}} - \sum \dot{m}_{\text{out}}\right) \tag{1.1}$$

$$\dot{m} = C_d A P_u \sqrt{\frac{2\gamma}{R_s T_u(\gamma-1)}\left[\left(\frac{P_d}{P_u}\right)^{\frac{2}{\gamma}} - \left(\frac{P_d}{P_u}\right)^{\frac{\gamma+1}{\gamma}}\right]} \tag{1.2}$$

$$\frac{A_e}{A_t} = \frac{1}{M_e}\sqrt{\left(\frac{2}{\gamma+1}\right)\left(1+\frac{\gamma-1}{2}{M_e}^2\right)^{\frac{\gamma+1}{\gamma-1}}} \tag{1.3}$$

$$\frac{P_e}{P_c} = \left(1+\frac{\gamma-1}{2}{M_e}^2\right)^{-\frac{\gamma}{\gamma-1}} \tag{1.4}$$

$$\frac{T_e}{T_c} = \left(1+\frac{\gamma-1}{2}{M_e}^2\right)^{-1} \tag{1.5}$$

$$v_e = M_e\sqrt{\gamma R T_e} \tag{1.6}$$

$$\dot{m} = A_t P_c \sqrt{\frac{\gamma}{R T_c}\left(\frac{2}{\gamma+1}\right)^{\frac{\gamma+1}{\gamma-1}}} \tag{1.7}$$

$$F = \dot{m} v_e + (P_e - P_a)A_e \tag{1.8}$$

where P is pressure, V is volume, m is mass, T is temperature, R_s is the specific gas constant, γ is the ratio of specific heats, M is the Mach number, and v is the velocity, of the gas. The subscript i represents the index for each volume, subscripts u and d represent the upstream and downstream conditions, respectively, and subscript c,

t, and e represent the chamber, throat, and exit conditions, respectively. A is the cross-sectional area of the orifice, C_d is the coefficient of discharge, $\epsilon = \frac{A_e}{A_t}$ is the cross section area expansion ratio, P_a is the ambient pressure, and F is the thrust force. These equations are presented in more detail in Chapter 4.

For constant thrust systems, previous control methods have focused on thrust control using gas flow control, such as in (Kvell et al., 2014), or pulse modulation of the solenoid valve, such as in (Kienitz & Bals, 2005). The constant thrust also allows classical optimal control analysis, (Kirk, 2004) for spacecraft motion.

However, the simplest configuration for a cold gas system may be a control valve and thruster nozzle attached directly to a pressure tank. This further reduces the complexity of the propulsion system, but also reduces the controllability.

Small Sats

Figure 1.1 shows an example of a cubeSat. Figure 1.2 shows a commercial off the shelf (COTS) microthrust cold gas propulsion system designed for CubeSats.

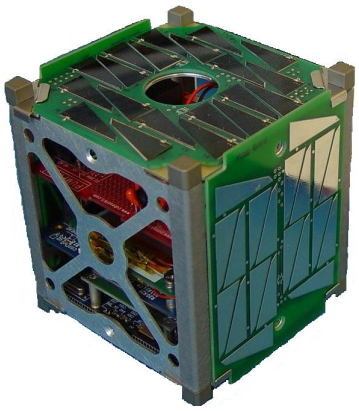

Figure 1.1: 1U CUBESAT (DARPA, 2008).

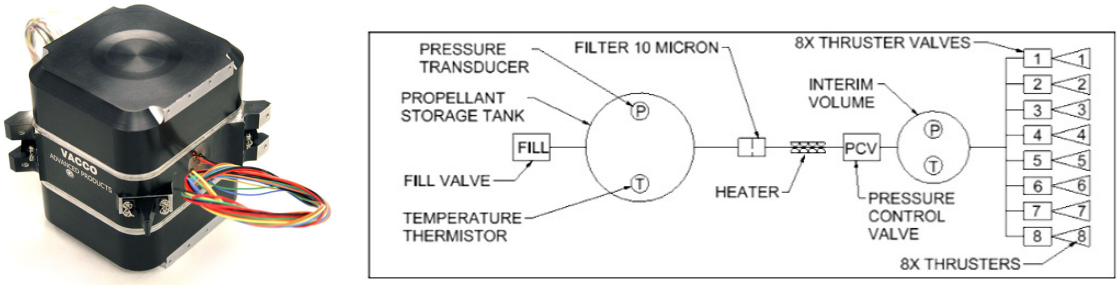

(a) (b)

Figure 1.2: Cold gas micro propulsion system for 3U CUBESAT. R134a propellant. Eight 25 mN thrusters. (VACCO, 2014).

1.3.2 Electric Propulsion

Electric propulsion is a general title that can be given to any engine that produces thrust from electrical energy. The fundamental process for thrusters is based on using electrical power to create an electric field that accelerates charged particles away from the spacecraft. This exhaust velocity determines the thrust of the engine. These thrusters are often rated by power, as power determines the strength of the electric field, and therefore the exhaust velocity of the propellant.

Electric propulsion has been studied for decades resulting in many different types of engines. Some examples are ion thrusters, Hall thrusters and plasma thrusters. In practice they are commonly powered by solar arrays on the spacecraft, and use an inert noble gas, such as xenon, as the propellant. The xenon gas is ionized so that it can be accelerated by the electric field and becomes the mass loss that results in thrust. This more direct method provides a high exhaust velocity for each ion, and is therefore more efficient with a much higher specific impulse than chemical rockets. However, the propellant throughput is very slow, which results in a very low thrust, but a mission is capable of carrying enough propellant so the engine can be operated

over a very long period of time.

Hall Thruster

The Hall thruster uses a neutral propellant that is ionized primarily through collisions with electrons. These electrons are held in a Hall current produced by radial magnetic field and an axial electric field. A coaxial magnetic coil configuration produces the inward radial magnetic field. An internal anode coupled with an external cathode produces the outward axial electric field. This electric field is the direct source for accelerating the ions away from the spacecraft and therefore creating a thrust. The cathode also provides an external source of electrons to neutralize the ions once they have left the spacecraft (Choueiri, 2001).

Governing Equations

A fluid model of the plasma flow in a Hall thruster can be used for feedback control design and numerical simulation. The time-dependent one-dimensional fluid model of the plasma flow in a Hall thruster is described by the following first order partial

differential equations,

$$\frac{\partial N}{\partial t} + V\frac{\partial N}{\partial x} = -\beta N n + \nu_{iw} n \tag{1.9}$$

$$\frac{\partial n}{\partial t} + \frac{\partial}{\partial x}(n v_i) = \beta N n - \nu_{iw} n \tag{1.10}$$

$$\frac{\partial n}{\partial t} + V\frac{\partial}{\partial x}(n v_{ex}) = \beta N n - \nu_{iw} n \tag{1.11}$$

$$\frac{\partial}{\partial t}(n m_i v_i) + \frac{\partial}{\partial x}(n m_i v_i^2) = neE + \beta N n M V - \nu_{iw} n m_i v_i \tag{1.12}$$

$$eE = -\frac{1}{n}\frac{\partial}{\partial x}(n T_e) - \nu_e m_e v_{ex} - \omega_{ce} m_e v_{e\theta} \tag{1.13}$$

$$\frac{\partial}{\partial t}(n v_{e\theta}) + \frac{\partial}{\partial x}(n v_{ex} v_{e\theta}) = \omega_{ce} n v_{ex} - \nu_e n v_{e\theta} \tag{1.14}$$

$$\frac{\partial}{\partial t}\left[\frac{3}{2} n T_e + \frac{1}{2} n m_e (v_{ex}^2 + v_{e\theta}^2)\right] + \frac{\partial}{\partial x}\left[\frac{5}{2} n v_{ex} T_e + \frac{1}{2} n v_{ex} m_e (v_{ex}^2 + v_{e\theta}^2)\right] = -\beta N n \gamma_i \epsilon_i - \nu_{ew} n \epsilon_w - n v_{ex} eE \; . \tag{1.15}$$

where n is the electron and single charge ion density, N is the neutral density, V is the axial velocity of the neutrals, β is the ionization rate, ν_{iw} is the collision frequency of the ions impacting the walls, E is the axial electric field, ω_{ce} is the electron cyclotron frequency, v_i is the ion axial velocity, v_{ex} and $v_{e\theta}$ are the axial and azimuthal electron velocities, respectively, T_e is the electron temperature and $\gamma_i \epsilon_i$ is the effective ionization cost (Barral, Miedzik, & Ahedo, 2008).

Electric Propulsion for Spacecraft

The low thrust of ion engines makes them only useful for spacecraft as on-board propulsion after the launch phase of a mission. They have therefore often been used to make slow attitude corrections, orbit boosting, and station keeping maneuvers, on spacecraft in Earth orbit.

Recently ion engines have been implemented as primary propulsion for long duration missions. There have been three missions so far; Deep Space 1, Hayabusa, and Dawn. Electric propulsion is proving to be an asset for complex deep space exploration (Polk, Kakuda, Anderson, & Brophy, 1999; Komurasaki & Kuninaka, 2007; J. Brophy, Ganapathi, Garner, & Gates, 2004).

Such complex deep space missions are possible because of the high efficiency and high specific impulse of the ion engine, which allow for enough on-board fuel to provide a large total delta-v for complex deep space missions. This provides an advantage over chemical rockets. The lower thrust can also be an advantage when smooth continuous thrust is desired.

Missions

The NASA Deep Space 1 (DS1) was the first interplanetary mission to use an electric propulsion engine in deep space and as the on-board primary propulsion. The mission was used to validate several high risk technologies including the solar electric propulsion (SEP) system. It was a 30 cm diameter, 2.3 kW ion thruster using xenon as the propellant. The ion propulsion system (IPS) was used for deterministic thrusting and trajectory correction maneuvers. Launched in 1998, DS1 successfully encountered the asteroid Braille in 1999 and the comet Borrelly in 2001. The IPS used 73 kg of xenon propellant and operated for a total of 16,265 hours (Polk et al., 1999; Rayman, Varghese, Lehman, & Livesay, 2000; Sengupta et al., 2009; J. R. Brophy, 2002).

The ESA SMART-1 (Small Mission for Advanced Research in Technology) was a lunar probe launched in 2003 to validate the PPS-1350 Hall thruster as its on-board,

primary propulsion system. It used 75 kg of xenon propellant, with a maximum of 1.5 kW, and operated for for a total of 4600 hours providing a delta-v of 3.5 km/s (Koppel, Marchandise, Prioul, Estublier, & Darnon, 2005; Darnon, Arrat, D'Escrivan, Chesta, & Pillet, 2007; Cornu, Marchandise, Darnon, & Estublier, 2007).

The JAXA Hayabusa was the first asteroid sample return mission. It used a cathode-less electron cyclotron resonance ion engine with 1.1 kW of power. The two engines were operated for a total of 40,000 hours providing a delta-v of 2.1 km/s. It was launched in 2003, encountered the asteroid Itokawa in 2005, and returned to Earth in 2010. It is also worth noting that when the reaction wheels and thrusters failed, the ion propulsion systems was used for attitude control and main propulsion, which saved the mission (Komurasaki & Kuninaka, 2007).

Dawn is currently in cruise transfer to Ceres after completing all objectives at Vesta. Dawn uses three of the ion thrusters based on the DS1 IPS. With 450 kg of xenon, it will provide a total delta-v of 11 km/s operated over a 10 year period. This delta-v will provide the necessary energy (along with a Mars gravity assist) for Dawn to become the first spacecraft to go into orbit around one body and then leave that body to orbit around another. This will make it the first to orbit two extraterrestrial bodies as well as the first mission to orbit a main-belt asteroid. It is also the first NASA science mission to use ion propulsion for primary propulsion. The mission involves a heliocentric orbital transfer to Vesta, orbit capture at Vesta, orbital transfer at Vesta for three altitudes, departure and escape from Vesta, heliocentric orbital transfer to Ceres, orbit capture at Ceres, and orbital transfer to low orbit at Ceres. This is the largest delta-v ever provided by an on-board propulsion system (Garner & Rayman, 2010; J. Brophy, Marcucci, Ganapathi, Gates, & Garner, 2005;

J. Brophy et al., 2004).

These successful uses of electric propulsion have caused an increased interest for replacing chemical rockets as the primary propulsion system on future deep space missions. NASA is currently designing a mission to redirect a relatively small near-Earth asteroid (7-10 meter diameter, 500 tons) by sending a spacecraft to capture and transfer the object to a lunar orbit, where it can be studied by astronauts. The mission calls for a xenon solar electric propulsion system because of the high delta-v required. This mission was announced in 2013 for the early 2020s (Stich, 2013). This Asteroid Capture and Redirect mission is part of a larger Asteroid Initiative headed by NASA for the purpose of identifying near-Earth objects (NEOs) that could potentially cause significant damage to Earth's human population and prepare possible missions that could be used to avoid these asteroid encounters.

Some contactless asteroid deflection missions have been investigated as they would be advantageous for use on long period deflection of subkilometer asteroids. Two such missions are the gravity tow mission (Lu & Love, 2005) and an ion beam shepherd mission (Bombardelli & Peláez, 2011a).

In order to gravitationally tow an asteroid slowly into a new orbit using the mass of a nearby spacecraft, the high specific impulse of the ion engine may be useful for the high delta-v required, but additionally, the low thrust aspect is necessary so that the thrust is only marginally greater the the gravitational force. The force must be applied continuously for a long period of time. A 20 ton spacecraft could deflect a 200 m diameter asteroid within a year with a 20 year lead. It requires continuous control to hover at the desired altitude from the asteroid (Lu & Love, 2005).

Another mission investigated involves slowly deflecting an asteroid by pushing

on it with a high collimated high velocity ion beam produced by an on-board ion thruster. This method is called the ion beam shepherd (IBS) and could transmit momentum similar to attaching an ion engine to the asteroid (Bombardelli & Peláez, 2011a). This technique has also been investigated as a method for space debris removal in Earth orbit (Bombardelli & Peláez, 2011b). Both of these methods are contactless deflection involving low continuous thrust scenarios. This is advantageous for subkilometer asteroids made of loosely bound rock, irregularly shaped, and can be used independent of asteroid spin.

Another proposed sample return mission of a near-Earth asteroid is the joint ESA/JAXA MARCO POLO mission which would use a cathode-less microwave discharge ion engine with a possible launch date in the late 2010s. The engine is based on the Hayabusa engine (Barucci et al., 2008).

NASA is also continuing development of more powerful engines such as VASIMR (Variable Specific Impulse Magnetoplasma Rocket) which will be one hundred times more powerful than current ion thrusters, and even more powerful engines are being called for.

One draw back to ion propulsion is the low thrust and long time period missions coupled with the difficulties of deep space communication. These missions will require autonomous navigation and control for spacecraft with low continuous propulsion.

Disturbances

These models are derived based small perturbations of the general central force models, where the small perturbation is the known constant acceleration of the low thrust engine. It would useful to include other possible perturbations such us disturbances.

One possible disturbances is the force due to the solar wind. This is the type of disturbance that could be modeled as the an unknown bounded disturbance. That is, the exact value of the solar wind at a given location is not known, but a maximum may be known based on solar wind knowledge.

Another possible disturbance are spacecraft oscillations that may occur due to nonrigid body dynamics. This is common with solar arrays. This can be modeled as a known disturbance if the dynamics are known for a particular spacecraft.

It is important to consider these disturbances when designing a control algorithm, especially if the disturbance forces are near the same order of magnitude as the thrust force, as may be the case with these low thrust engines. Robust and adaptive control law algorithms can be developed to overcome these disturbances. It is also possible to design observers to estimate the disturbances.

There is also always system noise and uncertainty in model parameters. In general a system with a disturbance, d, can be added to a system model as

$$\dot{\mathbf{x}} = \mathbf{f}(t, \mathbf{x}) + \sum_{k=1}^{m} \mathbf{g}_k(t, \mathbf{x}) u_k + d(t, \mathbf{x}) \tag{1.16}$$

where $\mathbf{x} = [x_1, \ldots, x_n]^T \in \mathbb{R}^n$, $\mathbf{f}(\mathbf{x})$ is the drift vector field, $\mathbf{g}_k$ are the control vector fields, u_k are the control inputs, and m is the number of control inputs.

1.4 Problem Statement

This work is devoted to the study of small thrust propulsion systems in regard to their modeling, and to the design of feedback control algorithms that are robust with respect to disturbance. Also some optimal control related issues are considered.

As spacecrafts become smaller, cheaper and more numerous, cold gas propulsion is a simple option for main propulsion and attitude control. A cold gas propulsion system is well suited to provide the required thrust for a small surveyor spacecraft operated near an asteroid or planetary surface with the additional bonus of obtaining propellant in-situ from the local environment. Previous thrust control has been based on feed forward and linear feed back techniques. Previous spacecraft control with cold gas thrusters assume constant or throttleable thrust.

Deep space exploration using electric propulsion presents a problem of a system that uses long periods of low, continuous thrust that require autonomous guidance and navigation control. A chemical rocket produces a high thrust for a short amount of time. These maneuvers are therefore treated as an instantaneous delta-v that transfers the spacecraft from one Keplerian orbit to another. The nature of the continuous thrust requires non-Keplerian orbital models to correctly control orbital transfer maneuvers. The control techniques developed in general for systems with a small control input could be applied to spacecraft with electric propulsion. These techniques could be very different than current control methods for missions using chemical propulsion.

Chapter 2

Mathematical and Control Methods

The dynamical systems to be studied in this dissertation are generally defined in this section. A scalar function is defined as a map from a vector of state values, $\mathbf{x} \in \mathbb{R}^n$, to a scalar value, $f \in \mathbb{R}$, denoted as $f(\mathbf{x}) : \mathbb{R}^n \to \mathbb{R}$. A vector function, is defined as a map from a vector of state values, $\mathbf{x} \in \mathbb{R}^n$, to a vector of values, $\mathbf{f} \in \mathbb{R}^n$, denoted as $\mathbf{f}(\mathbf{x}) : \mathbb{R}^n \to \mathbb{R}^n$. The vector function can be denoted as vector of scalar functions as

$$\mathbf{f}(\mathbf{x}) = [f_1(\mathbf{x})\ f_2(\mathbf{x}) \dots f_n(\mathbf{x})]^T\ .$$

The most general autonomous system is a finite number of coupled first-order ordinary differential equations

$$\dot{\mathbf{x}} = \mathbf{f}(t, \mathbf{x}, \mathbf{u}) \tag{2.1}$$

where $\mathbf{x} \in \mathbb{R}^n$ is the state vector, $\mathbf{u} \in \mathbb{R}^m$ is the input vector, and t is time. A subclass of nonlinear systems that is commonly studied is called control affine. Such systems can be defined when the control input is linear and the system can therefore be written as

$$\dot{\mathbf{x}}(t) = \mathbf{f}(\mathbf{x}(t)) + \mathbf{g}(\mathbf{x}(t))\mathbf{u}(t) \tag{2.2}$$

where $\mathbf{f}(\mathbf{x})$ is the drift vector field, $\mathbf{g}(\mathbf{x})$ is the control vector field, and where both vector fields are infinitely smooth. A general block diagram of a feedback control for such a system is shown in Figure 2.1. The state output is

$$\mathbf{y} = \mathbf{h}(\mathbf{x}) \tag{2.3}$$

where $\mathbf{y} \in \mathbb{R}^p$. To recover the system state for feedback control, an observer can be designed in the form

$$\dot{\hat{\mathbf{x}}} = \hat{\mathbf{f}}(\hat{\mathbf{x}}, \mathbf{u}) + \mathbf{\Lambda}(\mathbf{y} - \mathbf{h}(\hat{\mathbf{x}})) \tag{2.4}$$

where the estimated state $\hat{\mathbf{x}}$ is driven to the actual state and where $\mathbf{\Lambda}$ is a function of the estimate error. A feedback controller is designed to drive the system state to the desired state, $\mathbf{x}^*$.

2.1 Linear Control

The simplest form of a state feedback controller is a linear controller. A linear controller is the first choice for a linear system or a nonlinear system that can reasonably

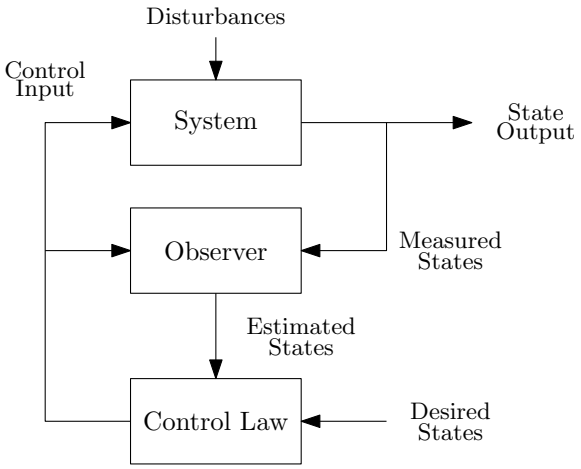

Figure 2.1: General block diagram for a control system.

be linearized. A linear time-invariant system as described in state space is

$$\dot{\mathbf{x}} = \mathbf{A}\mathbf{x} \tag{2.5}$$

where $\mathbf{x} \in \mathbb{R}^n$ is the state vector and $\mathbf{A} \in \mathbb{R}^{n \times n}$ is a constant matrix. A linear time-invariant system with a control input vector, $\mathbf{u} \in \mathbb{R}^m$, and a measured output state vector $\mathbf{y} \in \mathbb{R}^p$ is written as

$$\dot{\mathbf{x}} = \mathbf{A}\mathbf{x} + \mathbf{B}\mathbf{u} \tag{2.6}$$

$$\mathbf{y} = \mathbf{C}\mathbf{x} \tag{2.7}$$

where $\mathbf{B} \in \mathbb{R}^{n \times m}$ and $\mathbf{C} \in \mathbb{R}^{p \times n}$ are constant matrices. A linear observer drives the estimated state to the actual state and is written in the form

$$\dot{\hat{\mathbf{x}}} = \mathbf{A}\hat{\mathbf{x}} + \mathbf{B}\mathbf{u} + \mathbf{L}(\mathbf{y} - \mathbf{C}\hat{\mathbf{x}}) \tag{2.8}$$

where $\mathbf{L} \in \mathbb{R}^{n \times p}$ is a constant observer gain. A full state linear feedback control drives the state error $\bar{\mathbf{x}} = \hat{\mathbf{x}} - \mathbf{x}^*$ to zero by defining the proportional control law as

$$\mathbf{u} = -\mathbf{K}\bar{\mathbf{x}} \tag{2.9}$$

where $\mathbf{K} \in \mathbb{R}^{m \times n}$ is a constant proportinal gain (Wie, 2008). For control of systems with limited control, the small gains theory attempts to chose a control gain $\mathbf{K}$ such that the magnitude of the control input, $\|\mathbf{u}\|$, is as small as possible. These linear control methods have a limited application in the small thrust problems that are presented in this work. Therefore nonlinear control methods are investigated.

2.2 Small Control Property

One possible technique for constructing a control law is to use the method for constructing Lyapunov functions for affine and homogeneous systems that satisfy the "Jurdjevic-Quinn" conditions (Faubourg & Pomet, 2000). This technique was investigated in (Kellett & Praly, 2004) and (Gurfil, 2007). This involves the nonlinear control system of the form

$$\dot{\mathbf{x}} = \mathbf{f}(\mathbf{x}) + \sum_{k=1}^{m} \mathbf{g}_k u_k \tag{2.10}$$

where $\mathbf{x} = [x_1, \ldots, x_n]^T \in \mathbb{R}^n$, $\mathbf{f}(\mathbf{x})$ is the drift vector field, $\mathbf{g}_k$ are the control vector fields, u_k are the control inputs, and m is the number of control inputs. If $\mathbf{g}_k \in C^\infty$ $\forall k = 1, \ldots, m$, the system (2.10) is affine.

Feedback control algorithms can be designed by developing a Lyapunov function $V(x)$ that has the properties of being positive definite and where $\dot{V}(x)$ is negative

semi-definite. For small control, the Lyapunov function should also satisfy

$$L_{f_0}V(x) + \sum_{k=1}^{m} u_k L_{f_0}V(x) < 0 \tag{2.11}$$

where L is the Lie or direction derivative. Then the small control property is satisfied as

$$\|x\| < \delta \Longrightarrow \exists u \begin{cases} \|u\| < \epsilon \\ L_{f_0}V(x) + \sum_{k=1}^{m} u_k L_{f_0}V(x) < 0 \end{cases} \tag{2.12}$$

for $\epsilon > 0$, and $\delta > 0$ (Faubourg & Pomet, 2000).

The controllability, stabilizability and accessibility of the general nonlinear control system is extensively discussed in (Jurdjevic & Quinn, 1978) through the use of the Lie algebra that is generated by the vector fields of the system. The controllability, stabilizability and accessibility is shown for different classes of systems.

The stabilizability of the general nonlinear control system was also discussed in (Artstein, 1983) based on the class of Lyapunov functions. It was shown that there exists a closed loop continuous feedback stabilizer if a smooth Lyapunov function exists, but additional conditions on the Lyapunov function are necessary for the the controller to be continuous at the origin. The difference between relaxed controls and ordinary controls is also discussed (Artstein, 1983).

Using the results from (Artstein, 1983), it was then shown in (Sontag, 1989) that a stabilizing feedback control would be continuous at the origin if it satisfied the small control property, see theorem 2.1. The small control property is also formalized along with a universal formula to construct a continuous feedback stabilizer based on the Lie derivatives of a control Lyapunov function.

Theorem 2.1. *(small control property) For every given $\epsilon > 0$ there exists a $\delta > 0$ such that for some $x \neq 0$ that satisfies $||x|| < \delta$, there exists a $||u|| < \epsilon$ such that*

$$L_{\mathbf{f}}V(\mathbf{x}) + \sum_{k=1}^{m} u_k L_{\mathbf{g}_k}V(\mathbf{x}) < 0 \tag{2.13}$$

where $V(\mathbf{x})$ is a smooth, proper, and positive definite function known as a control Lyapunov function. It was also shown that if the control Lyapunov function satisfied the small control property for an affine control system, then the continuous and asymptotically stabilizing feedback can be constructed as

$$u_k = -\frac{a + \sqrt{a^2 + (\sum_{i=1}^{m} b_i^2)^2}}{\sum_{i=1}^{m} b_i^2} b_k \tag{2.14}$$

where $a = L_{\mathbf{f}}V(\mathbf{x})$ and $b_k = L_{\mathbf{g}_k}V(\mathbf{x})$. The small control property is given for the general nonlinear system. In other words, if the system, with such Lyapunov functions, is within a finite distance from the origin, an arbitrarily small control can be used to drive the system to the origin.

In (Faubourg & Pomet, 2000) this work is furthered by introducing methods to construct such control Lyapunov functions, specifically affine, homogenous, nonlinear systems with Jurdjevic-Quinn conditions. This can work for stabilization of a system with small control, but not necessarily control of a system with small control input.

2.3 Optimal Control

Small control analysis can benefit from optimal control theory because of the inherent control input constraint. This section outlines the classical approach to derive a time

optimal feedback control for a time invariant linear system. This is to contrast the time optimal feedback controller derived for the system in Chapter 7. Consider a linear, stationary system of order n and having m controls as

$$\dot{\mathbf{x}} = \mathbf{A}\mathbf{x} + \mathbf{B}\mathbf{u} \, . \tag{2.15}$$

The following theorems can be to applied to such a system from Pontryagin's minimum principle for minimum time problems.

Theorem 2.2 (Existence)**.** *If all of the eigenvalues of* $\mathbf{A}$ *have nonpositive real parts, then an optimal control exists that transfers any initial state* $\mathbf{x}_0$ *to the origin.*

Theorem 2.3 (Uniqueness)**.** *If an extremal control exists, then it is unique.*

Theorem 2.4 (Number of switchings)**.** *If the eigenvalues of* $\mathbf{A}$ *are all real, and a (unique) time-optimal control exists, then each control component can switch at most* $(n-1)$ *times.*

For the system

$$\begin{aligned} \dot{x}_1 &= x_2 \\ \dot{x}_2 &= u \end{aligned} \tag{2.16}$$

with control $|u| \leq 1$, the minimum time optimal control can be derived from the following method. The Hamiltonian of the system is

$$\mathscr{H} = 1 + p_1 x_2 + p_2 u \tag{2.17}$$

where p_i are the Lagrange multipliers or costates. The minimum principle indicates

that the optimal control u^* must satisfy

$$p_2^* u^* \leq p_2^* u \tag{2.18}$$

and the optimal control is

$$u^*(p_2^*) = \left\{ \begin{array}{ll} -1 & \text{for } p_2^* > 0 \\ +1 & \text{for } p_2^* < 0 \end{array} \right\} = -\text{sgn}(p_2^*) \; . \tag{2.19}$$

From the Hamiltonian the costate solution can be found as

$$\begin{aligned} p_1^*(t) &= c_1 \\ p_2^*(t) &= -c_1 t + c_2 \; . \end{aligned} \tag{2.20}$$

Since $p^*(t)$, and therefore $u^*(t)$ can only change signs at most once, the optimal control from some initial state must be

$$u^*(t) = \left\{ \begin{array}{llllll} +1 & \text{for all } t \in [t_0, t^*] & \text{or} & & & \\ -1 & \text{for all } t \in [t_0, t^*] & \text{or} & & & \\ +1 & \text{for all } t \in [t_0, t_1) & \text{and} & -1 & \text{for all } t \in [t_1, t^*] & \text{or} \\ -1 & \text{for all } t \in [t_0, t_1) & \text{and} & +1 & \text{for all } t \in [t_1, t^*] \; . & \end{array} \right. \tag{2.21}$$

The segments of the optimal trajectories can be found by integrating the state equations with $u = \pm 1$ as

$$\begin{aligned} x_2 &= \pm t + c_3 \\ x_1 &= \pm \tfrac{1}{2} t^2 + c_3 t + c_4 \; . \end{aligned} \tag{2.22}$$

Time can be eliminated from these parametric equations to find parabolic trajectories

in state space as

$$\begin{aligned} x_1 &= \tfrac{1}{2}x_2^2 + c_5 \quad \text{for } u = +1 \\ x_1 &= -\tfrac{1}{2}x_2^2 + c_6 \quad \text{for } u = -1\ . \end{aligned} \tag{2.23}$$

From these a switching function can be defined as

$$s(x) = x_1 + \frac{1}{2}x_2|x_2| = 0 \tag{2.24}$$

and so

$$u^*(x) = \begin{cases} -1 & \text{for } s(x) > 0 \\ +1 & \text{for } s(x) < 0 \\ -1 & \text{for } s(x) = 0 \text{ and } x_2 > 0 \\ +1 & \text{for } s(x) = 0 \text{ and } x_2 < 0 \\ 0 & x = 0 \end{cases} \tag{2.25}$$

Thus a time optimal state feedback control law is derived (Kirk, 2004).

2.4 Variable Structure Control

Variable structure control and its subset, sliding mode control, are used for nonlinear feedback control design in conjunction with optimal control design. This section will describe the background of variable structure control (VSC).

To begin a Variable Structure System (VSS) is a system that changes its structure depending on its own state, as shown in Figure 2.2. For example, there exist N

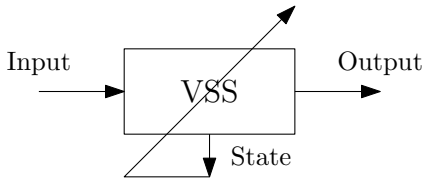

Figure 2.2: Block diagram of a Variable Structure System.

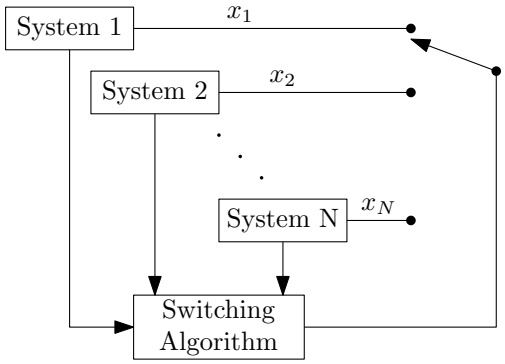

Figure 2.3: Block Diagram of a Variable Structure System with switching algorithm.

structures for a system described as

$$\begin{aligned} \dot{x}_1 &= f_1(t, x_1) \quad , \quad x_1 \in \mathbb{R}^{n_1} \\ &\vdots \qquad\qquad\quad \vdots \\ \dot{x}_N &= f_N(t, x_N) \quad , \quad x_N \in \mathbb{R}^{n_N} \end{aligned} \tag{2.26}$$

with a switching algorithm defined as

$$k = g_m(t, x_m) \; . \tag{2.27}$$

This is shown in Figure 2.3.

Variable structure control is a type of discontinuous nonlinear control. This method applies state feedback, discontinuous switching, between multiple, contin-

uous control laws. Consider a continuous system

$$\dot{x} = f(t, x, u) \tag{2.28}$$

where there exists several continuous controllers, $u_1(t, x), ..., u_N(t, x)$. A block diagram is shown in Figure 2.4. The control structure may switch between control

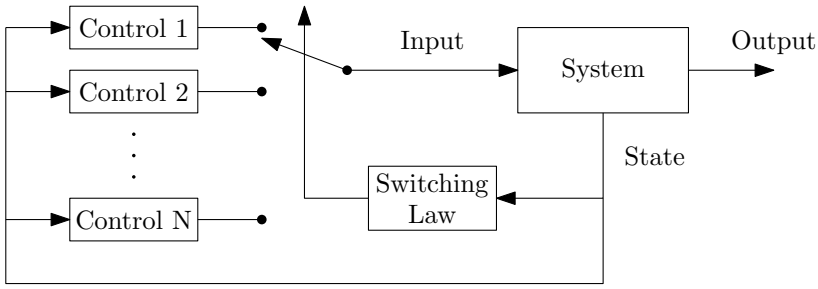

Figure 2.4: Schematic block diagram of variable structure control.

laws at very high frequency. Such discontinuous control laws were first introduced by (Függe-Lotz, 1953) and first described by (Emelyanov, 1967). Further investigation into the effects of variable structure control were done by (Filippov, 1988). To illustrate the benefits of VSC, consider an example system, $\ddot{x} = u$, where the control input, u is defined by two continuous controllers, $u_1 = -\alpha_1^2 x$, and $u_2 = -\alpha_2^2 x$, such that $\alpha_1^2 > \alpha_2^2$. Control u_1 and u_2 will each result in the set of state space trajectories as depicted by the elliptical paths in Figure 2.5 (a) and (b), respectively. Neither control is asymptotically stable. However, switching between the two controllers with a properly defined logic such as

$$u(x) = \begin{cases} u_1 & \text{if } x\dot{x} > 0 \\ u_2 & \text{if } x\dot{x} < 0 \end{cases} \tag{2.29}$$

will result in asymptotic stability as depicted in Figure 2.5(c).

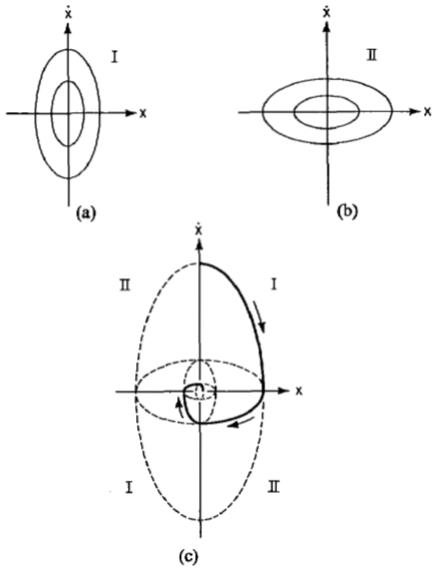

Figure 2.5: State space plot of VSC. Asymptotic stability achieved using feedback control by switching between structure I and II (Utkin, 1977).

2.5 Sliding Mode Control

Sliding mode control is a subset of variable structure control, where the system states are driven to a switching surface and then the states slide along the surface to the origin as shown in Figure 2.6. Variable structure control was further developed and sliding mode was introduced by (Utkin, 1978). Further development of sliding mode control was done by (Utkin, 1992) and (S. Drakunov, 1992).

A sliding mode controller using a variable structure system is particularly suitable method for handling nonlinear systems with uncertain dynamics and disturbances. The main idea of the method is to switch the control in such a way so that the system from any possible state was forced to reach a certain manifold in the state space, i.e.,

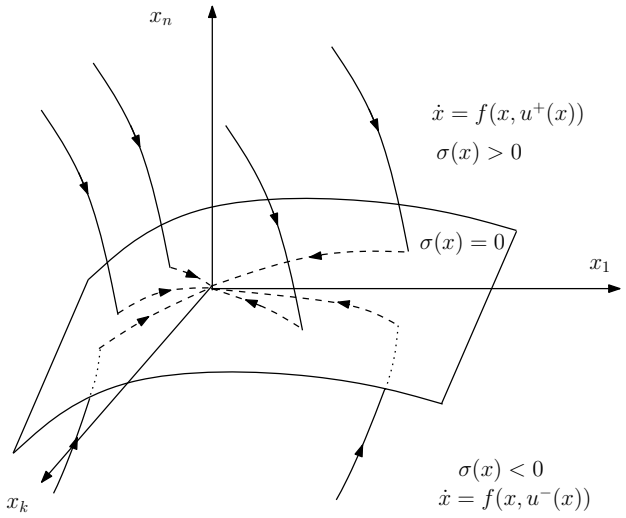

Figure 2.6: Example trajectory plot of sliding mode control (Kamran, 2016).

to keep some relation between the systems' internal variables. This relation (manifold) is chosen in such a way that the system fulfills a desired task under that constraint. The major advantage of Sliding Mode controllers is an inherent low sensitivity to parameter variations and disturbances since after the reaching phase the state is kept very robustly on the manifold in spite of the parameter variations and external disturbances. For a nonlinear system, given as,

$$\dot{x} = f(t, x) + B(t, x)u \tag{2.30}$$

where $x \in \mathbb{R}^n$ and $u \in \mathbb{R}^m$, the control input u is designed to switch between control laws based on the region of state space as determined by the switching surface σ. For example,

$$u_i = \begin{cases} u_i^+(t, x) \ , \ \text{if } \sigma_i(t, x) > 0 \\ u_i^-(t, x) \ , \ \text{if } \sigma_i(t, x) < 0 \ , \end{cases} \tag{2.31}$$

or written as one equation,

$$u_i = \frac{u_i^+ + u_i^-}{2} + \frac{u_i^+ - u_i^-}{2}\text{sgn}(\sigma_i) = g(t,x) + M(t,x)\text{sgn}(\sigma_i)\ . \tag{2.32}$$

where $\text{sgn}(\cdot)$ is the signum function, defined as

$$\text{sgn}(x) = \begin{cases} +1\ , \text{ if } x > 0 \\ -1\ , \text{ if } x < 0 \end{cases} \tag{2.33}$$

There are two phases in designing sliding mode control. The first involves finding a sliding surface, $\sigma(t,x) = 0$, such that if the system state is confined on this manifold the system state is stabilized to the desired equilibrium. The second phase involves finding a control that drives the system state to the sliding manifold from any initial conditions, such that the conditions for existence of sliding mode are fulfilled.

Beginning with the assumption that the sliding surface is already chosen, it can be differentiated in the form

$$\dot{\sigma} = \frac{\partial \sigma}{\partial x}Bu + \frac{\partial \sigma}{\partial x}f + \frac{\partial \sigma}{\partial t}\ . \tag{2.34}$$

Substituting in the controller u_i from (2.32), it becomes

$$\dot{\sigma} = \frac{\partial \sigma}{\partial x}BM\text{sgn}(\sigma) + F \tag{2.35}$$

where $F = \dfrac{\partial \sigma}{\partial x}f + \dfrac{\partial \sigma}{\partial t} + \dfrac{\partial \sigma}{\partial x}Bg$. The matrix M can be chosen as

$$M = -\Gamma\left(\frac{\partial \sigma}{\partial x}B\right)^{-1} \Rightarrow \dot{\sigma} = -\Gamma\text{sgn}(\sigma) + F \tag{2.36}$$

such that $\sigma \to 0$ in finite time, where $\|F\| < \Gamma$. Using the Lyapunov function

$$V(\sigma) = \text{sgn}(\sigma)^T \sigma = \sum |\sigma_i|$$

then

$$\dot{V}(\sigma) = \text{sgn}(\sigma)^T \dot{\sigma} = -\Gamma n + \text{sgn}(\sigma)^T F < 0$$

where $\text{sgn}(\sigma)^T \text{sgn}(\sigma) = n$, then $\sigma \to 0$ as $t \to \infty$. There may be other ways to chose matrix M to guarantee that $\sigma \to 0$.

The main difficulty in sliding mode control is in choosing the sliding manifold. In order to achieve the control goal, constrained motion on the sliding manifold should be stable. As shown in (Utkin, 1977), for systems such as (2.30) the equivalent control method can be used to obtain the equation of motion in sliding mode. By setting $\dot{\sigma} = 0$ in (2.34), and finding the corresponding control from

$$\frac{\partial \sigma}{\partial t} + \frac{\partial \sigma}{\partial x} f + \frac{\partial \sigma}{\partial x} B u_{\text{eq}} = 0 \tag{2.37}$$

then the solution is

$$u_{\text{eq}} = -\left(\frac{\partial \sigma}{\partial x} B\right)^{-1} \left(\frac{\partial \sigma}{\partial t} + \frac{\partial \sigma}{\partial x} f\right) . \tag{2.38}$$

By substituting this control into (2.30), the motion becomes

$$\dot{x} = \left[I - B\left(\frac{\partial \sigma}{\partial x} B\right)^{-1} \frac{\partial \sigma}{\partial x}\right] f - B\left(\frac{\partial \sigma}{\partial x} B\right)^{-1} \frac{\partial \sigma}{\partial t} . \tag{2.39}$$

If the control u is bounded, for example, if

$$\|u\| \leq U_{\max} \tag{2.40}$$

where $\|\cdot\|$ can be understood in different spaces such as

$$\|u\|_1 = |u_1| + \ldots + |u_m| \tag{2.41}$$

$$\|u\|_2 = \sqrt{|u_1|^2 + \ldots + |u_m|^2} \tag{2.42}$$

$$\|u\|_\infty = \max\{|u_1|, \ldots, |u_m|\} \ , \tag{2.43}$$

then a necessary condition for sliding mode to exist is

$$\|u_{\text{eq}}\| \leq U_{\max} \tag{2.44}$$

So

$$\left\| \left(\frac{\partial \sigma}{\partial x} B \right)^{-1} \left(\frac{\partial \sigma}{\partial t} + \frac{\partial \sigma}{\partial x} f \right) \right\| \leq U_{\max} \tag{2.45}$$

should be satisfied.

2.6 Hamiltonian Approach

One approach to controlling a system with arbitrarily small control input is to control the energy of the system. The total energy of a mechanical system can be defined by the Hamiltonian, H. The standard form of a system in terms of the Hamiltonian is

defined as

$$\begin{aligned} \dot{\mathbf{q}} &= \frac{\partial H}{\partial \mathbf{p}} \\ \dot{\mathbf{p}} &= -\frac{\partial H}{\partial \mathbf{q}} \\ H &= T + V \end{aligned} \tag{2.46}$$

where $\mathbf{q}$ is the position, $\mathbf{p}$ is the momentum, $T = T(\mathbf{p})$ is the kinetic energy and $V = V(\mathbf{q})$ is the potential energy. The total mechanical energy H is a constant of the motion.

If a mechanical system is perturbed by a small control input u, the Hamiltonian equations can be written as

$$\begin{aligned} \dot{\mathbf{q}} &= \frac{\partial H}{\partial \mathbf{p}} \\ \dot{\mathbf{p}} &= -\frac{\partial H}{\partial \mathbf{q}} + \mathbf{B}_p(\mathbf{q}, \mathbf{p})u \ . \end{aligned} \tag{2.47}$$

The control is to slowly drive the system energy H to a desired energy H^*, where $H = H(\mathbf{q}, \mathbf{p})$ and $H^* = H^*(\mathbf{q}^*, \mathbf{p}^*)$. The Hamiltonian equations of the desired system can be written as

$$\begin{aligned} \dot{\mathbf{q}}^* &= \frac{\partial H}{\partial \mathbf{p}}(\mathbf{q}^*, \mathbf{p}^*) \\ \dot{\mathbf{p}}^* &= -\frac{\partial H}{\partial \mathbf{q}}(\mathbf{q}^*, \mathbf{p}^*) \\ H^* &= H(\mathbf{q}^*, \mathbf{p}^*) \end{aligned} \tag{2.48}$$

where the total mechanical energy H^* is a constant of the motion. Another way to define the control goal is to design u such that system (2.46) is driven to system

(2.48). Additionally, the control input is constrained to be an arbitrarily small control input, $|u| \leq \epsilon$.

The Hamiltonian system can be written in the control affine form of

$$\dot{\mathbf{x}} = \mathbf{f}(\mathbf{x}) + \mathbf{B}(\mathbf{x})u \tag{2.49}$$

where $\mathbf{x} = [\mathbf{q}, \mathbf{p}]^T$

Designing such a control begins with the construction of the sliding surface defined by the energy error as

$$\sigma = H(\mathbf{q}, \mathbf{p}) - H^* = 0 \tag{2.50}$$

where H^* is constant. The time derivative of the sliding surface is

$$\dot{\sigma} = \frac{\partial H}{\partial p} B_p u \ . \tag{2.51}$$

The Lyapunov function is chosen as

$$V_L = \frac{1}{2}\sigma^T \sigma > 0 \ . \tag{2.52}$$

And its derivative is

$$\dot{V}_L = \sigma^T \dot{\sigma} = \sigma^T \frac{\partial H}{\partial p} B_p u \ . \tag{2.53}$$

To make this negative definite, the control input u is chosen as

$$u = -k\text{sgn}\left(\sigma^T \frac{\partial H}{\partial p} B_p\right) \ . \tag{2.54}$$

The Lyapunov function time derivative becomes

$$\dot{V}_L = \sigma^T \frac{\partial H}{\partial p} B_p \left(-k \text{sgn} \left(\sigma^T \frac{\partial H}{\partial p} B_p \right) \right) = -k \left| \frac{\partial H}{\partial p} B_p \right| \tag{2.55}$$

such that $\dot{V}_L < 0$ for all $k > 0$. This means the control input can be arbitrarily small and still drive the system to the desired energy.

Chapter 3

Propulsion for Orbital Control

Electric propulsion has the advantage of on board fuel efficiency, but because of its small continuous thrust, it introduces different orbital dynamics requiring new control methods. This chapter introduces the orbital dynamics and then a feedback controller is designed for an analogous mechanical system.

There are many control objectives that can be considered for low thrust spacecraft. Fuel optimal and time optimal control under different conditions of variable and fixed final positions, velocities and times. These may be useful for rendezvous.

It is often assumed that the low thrust is constant, but the engines have a small throttle range. The throttle is usually controlled to optimize for peak engine efficiency which is based on solar array orientation and distance from the Sun. Efficiency is also affected by the life cycle performance on the engine. Additionally, the spacecraft may have a range of permissible attitudes based on instrumentation that do not allow for the desired control thrust vector at that time. The cruise phases may be divided up into multiple segments that sum to the total desired thrust vector. These problems

were taken into consideration on the experimental Deep Space 1 (Polk et al., 1999; Rayman et al., 2000), and SMART-1 missions (Koppel et al., 2005).

3.1 Small Thrust Orbital Control

Most of the previous research involving orbital transfers of spacecraft are done using feedforward open loop design. For high thrust impulse, open loop control is required. For low continuous thrust, open loop design is useful for obtaining optimal trajectories.

There has been some previous work for continuous thrust orbital transfer. Minimum time orbital transfer control laws where deveopled using Lagrange multipliers (Thorne, 1996). A control law was developed to have a spacecraft arrive at a particular location in its orbit at an earlier time. Methods of optimal control and Lyaponuv based feedback control were used with a time optimal cost function (Zagaris, 2012).

For a many-revolution orbit transfer, a time optimal control for one orbit was expanded to multiple orbits. It was solved using the two point boundary value problem (Wiesel & Alfano, 1985). For another multi-revolution optimization problem, the low thrust trajectory optimization is based on aliasing from information theory. The algorithm generates candidate solutions and obtains optimal feedback closed looped controls without needing to compute costates or covectors and without Hamilton-Jacobi theory. It boasts fast computation times by solving small chunks along the trajectory (Ross, Gong, & Sekhavat, 2007). The SMART-1 orbital transfer from Earth to Lunar orbit control problem is considered using sparse nonlinear programming and discretization of trajectory dynamics while including gravitational perturbations of

other bodies (Betts & Erb, 2003).

The continuous nature of electric propulsion allows for feedback closed loop control laws do be developed.

Nonlinear feedback control is considered by (Kellett & Praly, 2004). The control law is constructed using Lyapunov based methods of backstepping, forwarding, and a modified form of Jurdjevic-Quinn. The results are designed under the conditions of coplanar circular orbit transfer with small control input limits. Optimization performance was not considered. Nonlinear feedback control was also considered by (Gurfil, 2007). Here, controllability, accessibility, and stability for nonlinear feedback control of low continuous thrust orbital transfer are investigated. However, the closed loop time varying dynamic control is left as an open question.

3.2 Orbital Modeling

Historically, orbital mechanics can be modeled based on Kepler's laws of orbital motion; an orbiting body follows the path of an ellipse, the speed of the orbiting body will be determined as it sweeps out equal areas in equal time, and the orbital period is based on the size of the orbit. The driving force for these motions were shown to be a central force based Newton's law of gravitation defined as

$$\mathbf{F}_g = \frac{Gm_1m_2}{r^2}\hat{\mathbf{r}} \tag{3.1}$$

where G is the universal gravitational constant, m_i is the mass of each object, and r is the distance between the two objects. For the two body problem, the equations of

relative motion are derived to be

$$\ddot{\mathbf{r}} = -\frac{\mu}{r^3}\mathbf{r} \ . \tag{3.2}$$

This second order differential equation governs the motion of m_2 relative to m_1, where μ is the gravitational parameter defined as $\mu = G(m_1 + m_2)$, $\mathbf{r}$ is the position vector of m_2 relative to m_1, and $r = ||\mathbf{r}||$ is the distance between the two objects. From this, Kepler's laws can be derived under the assumptions that if we let $m_1 = M$ and $m_2 = m$, where M is the mass of a large body such as the Sun or a planet, m is the mass of a spacecraft, and $M >> m$. Under these conditions (3.2) describes the orbiting motion of the spacecraft around a large body. Additionally, the gravitational parameter $\mu \approx GM$ (Curtis, 2005).

This motion is also only true under the conditions that there are only two objects, and that the force of gravity is the only force. However, orbiting spacecraft experience gravitational pull from multiple bodies, some of which may be significantly asymmetrical, and other forces such as atmospheric drag or solar wind. Each of these forces, as well as any other small disturbances, are modeled as perturbations. The last force on a spacecraft not available to other orbiting bodies, is the thrust of an engine that allows the spacecraft to transfer from one orbit to another.

The additional force of thrust is given by the rocket equation

$$\sum \mathbf{F}_{ext} + \dot{m}\mathbf{v}_e = m\ddot{\mathbf{r}} \tag{3.3}$$

where $\sum \mathbf{F}_{ext}$ are the external forces on the spacecraft, mainly $\mathbf{F}_g$, and the term $\dot{m}\mathbf{v}_e$ is the momentum thrust, which comes from $\dot{m}$, the propellant mass flow rate, and $\mathbf{v}_e$,

the exhaust velocity of the propellant. The linear acceleration of the spacecraft due to the propulsion system can be described as

$$A = \frac{T}{m_o + \dot{m}t} \tag{3.4}$$

where T is the constant thrust of the propulsion system, and m_o is the initial mass of the spacecraft. This additional acceleration can be added to (3.2) as

$$\ddot{\mathbf{r}} = -\frac{\mu}{r^3}\mathbf{r} + \mathbf{A} \ . \tag{3.5}$$

For electric propulsion systems, it may be considered that $\dot{m} = 0$, and therefore A to be constant (Thorne, 1996). There are multiple reference frames to describe this motion and they are discussed in the following sections.

3.2.1 Inertial Frame

It may be obvious to begin by expressing (3.5) explicitly in Cartesian state space as,

$$\begin{aligned}
\dot{x} &= v_x \\
\dot{y} &= v_y \\
\dot{z} &= v_z \\
\dot{v}_x &= -\tfrac{\mu}{r^3}x + A\cos\beta\cos\alpha \\
\dot{v}_y &= -\tfrac{\mu}{r^3}y + A\cos\beta\sin\alpha \\
\dot{v}_z &= -\tfrac{\mu}{r^3}z + A\sin\beta
\end{aligned} \tag{3.6}$$

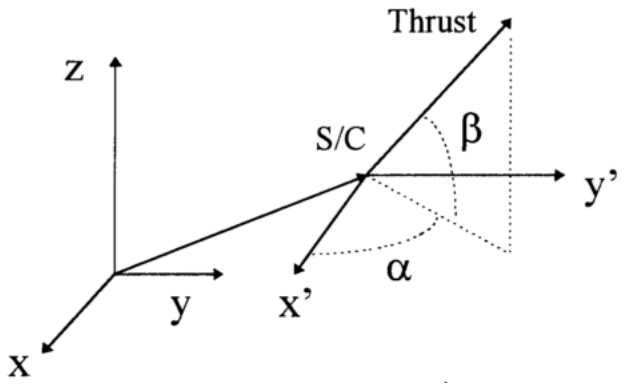

Figure 3.1: Thrust vector measured in body frame (Thorne, 1996).

where $r = \sqrt{x^2 + y^2 + z^2}$, and α and β are the angles of the thrust vector as measured in the body frame (Figure 3.1) (Thorne, 1996). From this model a feedback control algorithm could be implemented using control inputs that the trust T would be on or off, and the direction given by α and β. This control method could be designed to drive the system from its initial orbit state, $\mathbf{r}_0, \mathbf{v}_0$ to a desired orbit state $\mathbf{r}^*, \mathbf{v}^*$. This is a simple form but presents problems when solving numerically due to the fast changing variables, especially over long periods of time.

Given the low thrust, the system can be modeled as a two body problem with a perturbation. Using a variation of parameters technique, the six classical orbital elements can be derived in differential form, and have the advantage of changing slowly in time.

3.2.2 Orbit Elements

Traditionally, orbits are uniquely described by the six classical Keplerian orbital elements

$$(a, e, i, \Omega, \omega, \nu),$$

where a is the semimajor axis, e is the eccentricity, i is the inclination, Ω is the right ascension of the ascending node (RAAN), ω is the argument of periapsis, and ν is the true anomaly. For a stable orbit, each of these elements are constant except for the true anomaly, which gives the position in the orbit as a function of time. Deriving the differential form of these elements by a method of perturbation would yield a system of equations where the low thrust of the engine is that controllable perturbation. In the local-vertical-local-horizontal (LVLH) frame $[\hat{\mathbf{i}}_r, \hat{\mathbf{i}}_\nu, \hat{\mathbf{i}}_h]$, the accelerations and velocity vectors are given as (Zagaris, 2012)

$$\begin{aligned} \mathbf{A} &= a_r\hat{\mathbf{i}}_r + a_\nu\hat{\mathbf{i}}_\nu + a_h\hat{\mathbf{i}}_h \qquad (3.7)\\ \mathbf{v} &= \dot{r}\hat{\mathbf{i}}_r + r\dot{\nu}\hat{\mathbf{i}}_\nu \, . \qquad (3.8) \end{aligned}$$

The Lagrange Planetary Equations (LPEs) or Gauss's Variational Equations in acceleration form derived by (Schaub & Junkins, 2003) and shown in (Zagaris, 2012) also from (Battin, 1999) are

$$\begin{aligned} \dot{a} &= \tfrac{2a^2}{h}(e\sin\nu a_r + \tfrac{p}{r}a_\nu)\\ \dot{e} &= \tfrac{1}{h}(p\sin\nu a_r + ((p+r)\cos\nu + re)a_\nu)\\ \dot{i} &= \tfrac{r\cos(\omega+\nu)}{h}a_h\\ \dot{\Omega} &= \tfrac{r\sin(\omega+\nu)}{h\sin i}a_h\\ \dot{\omega} &= \tfrac{1}{he}(-p\cos\nu a_r + (p+r)\sin\nu a_\nu) - \tfrac{r\sin(\omega+\nu)\cos i}{h\sin i}a_h\\ \dot{\nu} &= \tfrac{h}{r^2} + \tfrac{1}{he}(p\cos\nu a_r - (p+r)\sin\nu a_\nu) \end{aligned} \qquad (3.9)$$

where $h = \sqrt{\mu p}$ is the specific angular momentum of the orbit, and $p = a(1-e^2)$ is the semilatus rectum of the orbit. But these are singular for circular orbits ($e = 0$)

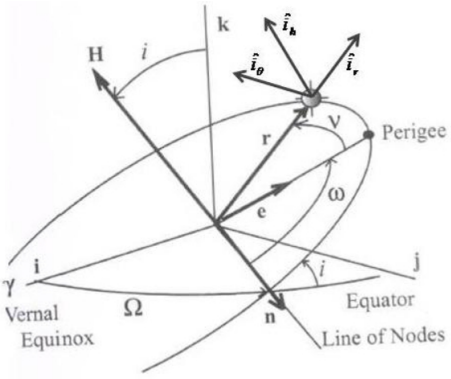

Figure 3.2: Classical orbital elements and the LVLH body frame (Zagaris, 2012).

and equatorial orbits ($i = 0$) (Zagaris, 2012).

3.2.3 Other Orbital Elements

The classical elements can be transformed from $(a, e, i, \Omega, \omega, \nu)$ to a new system $(p, e_x, e_y, h_x, h_y, L)$ given by the following equations for transformations (Kellett & Praly, 2004)

$$\begin{aligned} p &= a(1-e^2) \\ e_x &= e\cos(\omega+\Omega) \\ e_y &= e\sin(\omega+\Omega) \\ L &= \omega+\Omega+\nu \\ h_x &= \tan(i/2)\cos\Omega \\ h_y &= \tan(i/2)\sin\Omega \end{aligned} \tag{3.10}$$

where e_x and e_y are the x and y components of the eccentricity vector, h_x and h_y are the x and y components of the specific angular momentum vector, and L is the true longitude. The orbital model based on the Gauss equations in the local polar

coordinate system is given as (Kellett & Praly, 2004)

$$\begin{aligned}
\dot{p} &= 2kpa_\nu \\
\dot{e}_x &= k[Z\sin(L)a_r + Aa_\nu - e_y Y a_h] \\
\dot{e}_y &= k[-Z\cos(L)a_r + Ba_\nu + e_x Y a_h] \\
\dot{L} &= \sqrt{\tfrac{\mu}{p^3}}Z^2 + kY a_h \\
\dot{h}_x &= \tfrac{k}{2}X\cos(L)a_h \\
\dot{h}_y &= \tfrac{k}{2}X\sin(L)a_h
\end{aligned} \tag{3.11}$$

where

$$\begin{aligned}
k &= \sqrt{\tfrac{\mu}{p^3}}\tfrac{1}{Z}\ , \\
Z &= 1 + e\cos\nu\ , \\
A &= e_x + (1+Z)\cos L\ , \\
B &= e_y + (1+Z)\sin L\ , \\
X &= 1 + h_x^2 + h_y^2\ , \\
Y &= h_x\sin L - h_y\cos L\ .
\end{aligned}$$

In this form there are no singularities. A feedback control algorithm could be designed to use the control input $\mathbf{A}$ to drive the system from some initial state $(p, e_x, e_y, h_x, h_y, L)_0$, to some final state $(p, e_x, e_y, h_x, h_y, L)^*$.

3.3 Mechanical System Control

The inverted pendulum is studied as a lower order analogous system to the orbital model. The pendulum and orbital systems are both examples of a Hamiltonian mechanical system. A pendulum, with planar motion and small dissipative forces, is

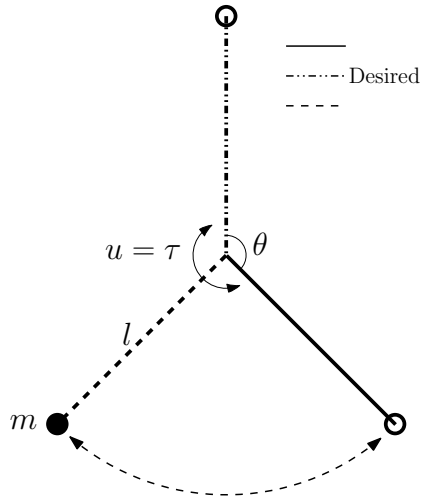

Figure 3.3: Inverted Pendulum.

a classically studied nonlinear. A feedback controller is designed for three types of desired conditions with a small continuous thrust input.

For a pendulum, as defined in Figure 3.3, the potential energy is

$$V(\theta) = mgl(\cos\theta + 1) \tag{3.12}$$

and the kinetic energy is

$$T(\theta, \dot{\theta}) = \frac{1}{2} ml^2 \dot{\theta}^2 \ . \tag{3.13}$$

The total Energy $E = T + V$ is

$$E = \frac{1}{2} ml^2 \dot{\theta}^2 + mgl(\cos\theta + 1) \tag{3.14}$$

where m is the mass of the pendulum located at length l, and θ is measured from the positive vertical. The potential energy is a function of height $h = l\cos\theta + l$ so that when the pendulum is in the positive vertical position, $\theta = 0$ and $h = 2l$, and in the

negative vertical position, $\theta = \pi, -\pi$ and $h = 0$.

From the Lagrangian, $L = T - V$, and using the Euler-Lagrange equation

$$\frac{d}{dt}\left(\frac{\partial L}{\partial \dot{\theta}}\right) - \frac{\partial L}{\partial \theta} = 0 \tag{3.15}$$

the equations of motion are

$$ml^2\ddot{\theta} = mgl\sin\theta\ . \tag{3.16}$$

Adding control u as a rotation torque or tangential force at distance l, (3.16) becomes

$$ml^2\ddot{\theta} = mgl\sin\theta + u\ . \tag{3.17}$$

3.3.1 Energy control

It is not possible to hold the pendulum at any given point using an arbitrarily small control input. Arbitrarily small feedback can only hold a constant position at natural equilibrium points. All other points would require an artificial equilibrium attained through a feed forward control. In the case of the pendulum, the feed forward portion would need to counter act the gravitational force at any time.

Instead of controlling the position directly, the controller will be designed to control the total energy of the system. Starting with the ideal condition that there are no dissipating forces, the total energy will naturally remain constant with no control input. The controller can then be designed to change the total energy, by either removing or adding energy. For any given total energy level, the pendulum would swing back and forth with a maximum height. The total energy, or maximum height, could slowly be increased or decreased using an arbitrarily small control input.

For optimal energy efficiency, it makes sense to follow the natural motion. In the case of the pendulum, the least amount of force will result in the most amount of energy increase if the force is added as the natural resonance of the system, that is, always adding force in the direction of motion.

To accomplish this, a sliding mode control will be implemented by choosing a novel sliding surface as the desired total energy of the system. This follows from the Hamiltonian of the system as described in Section 2.6. The sliding surface is

$$\sigma = (E - E^*) = 0 \tag{3.18}$$

where E^* is the desired total energy. By taking the time derivative and substituting the equations of motion, the control input u should be designed such that the state is driven to the sliding surface. Thus, the sliding surface becomes

$$\sigma = \frac{1}{2}ml^2x_2^2 + mgl(\cos x_1 + 1) - E^* \tag{3.19}$$

with its time derivative

$$\begin{aligned}
\dot{\sigma} &= ml^2x_2\dot{x}_2 - mgl\sin x_1\dot{x}_1 \\
&= ml^2x_2(\frac{g}{l}\sin x_1 + \frac{1}{ml^2}u) - mgl\sin x_1(x_2) \\
&= x_2mgl\sin x_1 + x_2u - x_2mgl\sin x_1 \\
&= x_2u
\end{aligned}$$

and so

$$\sigma\dot{\sigma} = \sigma x_2 u < 0\ . \tag{3.20}$$

By using the controller as

$$u = -\delta \text{sgn}(x_2 \sigma) \tag{3.21}$$

then

$$\begin{aligned} \sigma\dot{\sigma} &= \sigma x_2(-\delta \text{sgn}(x_2\sigma)) \\ &= -\delta|x_2\sigma| \end{aligned}$$

where $\sigma\dot{\sigma} < 0$ is guaranteed if $\delta > 0$. So δ can be an arbitrarily small control gain, that may be limited by the controller, and still reach the control goal. A similar controller was derived by (Åström & Furuta, 2000).

Example

For simplicity, the coefficients are set equal to 1, that is, let $g = 9.8\frac{m}{s^2}$, $l = 9.8m$ and $m = \frac{1}{9.8^2}kg$. Let the initial conditions be $\mathbf{x}_0 = [\pi\ 0]^T$, which corresponds to the pendulum at rest at the negative vertical equilibrium point, and therefore $E_0 = 0J$. Let the desired energy be $E^* = 2J$, which corresponds to many possible states, one in particular is $\mathbf{x}^* = [0\ 0]^T$, which corresponds to the unstable equilibrium at the positive vertical point. The equations of motion of the pendulum are modeled numerically in MATLAB using the Euler Method.

Figure 3.4 shows the system states over time. The energy successfully converges to its desired value and the position converges to the unstable equilibrium point. Figure 3.5 shows the path of the pendulum in state space. Notice that the desired energy is not a point in state space, but the set of points that have the same energy. Therefore the sliding surface is the desired energy level. Because the desired energy contains an

equilibrium point, the control drives the pendulum to a fixed position in this case.

This feedback controller works well, but it does not use sliding mode control until it reaches the desired energy. Therefore the control will be robust against disturbances once it reaches the desired energy. A more robust controller would have a sliding surface that could guide the pendulum to the desired energy.

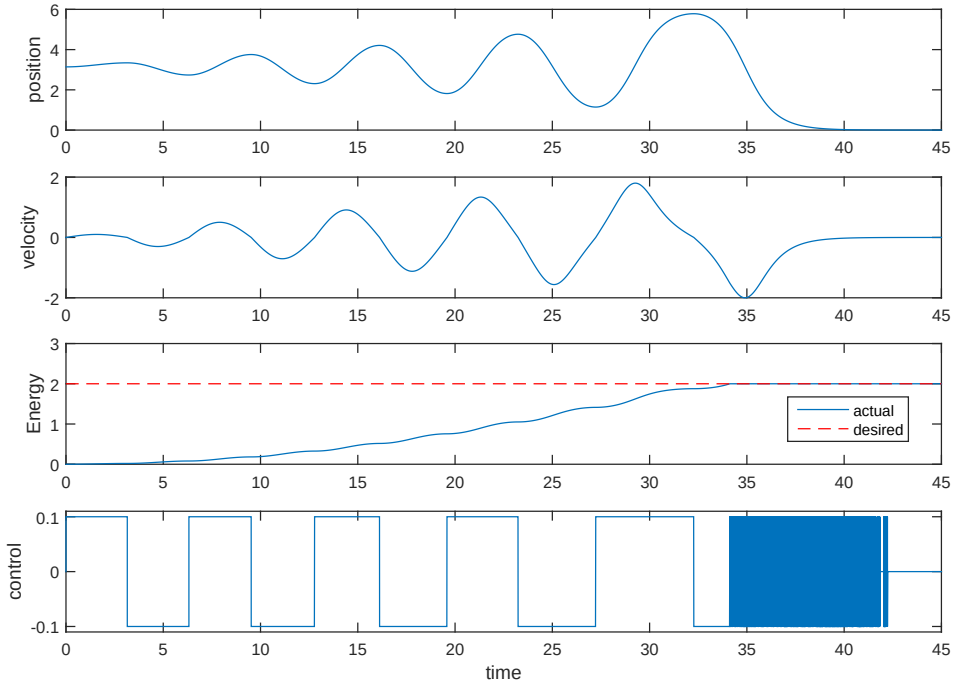

Figure 3.4: Inverted pendulum time profile results. Angular position and velocity, states x_1 and x_2. Total energy of the system is driven to desired energy. Arbitrarily small control input limited to $\delta = \pm 0.1$.

3.3.2 Virtual Sliding Surface Control

The energy controller is used on a virtual system that is similar to the actual system, but with no disturbances. The trajectory of the virtual system becomes the sliding surface of actual system. This allows for immediate convergence to a moving sliding

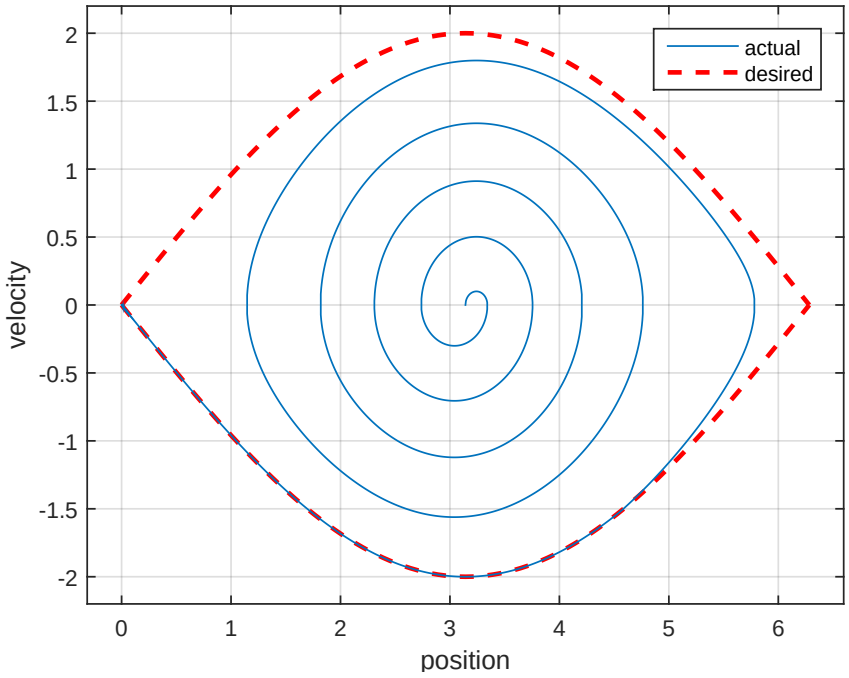

Figure 3.5: Inverted pendulum state space results. Angular position and velocity, states x_1 and x_2 driven to the sliding surface, $\sigma(\mathbf{x})$.

surface. The trajectory along the sliding surface allows for robustness against disturbances. The theory for such virtual point following is outlined in (S. V. Drakunov, 2008).

In general the virtual system is represented by the superscript $()^*$

$$\dot{x}^* = f(x^*) + B(x^*)u^* \tag{3.22}$$

$$\sigma^*(x) = 0 \tag{3.23}$$

$$u^* = u^*(E^*, E_{\text{des}}) \tag{3.24}$$

where E_{des} is the final desired energy. The virtual system has its own sliding surface and control law designed to drive the energy of the virtual system to the final desired

system. This is the same method as shown in Section 3.3.1. In general the actual system can have a disturbance $d(t, x)$ and is defined as

$$\dot{x} = f(x) + B(x)u + d(t, x) \tag{3.25}$$

$$\sigma(x) = 0 \tag{3.26}$$

$$u = u(E, E^*) \tag{3.27}$$

where the desired energy of the actual system, E^* is the current energy of the virtual system. The control law is the same as Section 3.3.1, however the desired energy is a moving surface.

For the pendulum example, the virtual pendulum system with is control law is defined as

$$\begin{aligned} \dot{x}_1^* &= x_2^* \\ \dot{x}_2^* &= \tfrac{g}{l}\sin x_1^* + \tfrac{1}{ml^2}u^* \end{aligned} \tag{3.28}$$

$$E^* = \frac{1}{2}ml^2 x_2^{*2} + mgl(\cos x_1^* + 1) \tag{3.29}$$

$$\sigma^* = (E^* - E_{\text{des}}) = 0 \tag{3.30}$$

$$u^* = -\delta^* \text{sgn}(x_2^* \sigma^*) \ . \tag{3.31}$$

The actual pendulum system with its control law is defined as

$$\begin{aligned} \dot{x}_1 &= x_2 \\ \dot{x}_2 &= \tfrac{g}{l}\sin x_1 + \tfrac{1}{ml^2}u + \xi \end{aligned} \tag{3.32}$$

$$E = \frac{1}{2}ml^2x_2^2 + mgl(\cos x_1 + 1) \tag{3.33}$$

$$\sigma = (E - E^*) = 0 \tag{3.34}$$

$$u = -\delta \mathrm{sgn}(x_2\sigma) \tag{3.35}$$

where ξ is white noise disturbance bounded by $d \geq |\xi|$. Convergence of E to E^* is guaranteed when the virtual controller gain is chosen such that $|\delta - \delta^*| \leq d$ and where $\delta^* \leq \delta$. And convergence of E^* to E_{des} is guaranteed by the equations of Section 3.3.1. This controller is therefore robust to a disturbance as long as the disturbance is less than the arbitrarily small limit of the control input.

Figure 3.6 shows the states of the virtual system and actual system over time. The virtual system shows the same profile as seen in Figure 3.4. However the actual system converges the the virtual system and follows it in sliding mode. The actual controller has a higher control effort than the virtual controller and so can be seen switching the entire time. The actual system is therefore able follow the virtual system path despite the disturbance. Figure 3.7 shows the same results in state space. The final desired energy level is the same as Figure 3.5, however the virtual sliding surface is created by the path of the virtual system. The actual system path converges to the virtual sliding surface and follows it to the final desired energy level. Again, in this case the desired energy level passes through an equilibrium point so the control drives the pendulum to a fixed position.

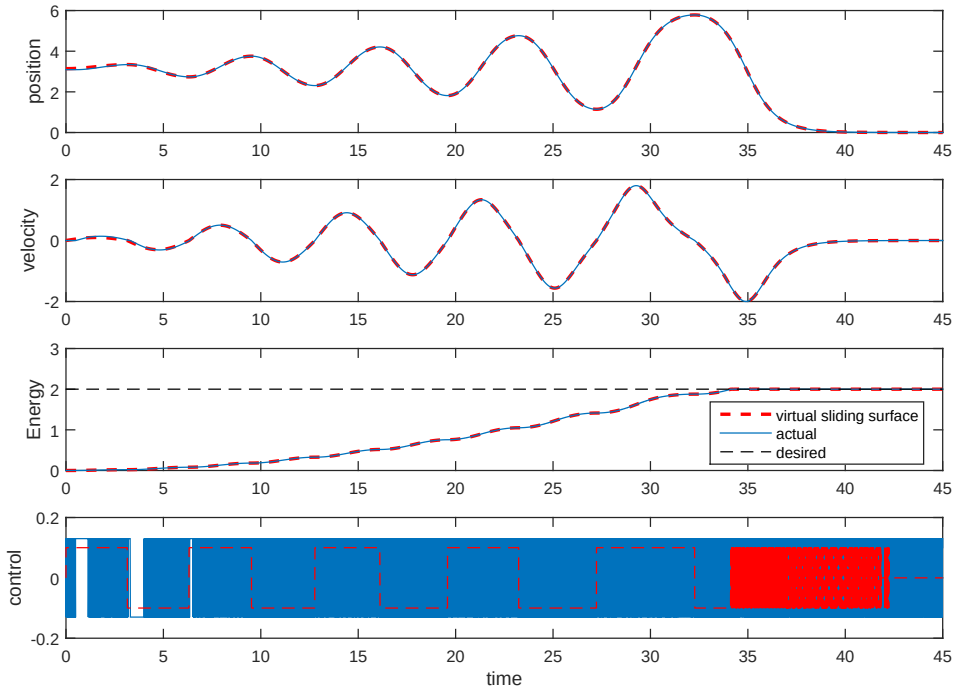

Figure 3.6: Inverted pendulum time profile results. Angular position and velocity, states x_1 and x_2, the actual states follow the virtual states. Total energy of the actual system slides along the virtual total energy which is in turn driven to desired energy. Arbitrarily small control input limited to $\delta^* = \pm 0.1$, $\delta = \pm 0.13$.

3.3.3 Synchronization Control

Sections 3.3.1 and 3.3.2 purposely chose a desired energy level that contained an equilibrium point so the control goal could be a fixed point. However, in general any energy level not through an equilibrium will produce a final state of the pendulum swinging back and forth. So a more interesting control goal is to reach a desired energy level and a desired position at a particular time. This control goal can be defined as driving a chase pendulum to synchronize its state path over time with an uncontrolled identical target pendulum.

The chase pendulum should be driven to match the amplitude and phase of an

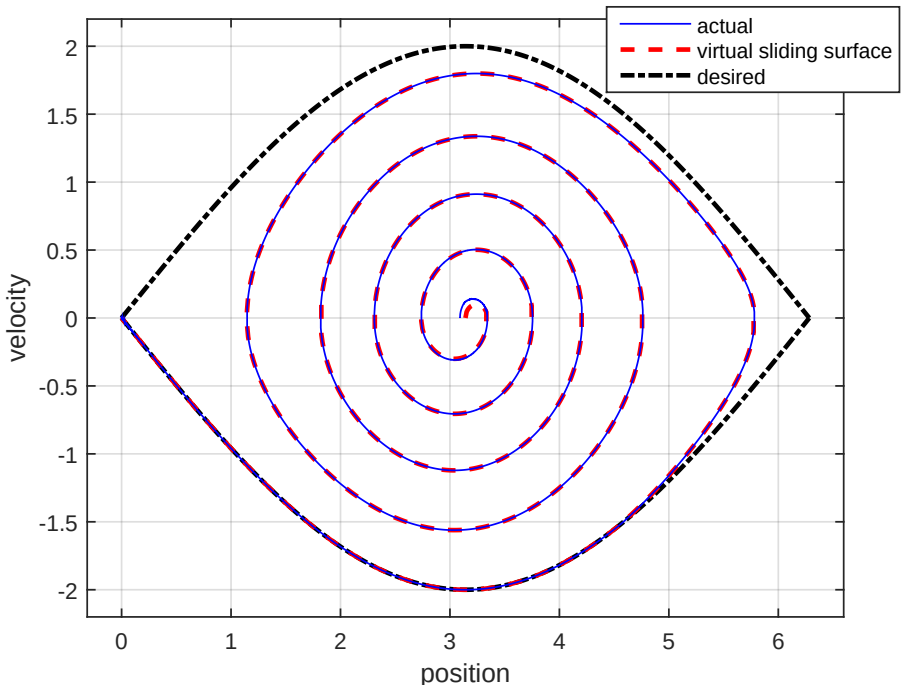

Figure 3.7: Inverted pendulum state space results. Angular position and velocity, states x_1 and x_2 driven to the virtual sliding surface, $\sigma^*(\mathbf{x})$, which is in turn driven to the desired sliding surface $\sigma(\mathbf{x})$.

identical uncontrolled target pendulum. In order to control the time at which the pendulum crosses any particular point, it is necessary to amend the control law to include some position state feedback. The target pendulum system state and energy is defined by the superscript $()^*$ as

$$\begin{aligned} \dot{x}_1^* &= x_2^* \\ \dot{x}_2^* &= \tfrac{g}{l} \sin x_1^* \end{aligned} \tag{3.36}$$

$$E^* = \frac{1}{2} m l^2 x_2^{*2} + mgl(\cos x_1^* + 1) \; . \tag{3.37}$$

The chase pendulum system state and energy is defined as

$$\begin{aligned} \dot{x}_1 &= x_2 \\ \dot{x}_2 &= \tfrac{g}{l}\sin x_1 + \tfrac{1}{ml^2}u_k \end{aligned} \tag{3.38}$$

$$E = \frac{1}{2}ml^2{x_2}^2 + mgl(\cos x_1 + 1) \tag{3.39}$$

where u_k is the control input with multiple stages. The first stage is to match the target's energy using the same method as described in Section 3.3.1. The sliding surface is defined as

$$\sigma(\mathbf{x}) = (E - E^*) = 0 \tag{3.40}$$

once the energy control converges, the amplitudes of the two pendulums will match but their motions may be out of phase. Since the motion is periodic, it is not enough to define the error based only on position. The chase and target pendulums will be in phase when both the position and velocity states are matched simultaneously. We propose the state vector error to be defined as

$$\bar{\mathbf{x}} = \|(\mathbf{x} - \mathbf{x}^*)\| = \sqrt{(x_1 - x_1^*)^2 + (x_2 - x_2^*)^2}\ . \tag{3.41}$$

This provides a feedback measurement, but we still need a feedback law. By choosing a control law as function of the position state, it is possible to adjust the period of the system so it is slightly different from the target system, while the total energy only cycles. For example, the natural dynamics of a harmonic oscillator, $\ddot{x} = \omega \sin x + u$, has a period, $T = 2\pi\omega^{-1/2}$. If you input a control function, $u = -k \sin x$, the dynamics

become

$$\ddot{x} = \omega \sin x - k \sin x$$

$$\ddot{x} = (\omega - k) \sin x \ .$$

Thereby, altering the period by some amount, $T = 2\pi(\omega - k)^{-1/2}$, the total energy will also oscillate with the same period, but will return to the initial energy after each cycle. This control law will shift the period of the chase pendulum to be different from the target pendulum. This will allow the phase of the chase to shift slowly over time until it matches that of the target.

Therefore, the control law is proposed with three different states, one for energy control, one for phasing control, and an off state

$$u_k = \begin{cases} u_1 = -\delta \text{sgn}(x_2 \sigma(\mathbf{x})) \\ u_2 = -\delta \sin(x_1 + \pi) \\ u_3 = 0 \ . \end{cases} \tag{3.42}$$

The control states will be used in succession based on the following state feedback logic

$$u = \begin{cases} u_1 & \text{, until} \quad |\sigma(\mathbf{x})| \leq \epsilon_1 & \text{, then} \\ u_2 & \text{, until} \quad \bar{\mathbf{x}} \leq \epsilon_2 & \text{, then} \\ u_1 & \text{, until} \quad |\sigma(\mathbf{x})| \leq \epsilon_1 & \text{, then} \\ u_3 & \text{, if} \quad |\sigma(\mathbf{x})| < \epsilon_1 \end{cases} \tag{3.43}$$

where ϵ_1 is the energy error tolerance, and ϵ_2 is the phase error tolerance. The second usage of u_1 is to re-drive the system to the target energy if the phasing is completed

not at the end of a full control cycle.

The pendulum synchronization is simulated for the chase system (3.38) and target sytem (3.36) with $\delta = 0.15$, $\epsilon_1 = 10^{-5}$ and $\epsilon_2 = 2 \cdot 10^{-3}$. Energy control stage using u_1 increases the energy of the chase to match the target, as seen in Figure 3.8 (before point $S1$), and the spiral stage in Figure 3.9. The phasing stage using u_2 cycles the total energy, slowly shifting the phase, as the total error goes to zero, as shown in Figure 3.8 (from point $S1$ to point $S2$), and in state space, Figure 3.9, the chase path (blue) is shifted away from the target path (black), changing the cycle time while still keeping two overlap point possibilities. The third stage using u_1 drives the chase energy back to the target energy because the target phase was reached before the energy had cycled back to the target (point $S2$ to point $S3$). The final stage using u_3 is to shut off the controlling allowing the two pendulums to remain synchronized with their identical natural dynamics.

3.4 Conclusions and Future Work

The energy control, robust energy control, and synchronization of a pendulum have been successfully achieved through simulation. All controllers are state feedback controllers. Future work would be to include some optimization to minimize the time or total control effort used. Particularly for synchronization in the phasing stage, the controller direction could be chosen in minimize the convergence time. Other future work would be to apply these controllers to multidimensional systems, and ultimately to the orbital model.

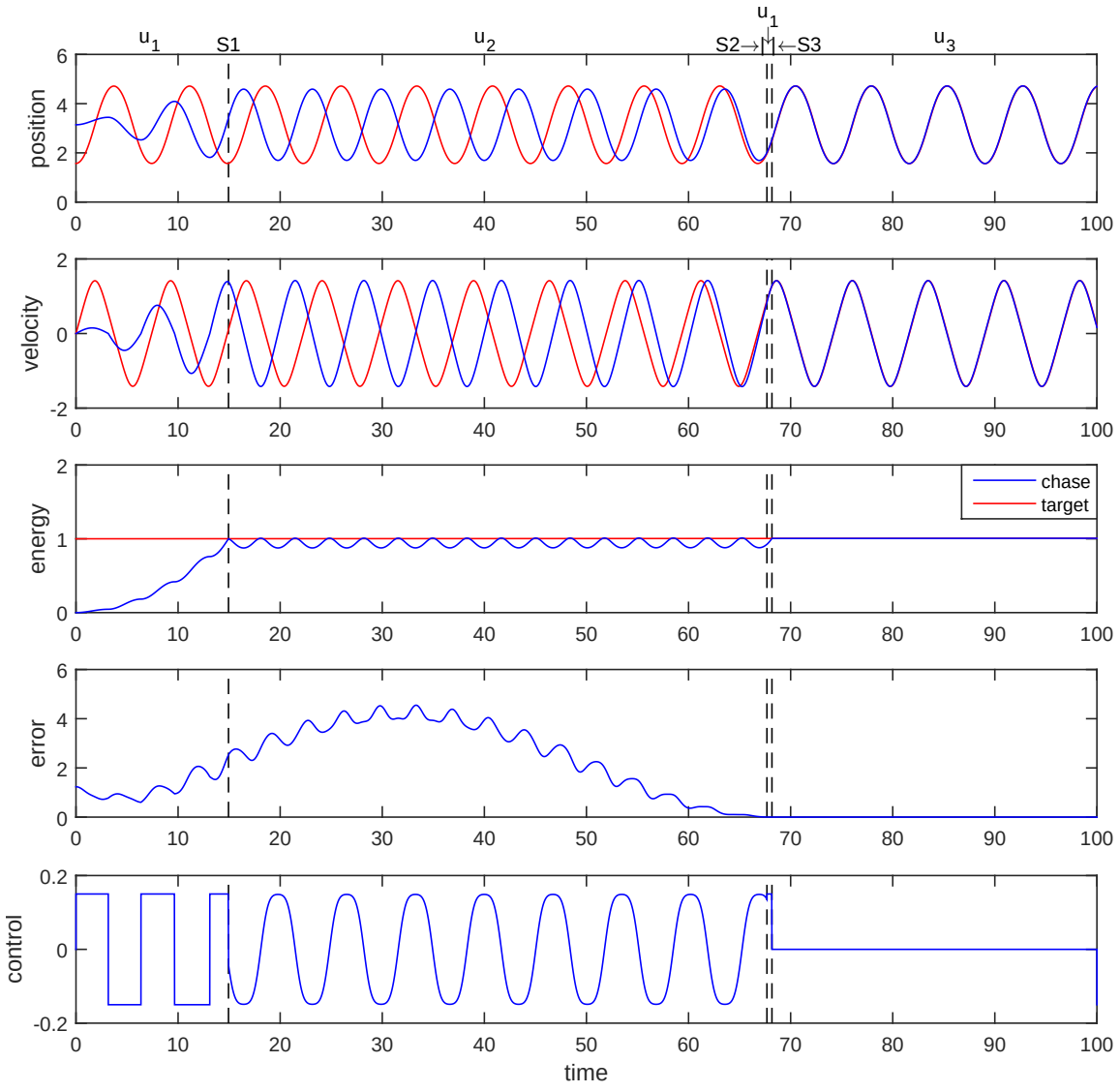

Figure 3.8: Inverted pendulum synchronization time profile results. Angular position and velocity, states x_1 and x_2, phase error is defined by $\bar{\mathbf{x}}$. Points $S1$ through $S3$ refer to the control stage switching points as defined by (3.43). Energy control, u_1, is used until target energy is reached (before $S1$). Phasing control, u_2, is used until chase and target phase is matched ($S1$-$S2$). Energy control is briefly reused to match target energy (after $S2$).

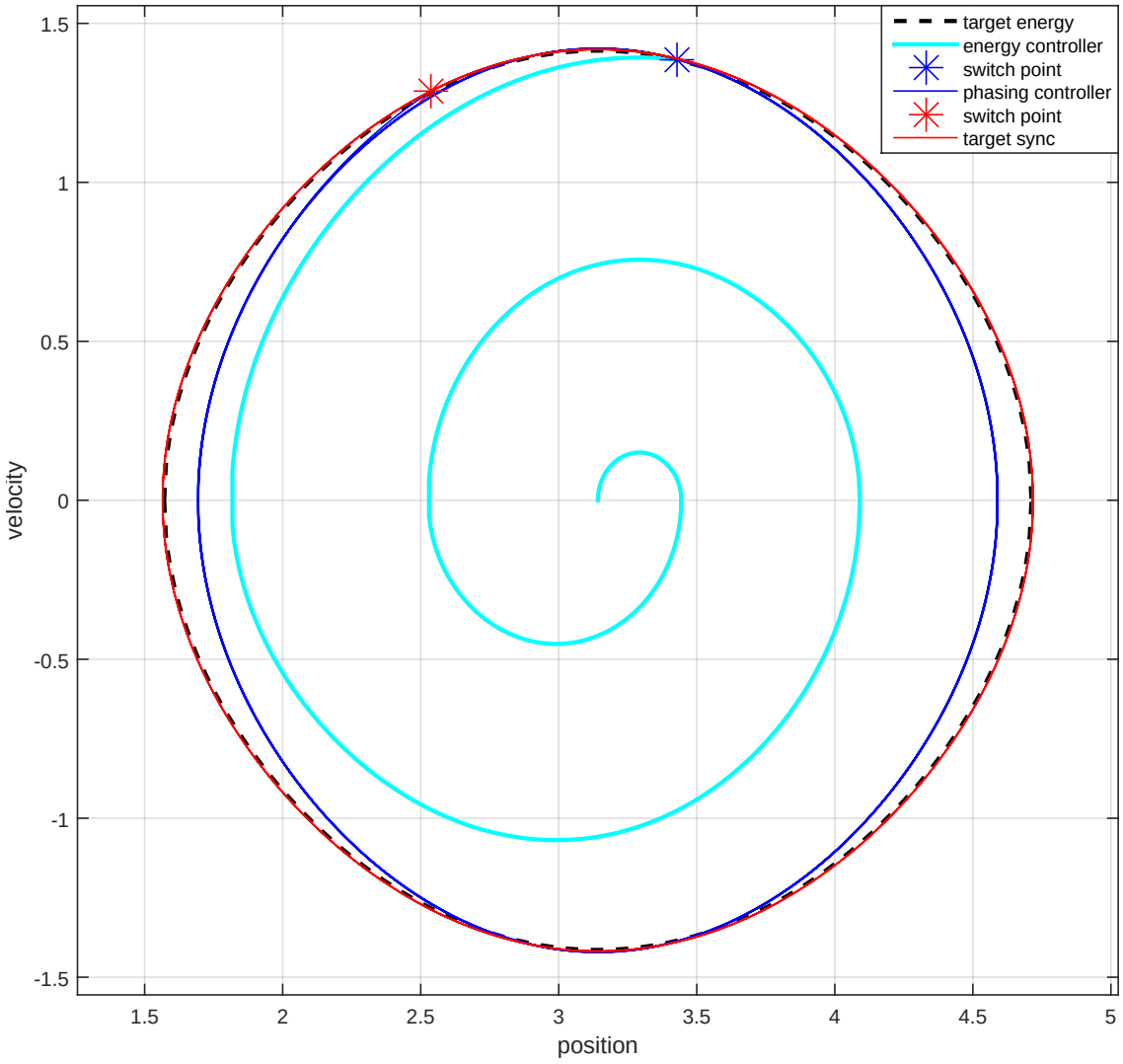

Figure 3.9: Inverted pendulum synchronization state space results. Angular position and velocity, states x_1 and x_2. Energy control drives the system to target energy (at the red switch point). Phasing controls alters the state space path until the chase and target intersect (at blue switch point).

Chapter 4

Cold Gas Fluid Modeling

In this chapter the fluid model is developed to be used in Chapters 6 and 7. The primary components of a cold gas propulsion system include a high pressure propellant storage vessel, a regulator to down-step and control pressure, solenoid valves for fast on/off switching, and thrusters to accelerate gas flow (Makled et al., 2009; Anis, 2012; Furumo, 2013).

The cold gas fluid model is developed as a series of control volumes connected by orifices. The flow is considered to be isentropic and adiabatic. The cold gas system is represented by first order ordinary differential equations of pressure and mass flow. The thrust characteristics are obtained using the rocket thrust equations. The dynamic model includes the response time characteristics of the pressure regulator and the solenoid valve. An accumulation volume is added after the regulator to help keep downstream pressure constant as multiple thrusters simultaneously demand mass flow during space flight maneuvers. The general, single stream schematic of a cold gas propulsion system is shown in Figure 4.1.

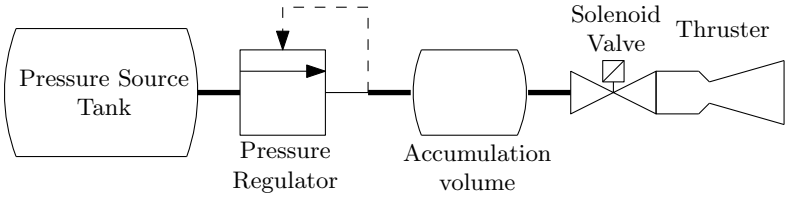

Figure 4.1: General schematic of a cold gas system.

4.1 Modeling Components

4.1.1 Control Volumes

The modeling begins generically by treating the system as a series of control volumes (CV) connected by small orifices. Each volume is modeled by pressure and mass change over time, $\dot{P}$ and $\dot{m}$, respectively. The pressure is governed by the ideal gas law,

$$P_i V_i = m_i R T_i \tag{4.1}$$

where P is pressure, V is volume, m is mass, and T is temperature, of the gas, and R is the specific gas constant. The subscript i represents the index for each volume. The volumes are constant and the temperatures are considered constant as the pressure changes in the tank is slow relative to heat exchange with the environment. Taking the time derivative of (4.1) yields

$$\dot{P}_i = \frac{R T_i}{V_i} \dot{m}_i \ . \tag{4.2}$$

The total mass flow rate, $\frac{dm}{dt} = \dot{m}$, is the sum of mass flow in and out of each volume as

$$\dot{m}_i = \sum \dot{m}_{\text{in}} - \sum \dot{m}_{\text{out}} \ . \tag{4.3}$$

Since the connections between control volumes could be pressure regulators, valves, turbines, thrusters, or other, the mass flow rate through each connection must be modeled accordingly.

4.1.2 Orifice Mass Flow

For isentropic, quasi-steady-state, subsonic flow through an orifice, the mass flow rate is given by (S. Drakunov, Hanchin, Su, & Özgüner, 1997)

$$\dot{m} = C_d A P_u \sqrt{\frac{2\gamma}{RT_u(\gamma-1)}\left[\left(\frac{P_d}{P_u}\right)^{\frac{2}{\gamma}} - \left(\frac{P_d}{P_u}\right)^{\frac{\gamma+1}{\gamma}}\right]} \tag{4.4}$$

where subscripts u and d represent the upstream and downstream conditions, respectively, A is the cross-sectional area of the orifice, C_d is the coefficient of discharge, and $\gamma = \frac{c_p}{c_v}$ is the ratio of specific heats. The coefficient of discharge is equal to one for the ideal case.

4.1.3 Nozzle

A converging-diverging nozzle can accelerate the gas to supersonic velocities through isentropic expansion. Supersonic flow will occur when the pressure differential is large enough given as

$$\frac{P_c}{P_a} \geq \left(\frac{\gamma+1}{2}\right)^{\frac{\gamma}{\gamma-1}} \tag{4.5}$$

such that the gas flow will be choked at the throat and accelerated to be supersonic at the exit. The exit conditions for Mach number M, pressure P, temperature T,

and velocity v, can be calculated from the following rocket thrust equations

$$\frac{A_e}{A_t} = \frac{1}{M_e}\sqrt{\left(\frac{2}{\gamma+1}\right)\left(1+\frac{\gamma-1}{2}M_e^2\right)^{\frac{\gamma+1}{\gamma-1}}} \tag{4.6}$$

$$\frac{P_e}{P_c} = \left(1+\frac{\gamma-1}{2}M_e^2\right)^{-\frac{\gamma}{\gamma-1}} \tag{4.7}$$

$$\frac{T_e}{T_c} = \left(1+\frac{\gamma-1}{2}M_e^2\right)^{-1} \tag{4.8}$$

$$v_e = M_e\sqrt{\gamma R T_e} \tag{4.9}$$

where $\epsilon = \frac{A_e}{A_t}$ is the cross section area expansion ratio, subscripts c, t , and e represent the chamber, throat, and exit conditions, respectively, and P_a is the ambient pressure, see Figure 4.2. The Mach number is numerically calculated from the expansion ratio. The mass flow rate, dependent only on upstream conditions for supersonic flow, and the thrust force F, are then calculated as

$$\dot{m} = A_t P_c\sqrt{\frac{\gamma}{RT_c}\left(\frac{2}{\gamma+1}\right)^{\frac{\gamma+1}{\gamma-1}}} \tag{4.10}$$

$$F = \dot{m}v_e + (P_e - P_a)A_e \tag{4.11}$$

see (Sutton & Biblarz, 2001) or (Benson, 2014).

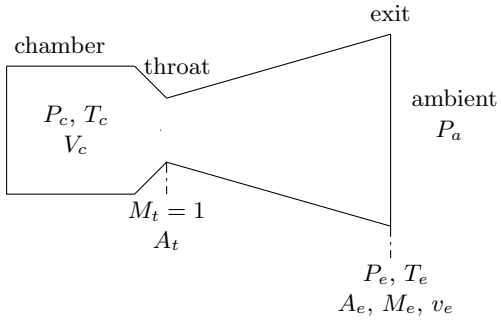

Figure 4.2: Converging-diverging nozzle.

4.1.4 Regulator

A regulator consists of a series of orifice flow and control volumes. In order to maintain a constant downstream pressure, the regulator employs a variable downstream control volume. The volume and subsequent orifice area depends on the balance of a spring force and the pressure difference between a reference pressure and the regulated pressure. This is accomplished by the balancing forces controlling the position of a diaphragm and poppet that simultaneously defines the volume and mass flow area past a poppet. Schematic is shown in Figure 4.3. The sum of the forces on the

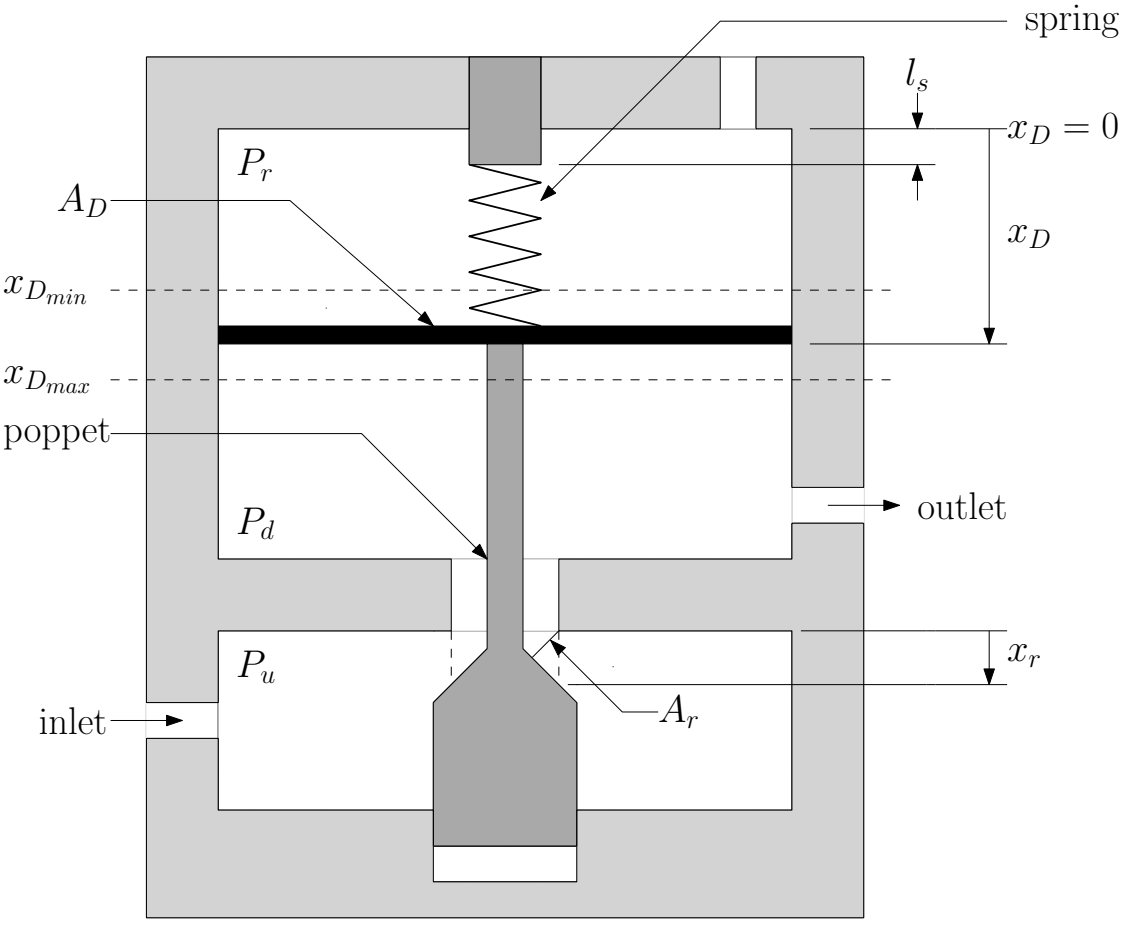

Figure 4.3: Schematic of a general spring loaded pressure regulator.

poppet are

$$M\ddot{x}_r = F_{\text{spring}} + F_{\text{friction}} + F_{\text{diaphram}} + F_{\text{flow}} \tag{4.12}$$

$$M\ddot{x}_r = -k(x_r - l_s) - b\dot{x}_r - A_D(P_d - P_r) + 0 \tag{4.13}$$

where x_r is the position of the poppet, k is the spring constant, b is the coefficient of kinetic friction, l_s is the set spring length, A_D is the diaphragm area, P_d is the downstream pressure, P_r is the reference or sense pressure, and the flow force is considered negligible.

An the regulator dynamics of (4.13) is approximated by a reduced differential equation and by having the many physical parameters of the full regulator combined into just a few tunable parameters. Many of the physical parameters are difficult to know, and may be highly dependent on a specific regulator. Instead our goal is to model a regulator in general. The approximate regulator is modeled only as a single variable orifice.

If we assume that the moving poppet mass is small, the acceleration term can be considered negligible thereby reducing the order of the equation as

$$0 = -k(x_r - l_s) - b\dot{x}_r - A_D(P_d - P_r) \ . \tag{4.14}$$

The pressure applied by the spring is $P_s = \frac{k}{A_D} l_s$ so (4.14) becomes

$$b\dot{x}_r = -kx_r - A_D(P_d - P_r - P_s) \ . \tag{4.15}$$

To transfer focus from poppet position to orifice area we will assume a linear relation as $A_r = c_r x_D$ where $c_r = \frac{A_{r\max}}{x_{r\max}}$. Additionally let $\tau_r = \frac{b}{k}$, and $k_r = \frac{A_D c_r}{k}$, then the

pressure regulator orifice area is described as

$$\tau_r \dot{A}_r = -A_r - k_r(P_d - P_r - P_s) \tag{4.16}$$

with two constant tunable parameters, the time constant, τ_r, and constant k_r.

A full regulator fluid model is simulated numerically in MATLAB and Simulink to compare to the approximate model. Figure 4.4 shows that the approximation model of a regulator can produce the same dynamics as the full regulator model.

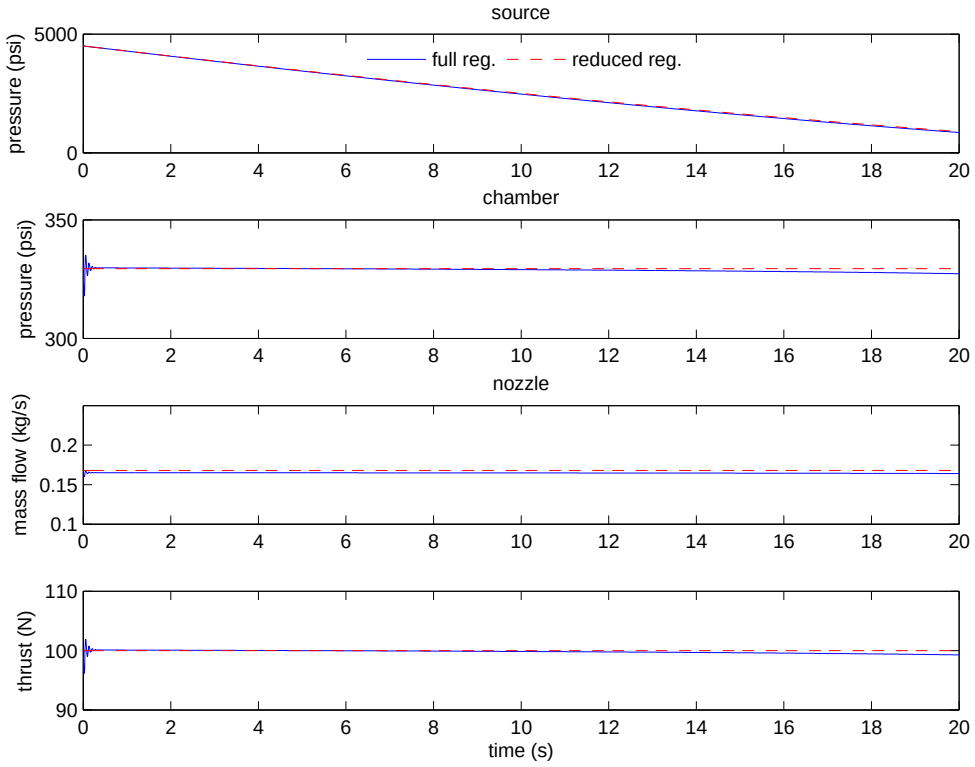

Figure 4.4: Full regulator model and approximate regulator model dynamics comparison.

The desired pressure may be input as the reference pressure ($P_r = P_{\text{des}}$, $P_s =$ constant), or as the spring set length ($P_s = P_{\text{des}}$, $P_r = P_a$). This mechanical system

will naturally drive the downstream pressure, P_d, to the desired pressure, P_{des}. The desired pressure is input into the regulator by setting the reference pressure or adjusting the spring set position, usually the latter. Since only one input is used at a time there may be a steady state error bias as seen in the steady state

$$0 = -A_r + k_r P_r - k_r \cancelto{0}{(P_d - P_{\text{des}})} \tag{4.17}$$

so the dynamics are only stable at the desired pressure for a particular reference pressure. Without control of both the spring and pressure inputs, it is not possible to drive the system to any pressure by directly feeding in the desired value as one of the two inputs. To generalize one step further, the pressure inputs can be written as one variable as,

$$\tau_r \dot{A}_r = -A_r - k_r(P_d - P_r) \tag{4.18}$$

with two constant tunable parameters, the time constant τ_r, and constant k_r, where A_r is the orifice area, P_d is the downstream pressure and P_r is the manually controlled desired downstream pressure.

A regulator component is therefore modeled as an orifice with subsonic mass flow governed by (4.4), with a variable orifice area governed by (4.18) and limited by $0 < A_r < A_{r_{\max}}$.

4.1.5 Solenoid Valve

The solenoid valve provides a control input to the cold gas system. A solenoid valve is used to provide fast on/off switching. The solenoid valve area is determined by an electrically driven poppet. The poppet is fully closed when no voltage is applied and

can only be commanded to be fully open by applying a sufficient voltage. This discrete control input means the valve area is either zero or a maximum. The valve is usually placed upstream from a reaction control thruster. When the valve is commanded open the maximum area will allow the chamber pressure of the thruster to increase until it reaches the upstream pressure.

Because the valve does not open or close instantaneously, any response delay or rise time must be modeled. The solenoid valve component is therefore modeled as an orifice with subsonic mass flow governed by (4.4), a variable area limited by $0 < A_r < A_{r_{\max}}$, and a predetermined time response profile as shown in Figure 4.5.

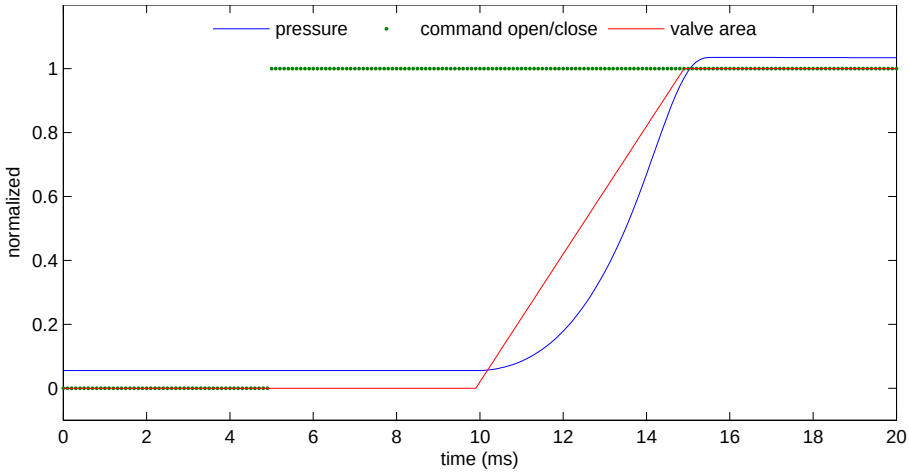

Figure 4.5: Solenoid valve time response.

4.2 Direct Feed Versus Constant Feed

The cold gas propulsion system shown in Figure 4.1 represents a constant feed system because the regulator provides a constant downstream pressure, and therefore thrust, as the tank pressure drops. The least complex version of the cold gas system would be

a nozzle attached directly to a pressure tank, as shown in Figure 7.2. This represents a direct feed system. In this case the tank pressure becomes the thruster chamber pressure, and so the thrust is directly dependent on the tank pressure state which decreases when used. This system reduces the component complexity but it increases the order of state equations needed to determine optimal control.

Direct feed is such that the chamber pressure is equal to the tank pressure and will maximize the thrust at any time by using all available potential energy, but the thrust will decrease over time as tank pressure drops. A constant feed uses a regulator to provide a constant chamber pressure and thrust until the tank pressure drops below the desired constant chamber pressure, and tank pressure drop will be slowed.

To compare the two cases, the tank pressure, $P_s(t)$, specific impulse, $I_{sp}(t)$, and $\Delta v(t)$ performance metrics need to be found as functions of time.

For a given gas propellant, tank and nozzle dimensions, and environment, there are many constant parameters, A_t,M_e, γ, A_e, P_a, R_s, T_c, V_c. In this case the only control volume is the tank/thruster chamber, and the only mass flow is the supersonic nozzle mass flow out of the control volume. The fluid model can be written as

$$F = C_1 P_c + C_4 \tag{4.19a}$$

$$\dot{m} = C_2 P_c \tag{4.19b}$$

$$P_s = C_3 m \tag{4.19c}$$

$$\dot{P}_s = -C_3 \dot{m} \tag{4.19d}$$

where

$$C_1 = A_t M_e \gamma \left(\frac{2}{\gamma+1}\right)^{\frac{\gamma+1}{2(\gamma-1)}} \left(1+\frac{\gamma-1}{2}M_e^2\right)^{-\frac{1}{2}} + A_e \left(1+\frac{\gamma-1}{2}M_e^2\right)^{-\frac{\gamma}{\gamma-1}} \tag{4.20a}$$

$$C_4 = -A_e P_a \tag{4.20b}$$

$$C_2 = A_t \sqrt{\frac{\gamma}{R_s T_c}\left(\frac{2}{\gamma+1}\right)^{\frac{\gamma+1}{\gamma-1}}} \tag{4.20c}$$

$$C_3 = \frac{R_s T_c}{V_c}\,. \tag{4.20d}$$

Direct feed The simplest component configuration of a cold gas propulsion system is one that attaches a nozzle directly to a pressure tank. The tank is the thruster chamber, and so $P_s \equiv P_c$, which decreases as the tank pressure is used. The pressure can be solved by substituting (4.19b) into (4.19d) with $P_c = P_s$ and solving for $P_s(t)$. The thrust can be solved by substituting $P_s(t)$ into (4.19a). The pressure profile is derived as

$$P_s(t) = P_0 e^{-C_3 C_2 t} \tag{4.21}$$

where P_0 is the initial tank pressure and the pressure and thrust profiles can be seen in Figure 4.6.

Constant feed The constant feed configuration will hold the chamber pressure constant using a regulator so that $P_c = P_C$ until the tank pressure falls below the chosen constant, $P_s \leq P_C$, which will occur at time, t_1. This case will give a lower thrust but for a longer time because the tank pressure drop is slowed. Once the tank pressure falls below the chosen chamber pressure, the thank pressure and chamber will decrease together the same as the direct feed case.

For the constant feed case the mass flow out of the tank is ultimately be determined by the nozzle mass flow and so the tank pressure can be solved by substituting (4.19b) into (4.19d) with $P_c = P_C$, where P_C is the chosen constant chamber pressure, and solving for $P_s(t)$ for $0 \leq t \leq t_1$. For $t > t_1$, the pressures are derived the same as the direct feed case with $P_s = P_c = P_C$ at time t_1. The tank pressure profile is found to be

$$P_s(t) = \begin{cases} P_0 - C_3 C_2 t & \text{for } t < t_1 \\ P_C e^{-C_3 C_2 (t - t_1)} & \text{for } t > t_1 \end{cases} \tag{4.22}$$

and the chamber pressure profile is

$$P_c(t) = \begin{cases} P_C & \text{for } t < t_1 \\ P_C e^{-C_3 C_2 (t - t_1)} & \text{for } t > t_1 \end{cases} \tag{4.23}$$

where

$$t_1 = \frac{P_0 - P_C}{C_3 C_2 P_C} \, . \tag{4.24}$$

The pressure and thrust profiles can be seen in Figure 4.6.

Specific impulse performance Specific impulse measures the fuel efficiency by comparing the total thrust produced by the total fuel used by mass, given as

$$g_0 I_{\text{sp}} = \frac{\int_0^t F(t) dt}{\int_0^t \dot{m}(t) dt} \, . \tag{4.25}$$

This can be solved directly from the time dependent thrust and mass flow equations (4.20), (4.21), (4.23) and (4.24) in the previous paragraphs.

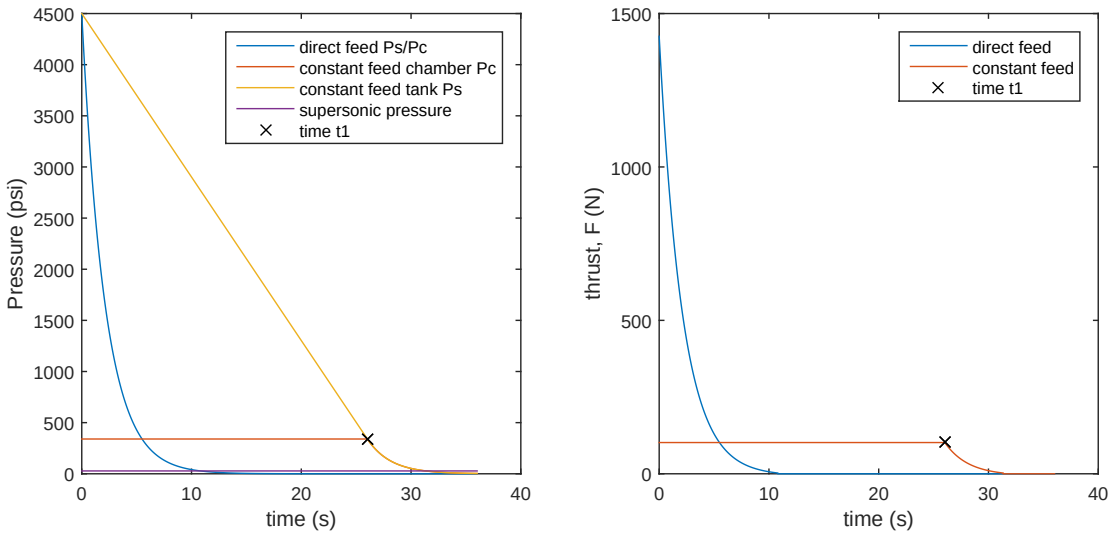

Figure 4.6: Pressure and thrust profiles comparing the direct and constant feed cases.

The specific impulse for the direct feed case is

$$g_0 I_v = \frac{C_1}{C_2} + C_4 \frac{C_3 t}{P_0(1 - e^{C_3 C_2 t})} \tag{4.26}$$

and the specific impulse for the constant feed case is

$$g_0 I_c = \frac{C_1}{C_2} + C_4 \times \begin{cases} \frac{1}{P_C} & \text{for } t < t_1 \\ \frac{C_3 t}{C_3 C_2 P_C t_1 + P_C(1 - e^{C_3 C_2 (t - t_1)})} & \text{for } t > t_1 \ . \end{cases} \tag{4.27}$$

When the ambient back pressure is a vacuum, $P_a = 0$, the specific impulse is maxi-

mized and both cases become equivalent as $C_4 = 0$,

$$g_0 I_v = g_0 I_c = \frac{C_1}{C_2} \ .$$

The specific impulse for each case is compared in Figure 4.7. In both cases, the efficiency is maximum when the atmospheric pressure is a vacuum. The efficiency of the direct feed case decreases over time with the tank pressure drop. However, the constant feed case provides maximum efficiency until the tank pressure drops below the chosen fixed chamber pressure. After this the specific impulse of the constant feed case drops and converges to the direct feed case.

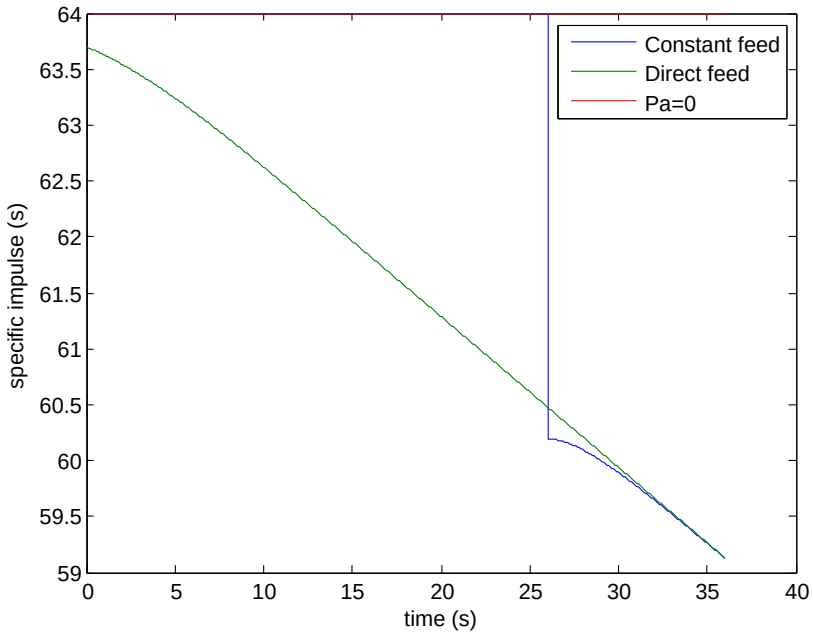

Figure 4.7: Fuel efficiency of the direct feed case versus the constant feed case.

Delta v performance To measure the performance of the spacecraft motion due to a thrusting maneuver, the change in velocity provided by a change in fuel mass can be calculated by

$$\Delta v = \int_0^t \frac{F(t)}{m(t)} dt \ . \tag{4.28}$$

Let the total mass, m, be equal to the mass of the spacecraft plus the mass of the remaining fuel at time t as $m = M_{\text{sc}} + M_{\text{fl}}$.

For the direct feed case Δv is calculated as

$$\Delta v_v = \int_0^t \frac{C_1 P_0 e^{-C_3 C_2 t} + C_4}{M_{\text{sc}} + \frac{P_0}{C_3} e^{-C_3 C_2 t}} dt \tag{4.29}$$

and for the constant feed case Δv is

$$\Delta v_c = \int_0^{t_1} \frac{C_1 P_C + C_4}{M_{\text{sc}} + \frac{P_0}{C_3} - C_2 P_C t} dt + \int_{t_1}^t \frac{C_1 P_C e^{-C_3 C_2 (t - t_1)} + C_4}{M_{\text{sc}} + \frac{P_C}{C_3} e^{-C_3 C_2 (t - t_1)}} dt \ . \tag{4.30}$$

To compare both cases, (4.29) and (4.30) can be integrated numerically, or, Δv can be calculated numerically as

$$v_{i+1} = v_i + \frac{1}{M_{\text{sc}} + M_{\text{fl}_i}} F_i dt \ . \tag{4.31}$$

As shown in Figure 4.8, the direct feed case can provide a much faster gain in Δv, while the constant feed case can provide an overall larger Δv. This would make the constant feed case fuel optimal, and the direct feed case time optimal. For cases when the spacecraft mass is much much larger than the fuel mass, the total Δv from the direct feed case will be larger than constant feed case.

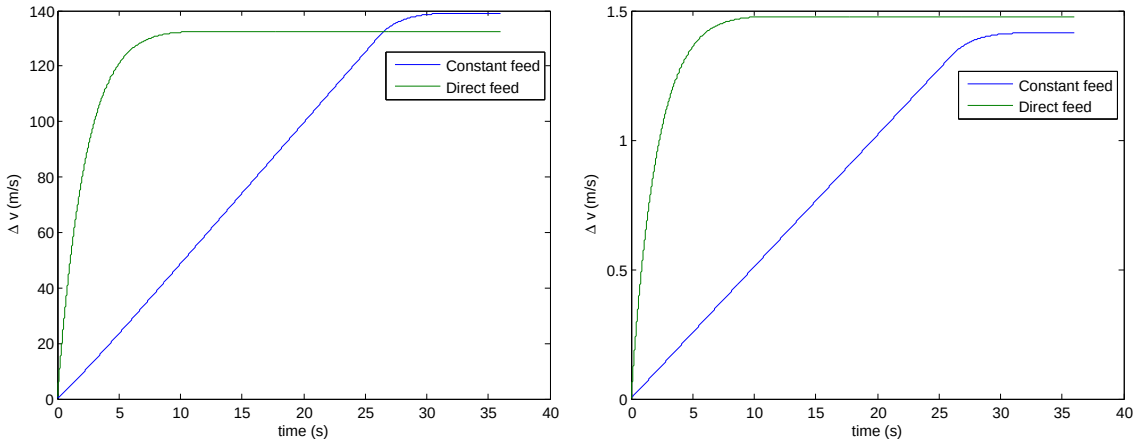

(a) (b)

Figure 4.8: Δv gain over time for the case of direct feed versus constant feed. (a) $M_{\text{sc}} = 20$, $M_{\text{fl}} = 5$ (b) $M_{\text{sc}} = 2000$, $M_{\text{fl}} = 5$.

4.3 Efficiency

We would like the fuel to last as long as possible. The properties of the gas chosen or the nozzle design may be used to maximize cold gas performance. To begin, the metric for maximum performance must be defined. This Section explores fuel efficiency and maximum flight time. The system constraints must also be defined, such as fuel, pressure, volume, temperature, or mass.

4.3.1 Nozzle Design

A converging-diverging nozzle is used to accelerate the exiting gas by converting the internal energy of the gas into kinetic energy through the process of isentropic expansion. The nozzle is ideally designed so that each gas particle exits the nozzle normal to the exit plane at maximum velocity. The inlet chamber parameters of pressure P_c, and temperature T_c, along with nozzle parameters of throat area A_t, and

nozzle expansion ratio $\frac{A_e}{A_t}$, can be chosen or designed to maximize thrust.

For given inlet conditions there exists an optimal nozzle expansion ratio. This can be seen by calculating the thrust force for a range of expansion ratios. As the exiting gas is allowed to expand with a greater expansion ratio, the exit velocity increases while the exit pressure decrease. As seen in Figure 4.9, the maximum thrust occurs when the exit pressure is made equal to the ambient pressure P_a. Therefore, it is optimal to chose an expansion ratio that provides an exit pressure that is equal to the ambient pressure.

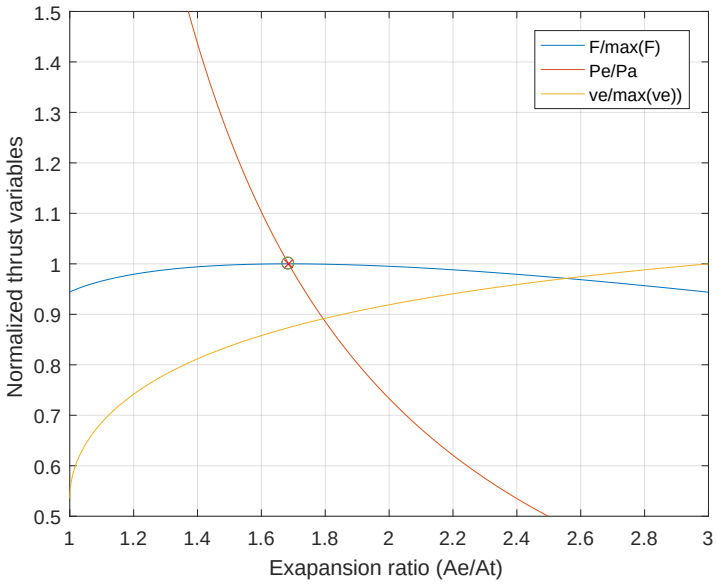

Figure 4.9: Thrust is maximized when with a nozzle expansion ratio that creates an exit pressure equal to the ambient pressure.

4.3.2 Specific Impulse

Propellant

Specific impulse I_{sp}, is a property commonly used to compare the efficiency of different rocket fuels. The average specific impulse is the measure of total thrust gained from the total weight of fuel used,

$$I_{\text{sp}} = \frac{\int_0^t F dt}{g_0 \int_0^t \dot{m} dt} \tag{4.32}$$

where g_0 is the Earth's gravitational acceleration at sea level. For chemical reactive fuels, specific impulse is experimentally determined by measuring thrust over time and measuring the initial and final fuel mass.

For a cold gas system all energy conversions are described in Section 4.1 so it is possible to analytically determine the specific impulse for different cold gas propellants and initial conditions. For steady state conditions, the average specific impulse is the same as the instantaneous specific impulse given as

$$I_{\text{sp}} = \frac{F}{g_0 \dot{m}} \, . \tag{4.33}$$

For a nozzle with optimal expansion ratio, when $P_e = P_a$, the thrust equation (4.11) can be solved for exit velocity as $v_e = \frac{F}{\dot{m}}$. Therefore the specific impulse can be described simply as $I_{\text{sp}} = \frac{v_e}{g_0}$. For isentropic flow, the exit velocity is

$$v_e = \sqrt{\frac{2\gamma R_s T_c}{\gamma - 1} \left[1 - \left(\frac{P_e}{P_c} \right)^{\frac{\gamma - 1}{\gamma}} \right]} \tag{4.34}$$

and so

$$I_{\text{sp}} = g_0 \sqrt{\frac{2\gamma R_s T_c}{\gamma - 1}\left[1 - \left(\frac{P_e}{P_c}\right)^{\frac{\gamma-1}{\gamma}}\right]}. \tag{4.35}$$

From (4.35), cold gas propellant performance is understood as a function of molecular structure γ, molecular mass $R_s = R/M$, set chamber pressure P_c, and chamber temperature T_c. The contribution of each of the these parameters can be seen in Figure 4.10.

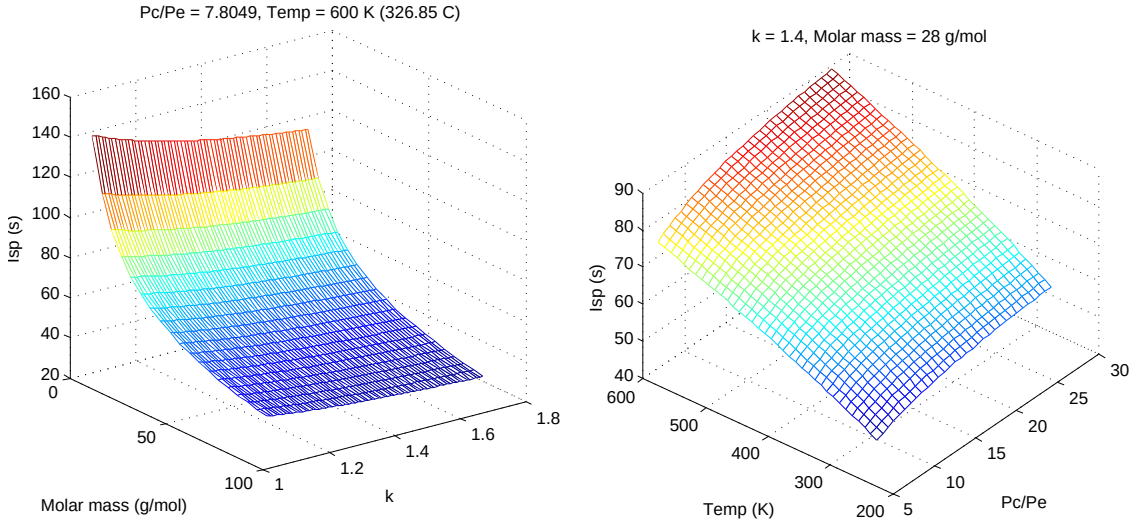

(a) (b)

Figure 4.10: Specific impulse relation to cold gas propellant parameters.

The two parameters set by a given gas type are γ and R_s. It is clear from Figure 4.10a that the specific impulse improves with gas molecules that have a small mass and small specific heat ratio. More importantly, it can be seen that the molar mass has a much more significant impact than the ratio of specific.

The other two parameters, chamber pressure and temperature, can be adjusted after choosing a gas type. As can be seen from Figure 4.10b, specific impulse im-

proves with higher pressure and temperature. Here it can also be concluded that the set temperature has a more significant impact than the set pressure. There is also a more subtle effect to distinguish between setting the chamber pressure and temperature. As can be seen in equations (4.19a),(4.20a), and (4.20b), chamber temperature will not determine the thrust force, but chamber pressure will. However, when designing for a given desired thrust, increasing the set chamber pressure can be offset by appropriately decreasing the nozzle throat area according to those equations.

4.3.3 Flight Time

One possible optimization criteria might be to maximize the total flight time of a vehicle before the propellant source is empty. For the cold gas propulsion the total flight time is defined as the total time the system can provide a constant thrust force. More specifically, the regulator will provide constant downstream pressure until the tank pressure decreases below the pressure required to provide the desired constant thrust.

Propellant Type

As shown in the Section 4.3.2, the specific impulse is improved by choosing a propellant with a lower molecular mass, and by heating the gas to a higher temperature. By choosing conditions for a higher specific impulse, we would hope to increase total flight time. However this may result in the opposite effect depending on the limiting factor for filling the pressure tank.

For example, a thruster with a chamber pressure regulated to 265 psia can produce a continuous thrust of 5 N until the tank pressure decreases from its initial pressure

Table 4.1: Tanks limited to a maximum pressure of 1200 psia. P_s and m are initial tank pressure and propellant mass.

Gas	M (g/mol)	P_s (psia)	T_s (^{o}C)	m (kg)	$\dot{m}$ (g/s)	flight time (s)
Air	29	1200	20	1.34	8.7	128
Air	29	1200	350	0.63	6.0	88
H2O	18	1200	350	0.40	4.6	70

Table 4.2: Spacecraft limited to maximum propellant mass of 1 kg. P_s and m are initial tank pressure and propellant mass.

Gas	M (g/mol)	P_s (psia)	T_s (^{o}C)	m (kg)	$\dot{m}$ (g/s)	flight time (s)
Air	29	897	20	1.00	8.7	89
Air	29	1907	350	1.00	6.0	150
H2O	18	3065	350	1.00	4.6	202

down to 265 psia. First consider the limiting factor for the tanks to hold a maximum pressure, as shown in Table 4.1. As the temperature is increased or the molar mass is decreased, the total initial mass of the gas is decreased and so total flight time is decreased. If the total mass of the propellant is the limiting factor, as shown in Table 4.2, then increasing the temperature or decreasing the molar mass will increase the initial pressure, and the total flight is increased.

Nozzle Throat Area

To maintain a constant thrust, a given chamber pressure determines the nozzle throat area needed to provide the desired thrust. If these parameters are free variables, they can be chosen to maximize the total flight time. As the throat area is decreased, the mass flow decrease will slow the tank pressure loss, however this will increase the needed chamber pressure to provide a desired thrust, therefore allowing less tank

pressure to be lost.

To find the maximum flight time, equation (4.24) along with (4.20) can be used to find the flight time for each throat diameter. The needed chamber pressure can be found from equation (4.19a) using a desired thrust. This is done using an optimal expansion ratio given the exit pressure is equal to the ambient pressure. Flight time as a function of nozzle throat diameter is seen in Figure 4.11. The results show that there is in fact an optimal throat area to maximize the flight time if the chamber pressure is a free parameter.

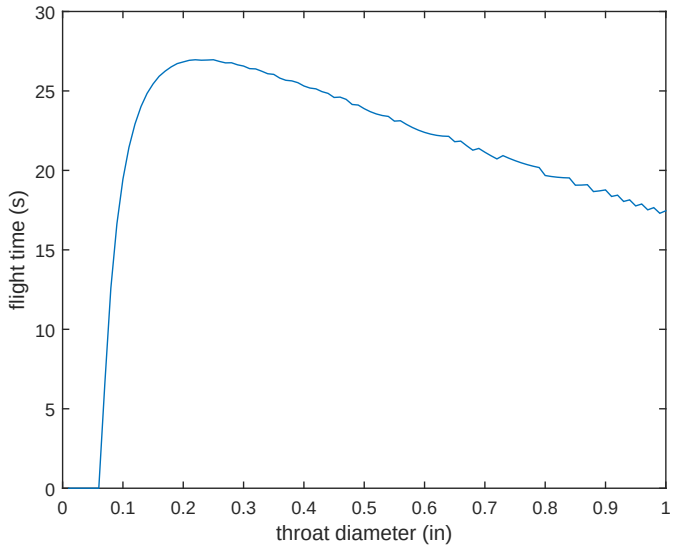

Figure 4.11: Optimizing flight time. Tank Pressure = 4500 psi, ambient Pressure = 14.7 psi, desired thrust = 100 N. Optimal throat diameter = 0.25 in, with chamber pressure = 329 psi. Maximum flight time = 27.0 s, and expansion ratio = 3.11.

Chapter 5

Cold Gas Propulsion for the Asteroid Free Flyer Project

The work in this Chapter was conducted under contract of the Asteroid and Lava Tube Free Flyer Project CIF, with testing performed at Swamp Works located at the Kennedy Space Center, NASA.

The project concept goal was to design a spacecraft that can control and stabilize attitude control using cold gas in microgravity. The propulsion system is a cold gas system. The goal of the research presented in this chapter is to design a cold gas thrust controller that can output a thrust equal to a desired thrust as commanded by an upper level attitude control system.

The Asteroid Free Flyer is designed with six thruster pods, two opposite facing thrusters on each pod, placed to give full control in three degrees of freedom, for a total of twelve thrusters. Each thruster is electrically controlled using a solenoid valve. Each thruster is designed to produce 1 N of thrust. Chamber pressure is determined

by a constant regulator upstream providing 100 psig to all twelve thrusters.

To demonstrate the attitude control in a flight configuration, the Free Flyer is placed in a multi-axis gimbol to allow three degrees of freedom for complete attitude control testing. Gas is stored onboard in two tanks. The tanks are filled to 2200 psig with N2 gas. The total tank volume is 13.6 L. Demonstration takes place under standard temperature pressure conditions. A picture is shown in Figure 5.1.

Bench testing was done to determine nozzle performance using a constant feed of shop air at 100 psig. Chamber pressure and thrust force were measured. Initially a single nozzle was tested, and then the full cold gas system was tested. The bench testing was also used to design and test the cold gas thrust controller.

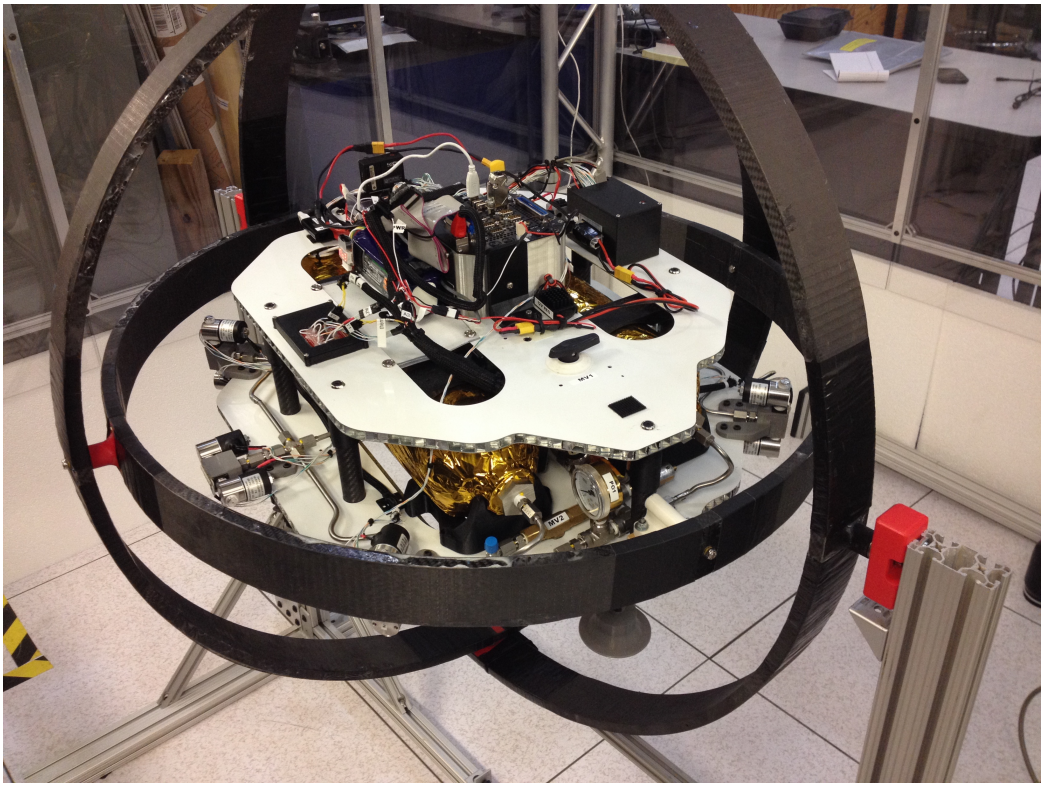

Figure 5.1: Asteroid Free Flyer in multi-axis gimbol test stand.

5.1 Nozzle Design

The Asteroid Free Flyer required 1 N of thrust per thruster and testing used shop air that had a maximum of 100 psig. With these parameters, under Earth sea level conditions, the rocket equations were used to optimize the nozzle dimensions, as well as calculate flow rates, shown in the Table 5.1. SCFM is Standard Cubic Feet per Minute.

Table 5.1: Single thruster for Asteroid Free Flyer.

Throat diameter	0.0455 ″
Expansion ratio	1.69
Exit Mach number	2.00
Mass flow	0.001934 kg/s
Volume flow rate	3.400864 SCFM

Based on Table 5.1, the nozzle was machined with a throat diameter of 0.05 ″. Due to the small size and material of the nozzle, it was machined as a cone. The cone shape slightly reduces the thrust performance from the ideal bell shaped nozzle. The performance factor can be calculated from the half angle of the cone, α, as

$$\frac{1}{2}\cos\alpha \tag{5.1}$$

A nozzle with a throat diameter of 0.07 ″ was also constructed for thrust performance testing.

Figure 5.2: Machined converging-diverging nozzle.

5.2 Control

For the Asteroid Free Flyer there was no direct measurement of the thrust force or chamber pressure, so there was no way to implement a feedback controller. Therefore, the common method of Pulse-Width-Modulation (PWM) was developed as an open loop control law for the cold gas thrusters.

The command is sent as a pulse train with a fixed frequency, where 0 and 1 are the solenoid closed and open commands, respectively. The width is modulated as a percentage of the cycle length. The average value over one cycle will be equal to duty cycle. The controller is designed to choose the duty cycle that makes the average thrust, over one cycle, to be equal to the desired thrust.

Since the average thrust is only valid over a full cycle, the system can only be commanded with a new desired thrust as fast as the frequency of the pulse signal. As seen Figure 5.3, the thrust profile does not follow the square pulse exactly because of the solenoid and thruster response times. Therefore, a look-up table is required to match the desired average thrust with the correct duty cycle.

As described in the next section, bench testing of the solenoid valve and thruster

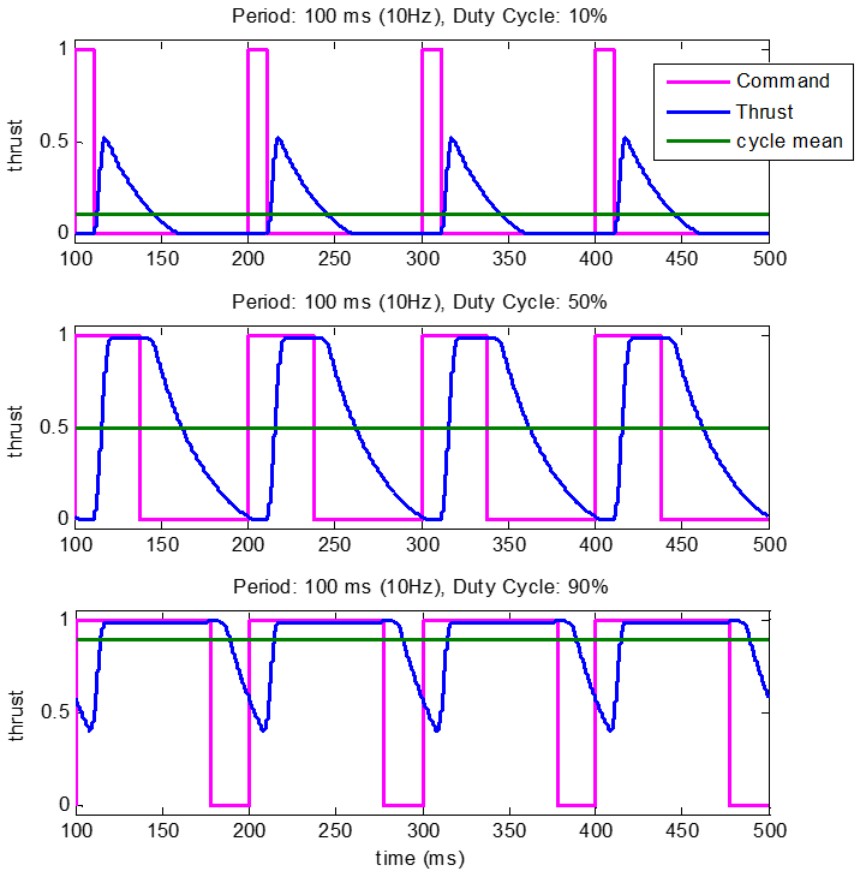

Figure 5.3: PWM command as it effects thrust profile and thrust average.

was done to properly characterize the thrust response. This information was used to update cold gas model so it could be used to help choose the right frequency. Further, bench testing was done to create the thrust to duty cycle look-up table and test the PWM controller.

5.3 Bench Testing

5.3.1 Test Stand

A test stand was built to measure thrust and pressure of a single thruster pod in order to characterize the performance of the solenoid valve and the nozzle. This data was used to parameterize the cold gas model to match the hardware, which in turn was used to develop and test a thrust control system.

The test stand consisted of a short metal beam on a pivot, with a force transducer attached to one end, and a thruster pod attached to the other. The thruster creates a force perpendicular to the beam on one end, and the moment of force was measured by the transducer at the other end. The thruster pod consisted of a hose, with shop air that carried a constant pressure, input to a solenoid valve, and the converging-diverging nozzle attached to the output of the valve. The volume between the valve and the nozzle throat became the thrust chamber which had traducers attached to measure pressure and temperature. The lab set up can be seen in Figure 5.4. The data was collected with LabView and was analyzed using Matlab.

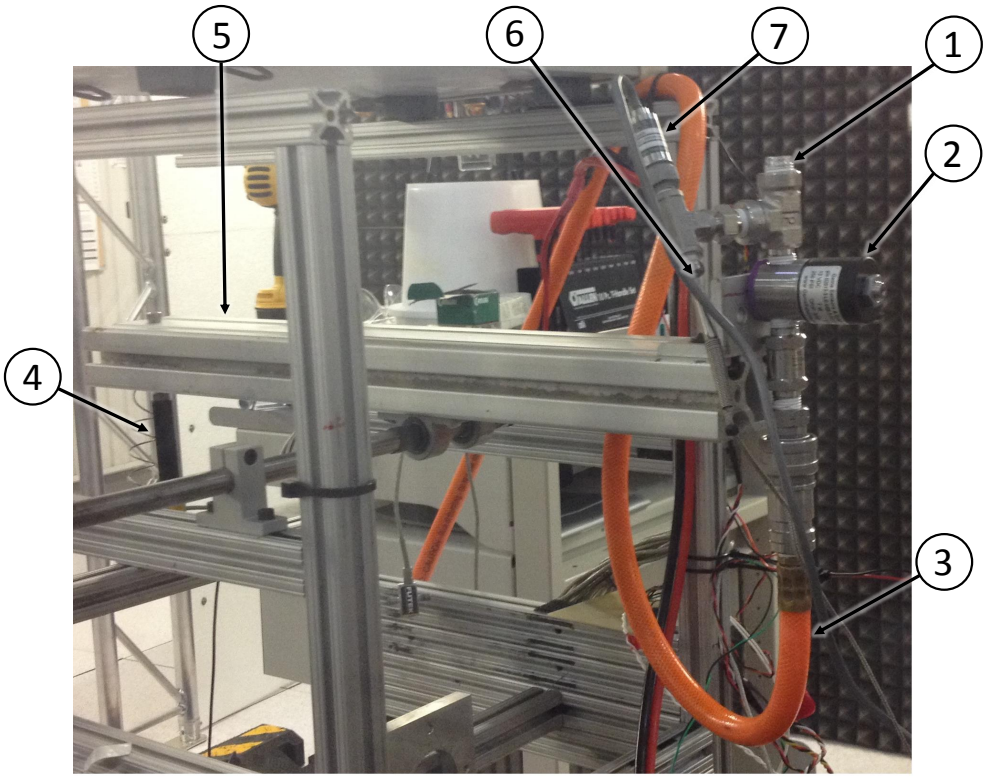

Figure 5.4: Thruster pod test stand. Nozzle (1), solenoid valve (2), shop air (3), force sensor (4), moment arm (5), temperature sensor (6), pressure sensor (7).

Thruster Performance Testing

Initial testing measured the steady state thrust force as a function of chamber pressure. The chamber pressure was varied for both the 0.05 ″ and 0.07 ″ nozzles. The resulting thrust could then be compared to the predicted thrust from the thrust equations.

As seen in Figure 5.5, the 0.05 ″ nozzle performed at approximately 96% of theoretical, while the 0.07 ″ nozzle performed at approximately 90% of theoretical. Because the 0.05 ″ nozzle performed at a higher efficiency and provided the necessary thrust, further testing was only performed on the 0.05 ″ nozzle.

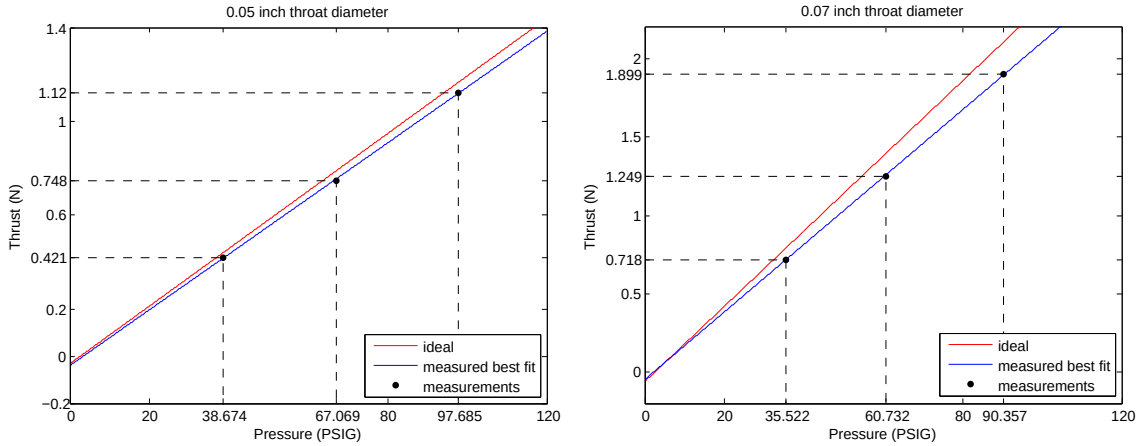

Figure 5.5: Measured steady state results showing thrust as a function of chamber pressure for the 0.05 ″ and 0.07 ″ nozzles.

Solenoid Valve Performance Testing

The thruster response times were measured by commanding the solenoid valve to open and close at various intervals. The goal is to measure the pressure response profile of an open command and a close command, including any response delay. An example trial is shown in Figure 5.6.

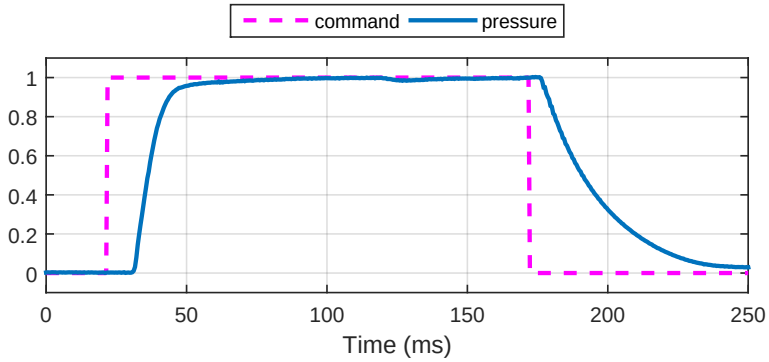

Figure 5.6: Measured chamber pressure response profile to a solenoid valve command open and close.

From Figure 5.6 the pressure response can be broken down. There is a clear delay

between the command open signal and the pressure response, which we will call open delay. There is a steep increase in pressure which slows near 100%. There is also a clear delay between the close command and the pressure response, which we will call the close delay. The pressure response is then a slower exponential decay. The pressure response was further tested by varying the time interval for open and closed commands. A sample of results is shown in Figure 5.7.

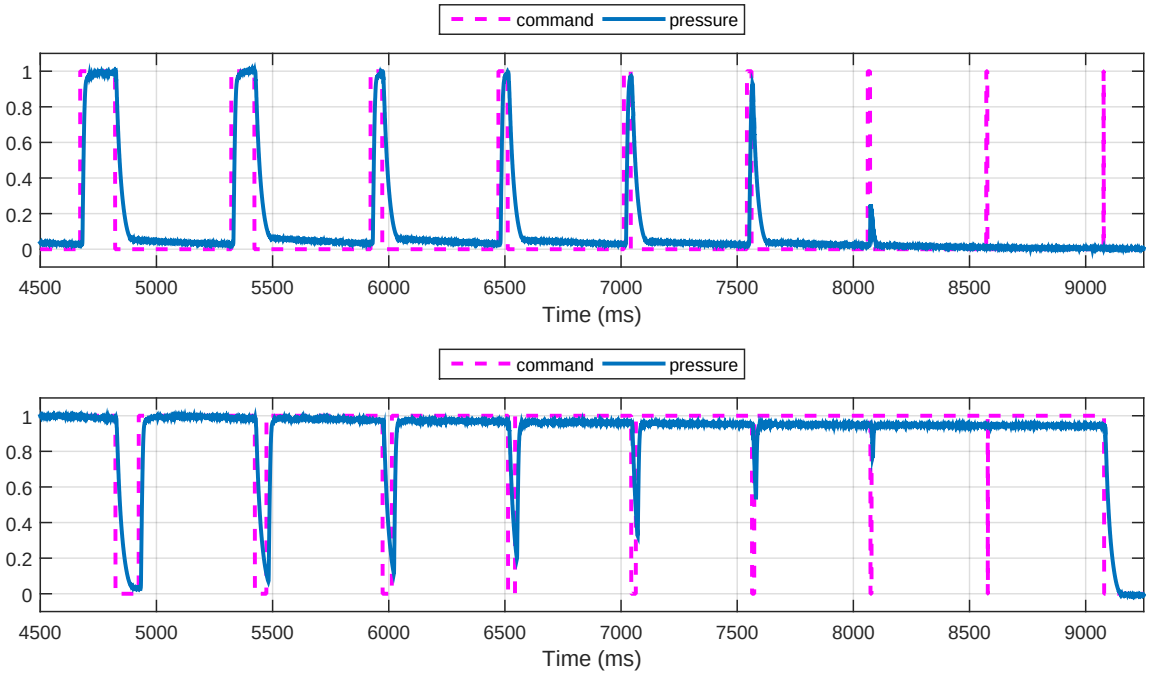

Figure 5.7: Variation in open interval time (VCO). Variation in closed interval time (VCC). Response measurement of chamber pressure resulting from variation of command input.

Figure 5.7 (top) shows that as the open time is decreased, the pressure eventually does not reach 100%, and eventually shows no response at all, giving a limit to control input responsiveness. A similar effect is shown in Figure 5.7 (bottom) for decreasing closed time. The pressure eventually cannot reach 0% and eventually

shows no response at all. These profiles will affect the average thrust over a given open/close command cycle.

The open delay was also measured as it depended on the previous closed time interval, and the close delay was measured as it depended on the previous open time interval. It was found that the solenoid valve had an open delay of approximately 10 ms and a close delay of approximately 5 ms. The delays decreased if the previous command interval was small, as shown Figure 5.8.

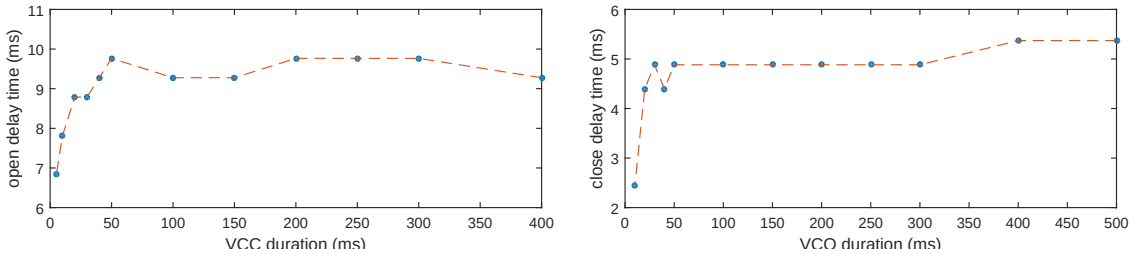

Figure 5.8: Solenoid delay as a function of how recently the solenoid was opened or closed. Variable Command Open (VCO), Variable Command Close (VCC).

Thrust Measurement Noise

It is clear from Figure 5.9 that there is a lot of noise in the thrust measurement. This damped oscillation on the thrust signal was determined to be an impulse response of the test stand itself, independent of the thruster. By filtering out the oscillation frequency, also shown in Figure 5.9, the thrust is shown to follow the pressure profile as expected. Since this measurement noise oscillated about a zero mean, it could be averaged out over a given thrust cycle.

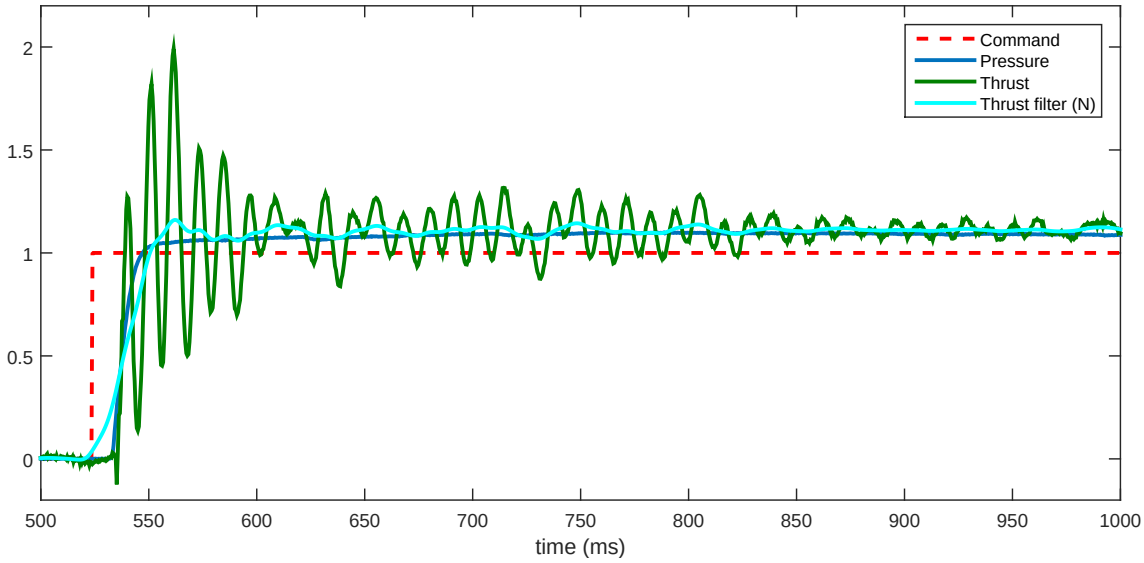

Figure 5.9: Filter to determine the actual thrust from the measurement noise.

Cold Gas Model Tuning

The parameters of the cold gas model were adjusted to match the pressure and thrust profiles from the test data. This includes physical dimensions, dimensionless coefficients, and regulator parameters. The model was tuned to match the solenoid delay and thrust performance. Figure 5.10 shows that the model was able to reproduce the measured values of the actual system.

Thrust to Duty Cycle Look-up Tables

From the updated cold gas model, the relation of duty cycle to thrust was investigated for multiple cycle frequencies to determine accuracy and range. From this, the 5 Hz and 10 Hz frequencies were chosen as the best candidates. The trade-off is that the 5 Hz frequency is most likely more accurate, but the 10 Hz frequency allows the attitude controller to react faster.

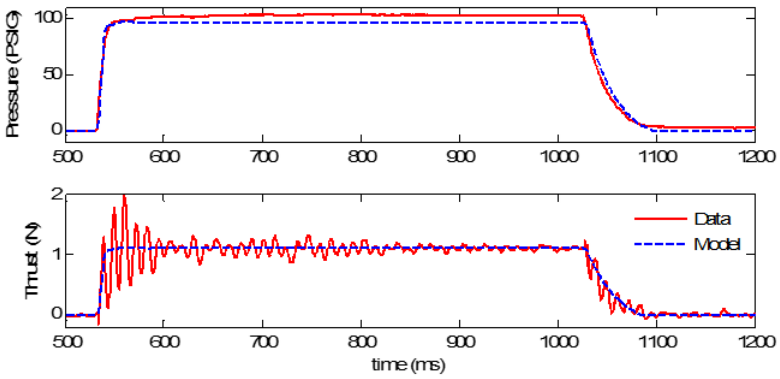

Figure 5.10: Cold gas model updated to predict pressure and thrust profile for a given command, based on test stand data.

To create the look-up table, the full Asteroid Free Flyer cold gas system was tested with a single thruster attached to the static test stand to measure thrust force.

The solenoid valve was sent several duty cycles with ten cycles each as thrust was recorded. The average thrust of each cycle was calculated in post processing as shown in Figure 5.11.

The average thrust of each duty cycle from Figure 5.11 was normalized by the maximum average thrust to create the look-up table shown in Figure 5.12.

The look-up table data was created by measuring one thruster as a total of one or four thrusters were firing. Four look-up tables were created in total; both 5 Hz and 10 Hz frequencies, each with one or four thrusters firing. The four thruster case was used in the final version as this was determined to be the most average case during attitude maneuvers. The 10 Hz case was chosen as the most desirable for its faster reactivity.

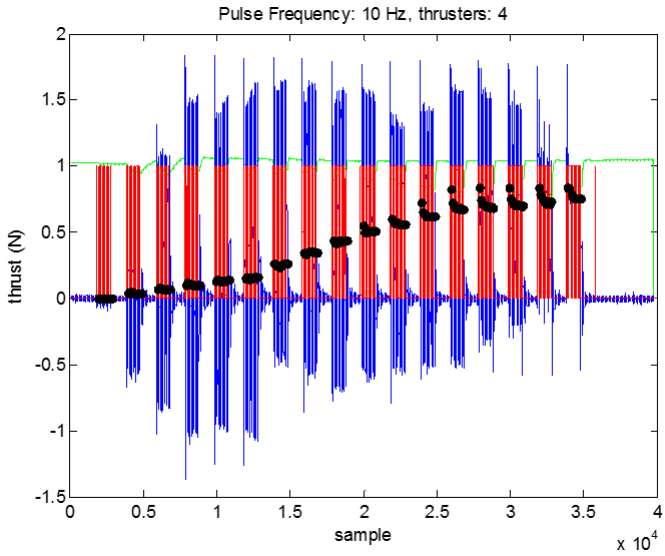

Figure 5.11: Data used to create duty cycle look-up table. The red is the command signal, the blue is thrust, the black dots are the average thrust over one cycle. Each block of black dots is the result of a different duty cycle.

5.3.2 PWM Controller for Asteroid Free Flyer

The cold gas thrust controller reads the desired thrust at the beginning of each cycle. The desired thrust is divided by the maximum thrust to convert to a percentage. The look-up table chooses the correct duty cycle that will produce the desired thrust. A PWM is then generated with that duty cycle and sent out to command the solenoid valve to open and close accordingly. The block diagram is shown in Figure 5.13.

Performance Data

The PWM controller was tested by sending a series of desired thrusts and measuring the actual thrust on the test stand. Figure 5.14 shows that the controller is providing the correct thrust up until the maximum thrust limit.

Note that in Figure 5.14 the available pressure drops as thrust demand increases,

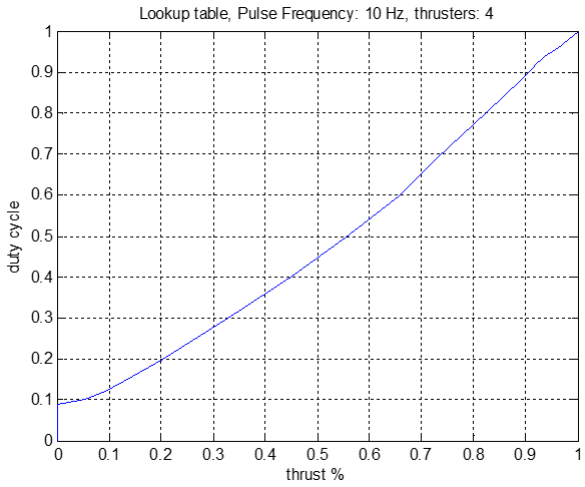

Figure 5.12: Thrust to duty cycle look-up table.

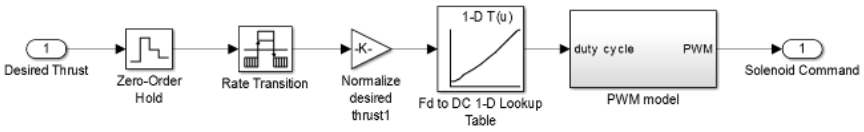

Figure 5.13: Block diagram of PWM cold gas controller.

lowering the total thrust possible. This pressure drop is more severe as more thrusters demand thrust. This can be seen in Figure 5.15 as more thrusters are fired.

As seen from the PS2 measurement of Figure 5.15, the regulator output decreases as more valves are open, and it is not able to raise the pressure to its desired setting. However the pressure reaches a steady state. Additionally, PS3 shows the solenoid feed line pressure drops even lower than PS2, which becomes more severe as more valves are open, but also remains at a steady state.

The performance of the cold gas system was also tested as tank pressure decreased over time. Figure 5.16 (top) shows a tank pressure drop from 1000 psig to 100 psig. Figure 5.16 (bottom) shows that the thrust tracked a desired thrust up to a maximum thrust limit until the tank pressure reached approximately 500 psig. As

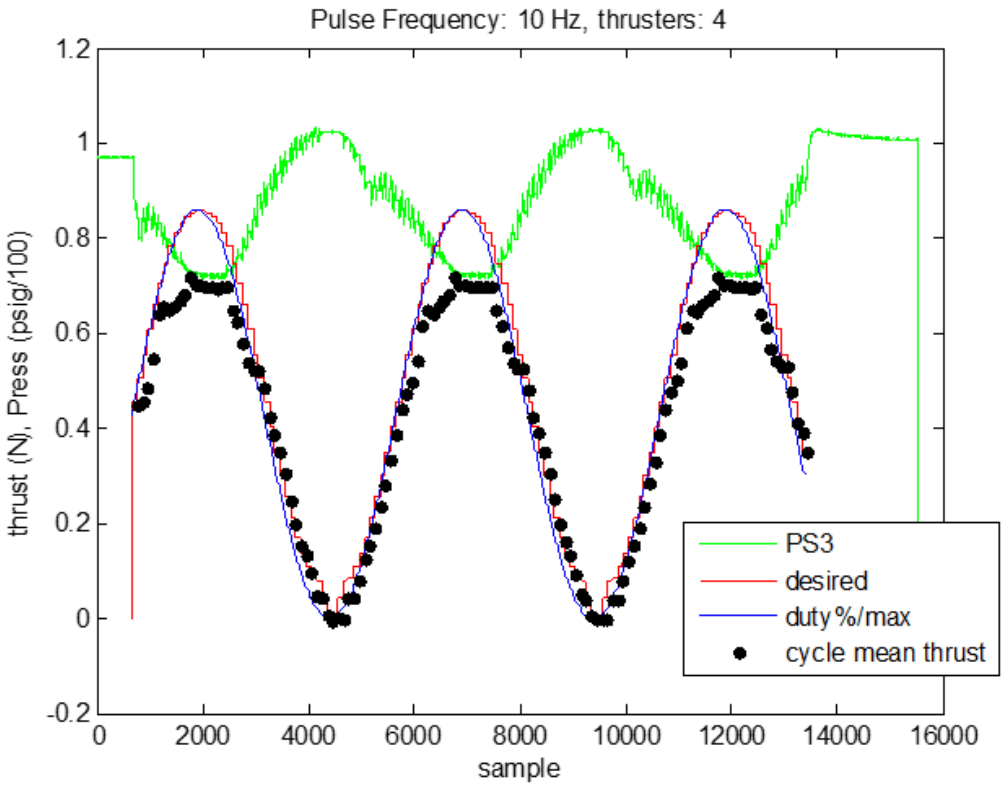

Figure 5.14: Test stand data comparing desired thrust with provided thrust from the PWM controller. PS3 is the solenoid valve input pressure. Actual thrust is able to track the desired thrust to a maximum limit.

the maximum thrust decreased, the accuracy of the PWM controller also decreases below approximately 200 psig.

5.3.3 Conclusions

The model created was able to closely predict a cold gas system. This provided information when designing the cold gas system for the Asteroid Free Flyer. The model also provided a simulation test bed to help design cold gas thrust controllers. The model was tuned based on test data to more accurately predict a particular cold

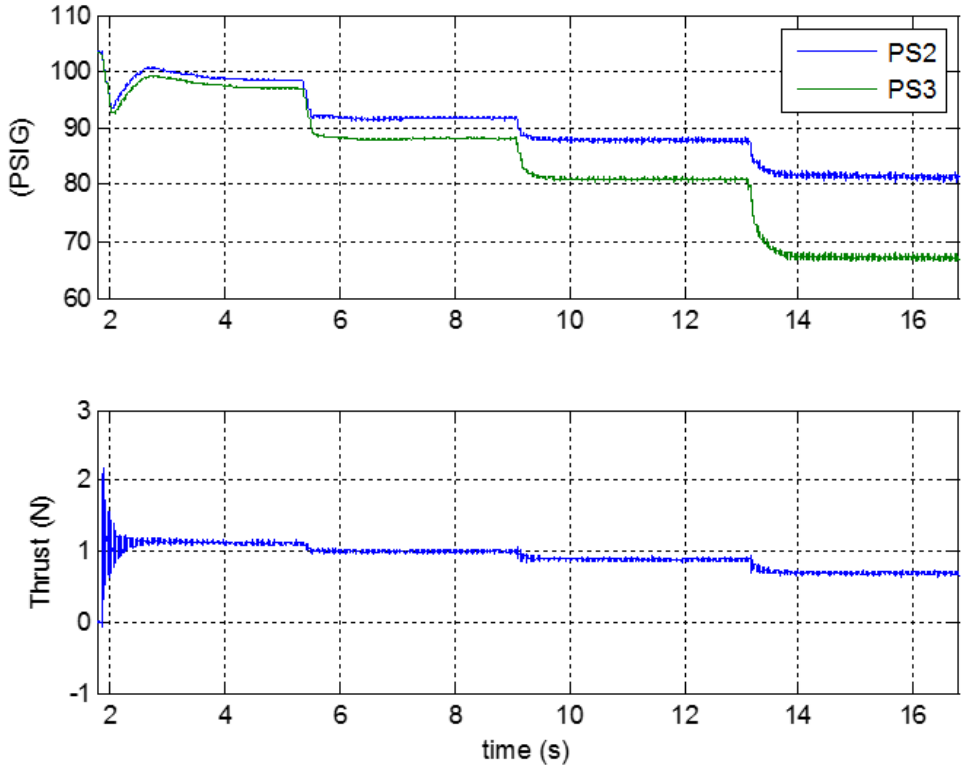

Figure 5.15: Regulator pressure is set at 103 psig and measured as 1, then 2, then 4, and then 6 thrusters are fired at once. PS2 is the regulator output pressure. PS3 is the solenoid valve input pressure.

gas system.

The PWM controller was successfully demonstrated on the thrust test stand as well as Asteroid Free Flyer attitude tests.

Although the performance of one thruster is very close to ideal, efficiency decreases significantly as many thrusters were used simultaneously during flight. Future research could be done to investigate solutions to prevent these significant pressure losses.

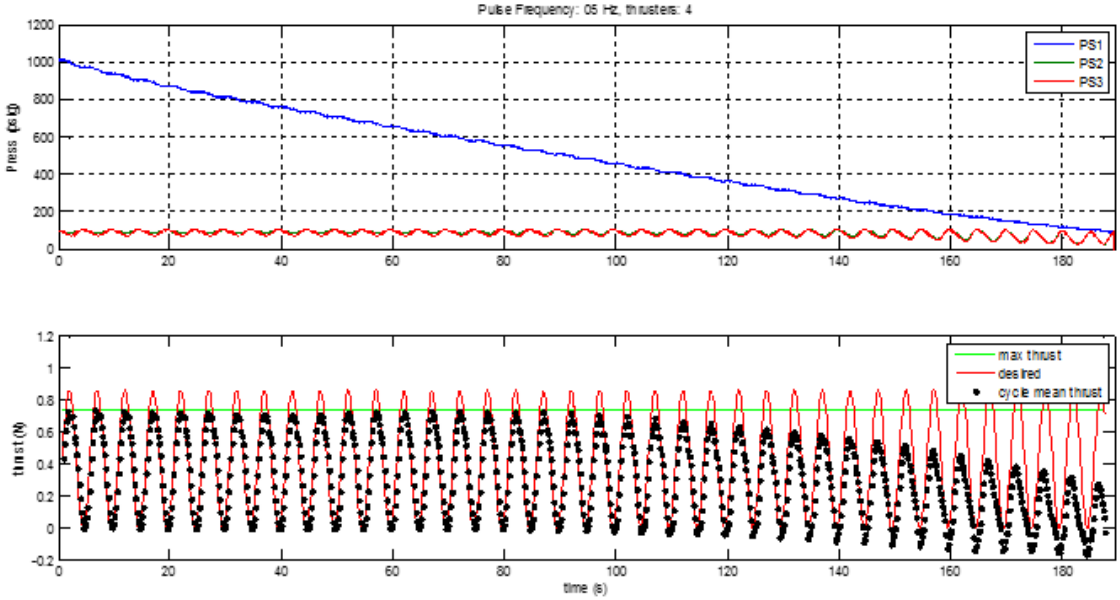

Figure 5.16: PWM controller performance as tank pressure is depleted.

Chapter 6

Feedback Thrust Control for Cold Gas Propulsion System

In this chapter, the design, modeling and control are described for a spacecraft configuration specified as that of a small surveyor to operate near a planetary surface in a gravity field, such the Moon or Mars. The spacecraft is designed to have one main gravity offloading thruster and four smaller reaction thrusters. The main thruster is actuated by a pressure regulator to provide small continuous thrust (Kitchen-McKinley et al., 2016). The four reaction thrusters are actuated by solenoid valves, which provides discrete thrust output. The control goal is to provide the desired thrust to each thruster. Two feedback controllers are incorporated, one for each of the thruster types as separate subsystems (one for the main thruster and one for a reaction thruster). An observer is also designed for the main thruster regulator to assist in full state feedback. Based on only pressure feedback states, both controllers can be implemented to track desired thrust as commanded by an upper level attitude

control system. The fluid model from Chapter 4 is used to develop the controllers and show the success of the controllers in simulation.

6.1 Full System Model

For a spacecraft in a gravitational field the cold gas propulsion system has one main thruster for gravitational off loading and four small thrusters for attitude control. The schematic for this system is shown in Figure 6.1.

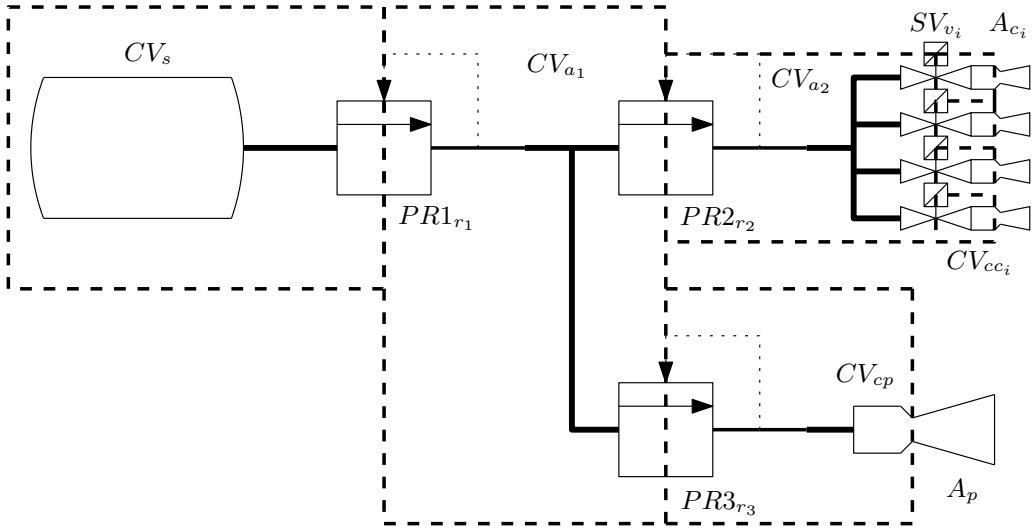

Figure 6.1: Cold gas propulsion schematic. The dot dash lines show control volumes. Each control volume and orifice is labeled and the nomenclature is given in Table 6.1.

Using (4.2),(4.3),(4.4),(4.10) and (4.18) for each component labeled in Figure 6.1,

Table 6.1: Cold gas propulsion system component subscript labels for Figure 6.1.

Control Volumes	
CV_s	source
CV_{a_1}	accumulation volume 1
CV_{a_2}	accumulation volume 2
CV_{cp}	main propulsion thruster chamber
CV_{cc_i}	reaction thruster chamber i
Orifices	
$PR1_{r_1}$	pressure regulator 1
$PR2_{r_2}$	pressure regulator 2
$PR3_{r_3}$	pressure regulator 3
A_p	main propulsion throat area
SV_{v_i}	solenoid valve i
A_{c_i}	reaction thruster throat area i

the model becomes a system of first order differential equations written as

$$\dot{P}_s = \frac{RT_s}{V_s}(-\dot{m}_{r_1}) \tag{6.1a}$$

$$\dot{m}_{r_1} = A_{r_1} P_s \sqrt{\frac{2\gamma}{RT_s(\gamma-1)}\left[\left(\frac{P_{a_1}}{P_s}\right)^{\frac{2}{\gamma}} - \left(\frac{P_{a_1}}{P_s}\right)^{\frac{\gamma+1}{\gamma}}\right]} \tag{6.1b}$$

$$\tau_{r_1}\dot{A}_{r_1} = -A_{r_1} - k_{r_1}(P_{a_1} - P_{r_1}) \tag{6.1c}$$

$$\dot{P}_{a_1} = \frac{RT_{a_1}}{V_{a_1}}(\dot{m}_{r_1} - \dot{m}_{r_2} - \dot{m}_{r_3}) \tag{6.1d}$$

$$\dot{m}_{r_2} = A_{r_2} P_{a_2} \sqrt{\frac{2\gamma}{RT_{a_2}(\gamma-1)} \left[\left(\frac{P_{a_2}}{P_{a_1}} \right)^{\frac{2}{\gamma}} - \left(\frac{P_{a_2}}{P_{a_1}} \right)^{\frac{\gamma+1}{\gamma}} \right]} \tag{6.1e}$$

$$\tau_{r_2} \dot{A}_{r_2} = -A_{r_2} - k_{r_2}(P_{a_2} - P_{r_2}) \tag{6.1f}$$

$$\dot{m}_{r_3} = A_{r_3} P_{a_1} \sqrt{\frac{2\gamma}{RT_{a_1}(\gamma-1)} \left[\left(\frac{P_{cp}}{P_{a_1}} \right)^{\frac{2}{\gamma}} - \left(\frac{P_{cp}}{P_{a_1}} \right)^{\frac{\gamma+1}{\gamma}} \right]} \tag{6.1g}$$

$$\tau_{r_3} \dot{A}_{r_3} = -A_{r_3} - k_{r_3}(P_{cp} - u_p) \tag{6.1h}$$

$$\dot{P}_{cp} = \frac{RT_{cp}}{V_{cp}} (\dot{m}_{r_3} - \dot{m}_p) \tag{6.1i}$$

$$\dot{m}_p = A_p P_{cp} \sqrt{\frac{\gamma}{RT_{cp}} \left(\frac{2}{\gamma+1} \right)^{\frac{\gamma+1}{\gamma-1}}} \tag{6.1j}$$

$$\dot{P}_{a_2} = \frac{RT_{a_2}}{V_{a_2}} (\dot{m}_{r_2} - \sum_{i=1}^{4} \dot{m}_{v_i}) \tag{6.1k}$$

$$\dot{m}_{v_i} = A_{v_i} P_{a_2} \sqrt{\frac{2\gamma}{RT_{a_2}(\gamma-1)} \left[\left(\frac{P_{cc_i}}{P_{a_2}} \right)^{\frac{2}{\gamma}} - \left(\frac{P_{cc_i}}{P_{a_2}} \right)^{\frac{\gamma+1}{\gamma}} \right]} u_i \tag{6.1l}$$

$$\dot{P}_{cc_i} = \frac{RT_{cc_i}}{V_{cc_i}} (\dot{m}_{v_i} - \dot{m}_{c_i}) \tag{6.1m}$$

$$\dot{m}_{c_i} = A_{c_i} P_{cc_i} \sqrt{\frac{\gamma}{RT_{cc_i}} \left(\frac{2}{\gamma+1} \right)^{\frac{\gamma+1}{\gamma-1}}} \tag{6.1n}$$

where u_i is the solenoid control input for the reaction thrusters, and u_p is the control input for the main propulsion regulator setting, for $i = 1, \ldots, 4$ for each reaction thruster.

6.2 Control

The control input for the reaction thrusters is the cross section area A, in the mass flow equation for each solenoid valve, where the area is commanded as either zero area

or maximum area (closed or open). The control input for the main thruster the set point for the adjustable pressure regulator P_{r_3}. This allows for continuous control of the main propulsion as opposed to the discontinuous control of the reaction thrusters. The control goal is to provide the desired thrust as commanded by the higher level flight controller. By substituting (4.6)-(4.10) into (4.11), the thrust force model can be written in the form

$$F = C_1 P_c + C_2 \tag{6.2}$$

where C_1 and C_2 are

$$C_1 = A_t M_e \gamma \left(\frac{2}{\gamma+1}\right)^{\frac{\gamma+1}{2(\gamma-1)}} \left(1+\frac{\gamma-1}{2}M_e^2\right)^{-\frac{1}{2}} + A_e \left(1+\frac{\gamma-1}{2}M_e^2\right)^{-\frac{\gamma}{\gamma-1}} \tag{6.3}$$

$$C_2 = A_e P_a \ . \tag{6.4}$$

Based on the assumption that the gas type, nozzle geometry, and atmospheric pressure, are constant, thrust force is a linear function of chamber pressure as seen in (6.2). The relation in (6.2) is used to calculate a desired chamber pressure from the desired force for each thruster. The state space model, of the form $\dot{x} = f(x,u)$, in this case is made up of the states

$$x = [P_s \ P_{a_1} \ P_{a_2} \ P_{cc_1} \ P_{cc_2} \ P_{cc_3} \ P_{cc_4} \ P_{cp} \ A_{r_1} \ A_{r_2} \ A_{r_3}]^T \ . \tag{6.5}$$

The thrust controllers are designed as full state feedback. It is reasonable to assume that the pressure states can be directly measured at each location. However, measuring the orifice area of each regulator would be very difficult. An observer is designed to estimate the value of the area states. The feedback controller is developed for the

main propulsion system independently from the reaction control system.

6.2.1 Main Propulsion Control

The actuator for the main propulsion thrust is the set pressure of the upstream pressure regulator ($PR3$). The local subsystem model for the main propulsion can be written as

$$\begin{aligned}\dot{P}_{cp} = &\left(\frac{RT_{cp}}{V_{cp}}P_{a_1}\sqrt{\frac{2\gamma}{RT_{a_1}(\gamma-1)}\left[\left(\frac{P_{cp}}{P_{a_1}}\right)^{\frac{2}{\gamma}}-\left(\frac{P_{cp}}{P_{a_1}}\right)^{\frac{\gamma+1}{\gamma}}\right]}\right)A_{r_3} \\ &-\left(\frac{RT_{cp}}{V_{cp}}A_p\sqrt{\frac{\gamma}{RT_{cp}}\left(\frac{2}{\gamma+1}\right)^{\frac{\gamma+1}{\gamma-1}}}\right)P_{cp}\end{aligned} \tag{6.6a}$$

$$\dot{A}_{r_3} = -\frac{1}{\tau_{r_3}}A_{r_3} - \frac{k_{r_3}}{\tau_{r_3}}P_{cp} + \frac{k_{r_3}}{\tau_{r_3}}u_p\ . \tag{6.6b}$$

To simplify the state equation, we introduce the notation

$$b(P_{cp}) = \left(\frac{RT_{cp}}{V_{cp}}P_{a_1}\sqrt{\frac{2\gamma}{RT_{a_1}(\gamma-1)}\left[\left(\frac{P_{cp}}{P_{a_1}}\right)^{\frac{2}{\gamma}}-\left(\frac{P_{cp}}{P_{a_1}}\right)^{\frac{\gamma+1}{\gamma}}\right]}\right) \tag{6.7a}$$

$$k = \left(\frac{RT_{cp}}{V_{cp}}A_p\sqrt{\frac{\gamma}{RT_{cp}}\left(\frac{2}{\gamma+1}\right)^{\frac{\gamma+1}{\gamma-1}}}\right)\ . \tag{6.7b}$$

The controller is based on the error $\bar{P}_{cp} = P_{cp} - P^*_{cp}$ where P^*_{cp} is the desired pressure. Assuming $\dot{P}^*_{cp} = 0$, the error dynamics can be derived as

$$\dot{\bar{P}}_{cp} = bA_{r_3} - kP_{cp}\ . \tag{6.8}$$

Driving this system to zero is guaranteed if $A_{r_3} = \frac{k}{b} P_{cp} - k_p \bar{P}_{cp}$ as the error dynamics become $\dot{\bar{P}}_{cp} = -k_p P_{cp}$. We propose the sliding surface to be

$$\sigma = bA_{r_3} - kP_{cp} - bk_p \bar{P}_{cp} = 0 \; . \tag{6.9}$$

To drive the system to the sliding surface the control input can be defined as

$$u_p = M_p \left[\frac{(u_{\max} - u_{\min})}{2} \text{sat} \left(\frac{1}{\epsilon_p} \left[\sigma + \lambda_p \int_0^t \sigma(\tau) d\tau \right] \right) + \frac{(u_{\max} - u_{\min})}{2} + u_{\min} \right] \tag{6.10}$$

where k_p, M_p, $u_{p\max}$, $u_{p\min}$, ϵ_p, and λ_p are tunable control parameters and $\text{sat}(\cdot)$ is the saturation function. This control function is designed so that the regulator set pressure switches fast between a higher or lower pressure than the desired pressure depending on a required increase or decrease in downstream pressure. This sliding mode controller has a performance improvement over directly setting the regulator set pressure to the desired pressure as long as the set pressure can be changed faster than the regulator dynamics. The convergence speed, however, is still limited to maximum regulator dynamics. The control law (6.10) as a function of the sliding surface is shown in Figure 6.2.

In this case the sliding surface, $\sigma + \lambda_p \int \sigma$, contains an integral term to remove any bias error. By taking the time derivative of (6.9), the dynamics of the sliding surface can put in the form

$$\dot{\sigma} = \psi_1 \text{sat} \left(\frac{1}{\epsilon_p} \left[\sigma + \lambda_p \int_0^t \sigma(\tau) d\tau \right] \right) + \psi_2 \tag{6.11}$$

where $|\psi_1|$ and $|\psi_2|$ are variables that depend on system state and tuning parameters.

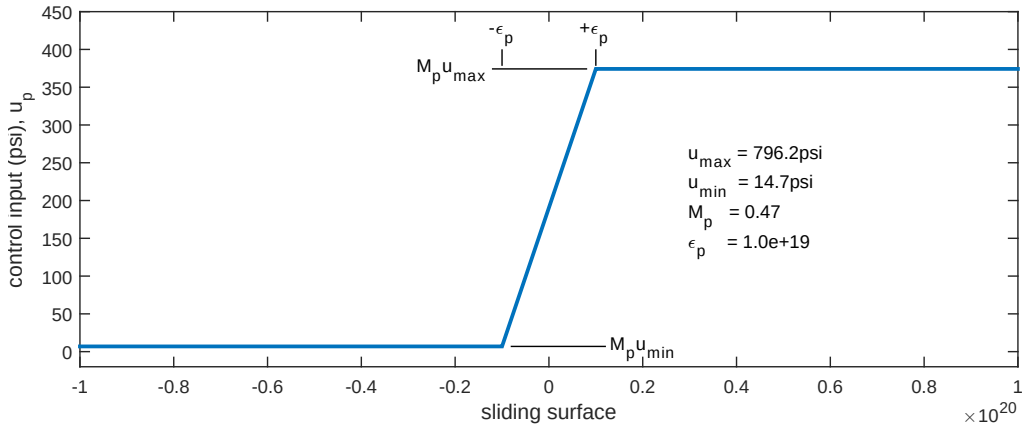

Figure 6.2: Control law (6.10) as a function of the sliding surface with example tuning parameters.

Equation (6.11) shows sliding mode control is guaranteed if $\sigma\dot{\sigma} < 0$. This can be achieved if control parameters k_p, M_p, $u_{\max}$, and $u_{\min}$ are tuned such that $|\psi_1| > |\psi_2|$.

Simulation

For simulating the main thruster performance, the desired thrusts of the reaction thrusters are set to zero. The desired thrust, for the main thruster, is given two step changes to visually demonstrate the tracking and control capabilities of the controller.

For comparison, the model is run using only the regulator dynamics. That is, the desired pressure for the main thruster is fed back directly as the set pressure into the upstream regulator.

The sliding mode controller developed in the previous section attempts to improve convergence robustness and accuracy of the desired thrust by rapidly adjusting the set pressure. The ability to tune the controller gains also allows for the convergence profile to be adjusted. The controller performance is shown in Figure 6.3a with two different gain values compared to no controller. The controller response is shown

against a step change in desired thrust to clearly show the convergence profile. Some

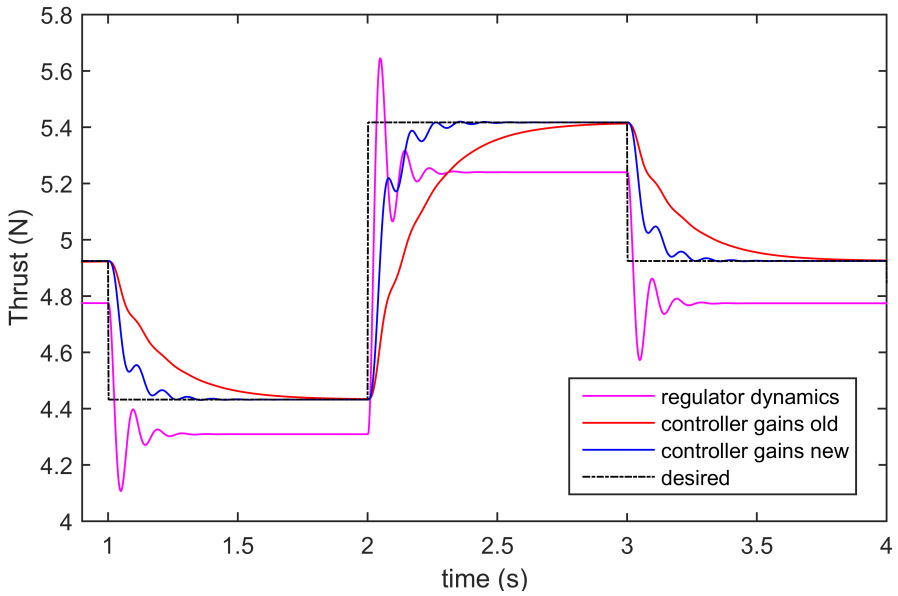

(a) Main propulsion performance using sliding mode controller with two different gain values compared to no controller.

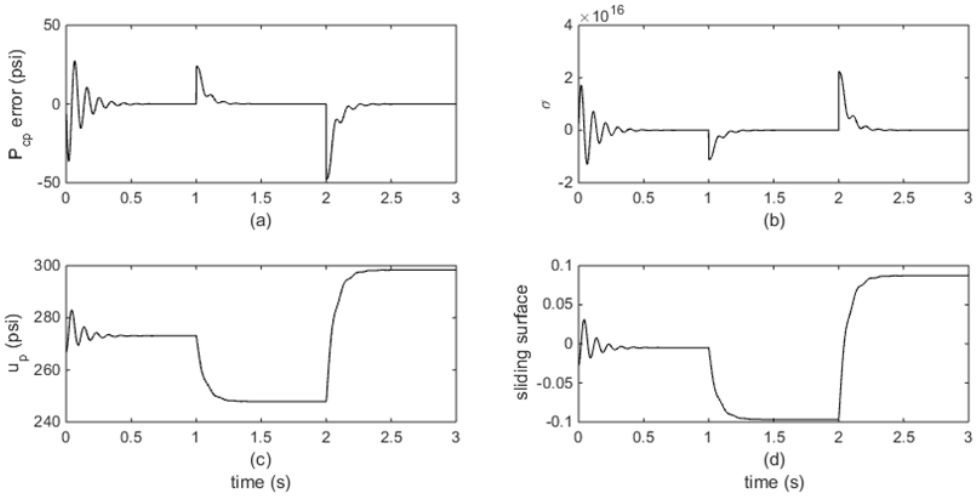

(b) Sliding mode control input states.

Figure 6.3: Controller response to desired thrust step change.

relevant controller states such as the error, $\bar{P}_{cp}$, the sliding surface, σ, and the control

input, u_p, are shown in Figure 6.3b. The desired thrust will mostly likely be a slowly changing value, so the controller's tracking performance is shown in Figure 6.4. The sliding mode controller is able to track the desired thrust much closer than only using the regulator dynamics. The ability to tune the controller gains allows for the tracking accuracy to be adjusted.

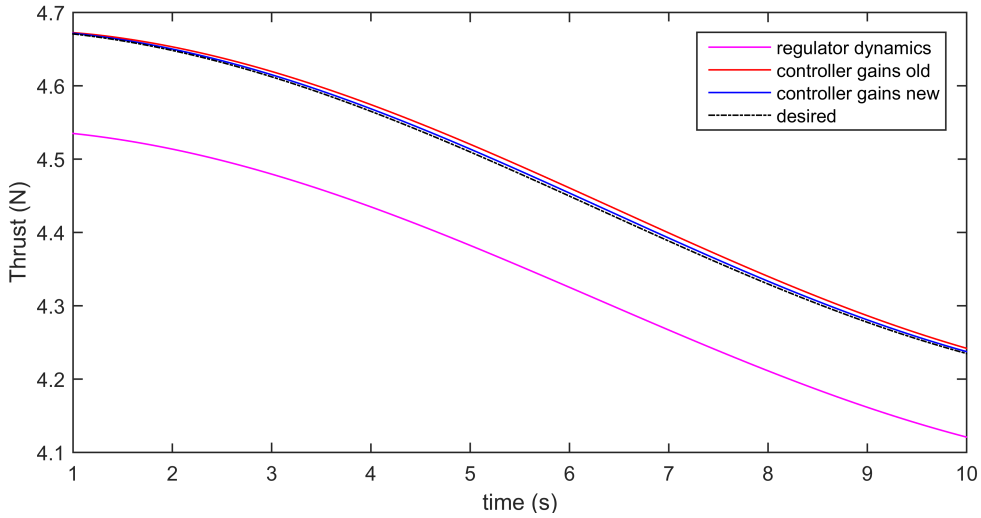

Figure 6.4: Main propulsion tracking performance using sliding mode controller with two different gain values compared to no controller.

6.2.2 Regulator Observer

The sliding mode controller requires measurements of the cold gas system states, upstream pressure P_{a_1}, downstream pressure P_{cp}, and the regulator orifice area A_{r_3}. It is practical to assume that the pressures can be measured directly. However, it would be nearly impossible to directly measure the orifice area. Even if the mechanical states of the regulator could be measured, it would be difficult to determine the effective area that ultimately determines the mass flow as described in the fluid model. It is

more desirable to estimate the orifice area that is mathematically modeled in the dynamic equations. A sliding mode observer is developed in this section to estimate the regulator orifice area based on the upstream and downstream pressure measurements.

The main propulsion state subsystem (6.6) is rewritten as

$$\dot{P}_{cp} = \frac{RT_{cp}}{V_{cp}} \left[A_{r_3} f_{r_3}(P_{cp}, P_{a_1}) - f_p(P_{cp}) \right] \tag{6.12a}$$

$$\dot{A}_{r_3} = -\frac{1}{\tau_{r_3}} A_{r_3} - \frac{k_{r_3}}{\tau_{r_3}} (P_{cp} - P_a - u_p) \tag{6.12b}$$

where the functions f_{r_3} and f_p are defined as

$$f_{r_3} = P_{a_1} \sqrt{\frac{2\gamma}{RT_{a_1}(\gamma - 1)} \left[\left(\frac{P_{cp}}{P_{a_1}} \right)^{\frac{2}{\gamma}} - \left(\frac{P_{cp}}{P_{a_1}} \right)^{\frac{\gamma+1}{\gamma}} \right]} \tag{6.13}$$

$$f_p = A_p P_{cp} \sqrt{\frac{\gamma}{RT_{cp}} \left(\frac{2}{\gamma + 1} \right)^{\frac{\gamma+1}{\gamma-1}}} \, . \tag{6.14}$$

The sliding mode observer is derived to drive the estimated area $\hat{A}_{r_3}$, to the actual area A_{r_3}, based on the error of the measured downstream pressure P_{cp}, and the estimated downstream pressure $\hat{P}_{cp}$. From (6.12) the observer model is

$$\dot{\hat{P}}_{cp} = \frac{RT_{cp}}{V_{cp}} \left[\hat{A}_{r_3} f_{r_3}(P_{cp}, P_{a_1}) - f_p(P_{cp}) \right] + L_1 \text{sgn}(P_{cp} - \hat{P}_{cp}) \tag{6.15a}$$

$$\dot{\hat{A}}_{r_3} = -\frac{1}{\tau_{r_3}} \hat{A}_{r_3} - \frac{k_{r_3}}{\tau_{r_3}} (P_{cp} - P_a - u_p) + L_2 \text{sgn}(P_{cp} - \hat{P}_{cp}) \tag{6.15b}$$

where L_1 and L_2 are the observer gains.

Simulation

First, the observer gains are tuned to make sure estimated downstream pressure is correctly driven to the measured downstream stream. Then, the observer is tested on the simulated orifice area. Two sets of observer gains are tested. The gains are tuned so that the pressure converges almost immediately as shown in Figure 6.5a, and the area convergences soon after as shown in Figure 6.5b. Since area has some convergence time, it may be necessary to allow the observer to run before engaging the controller as the controller needs the orifice area feedback.

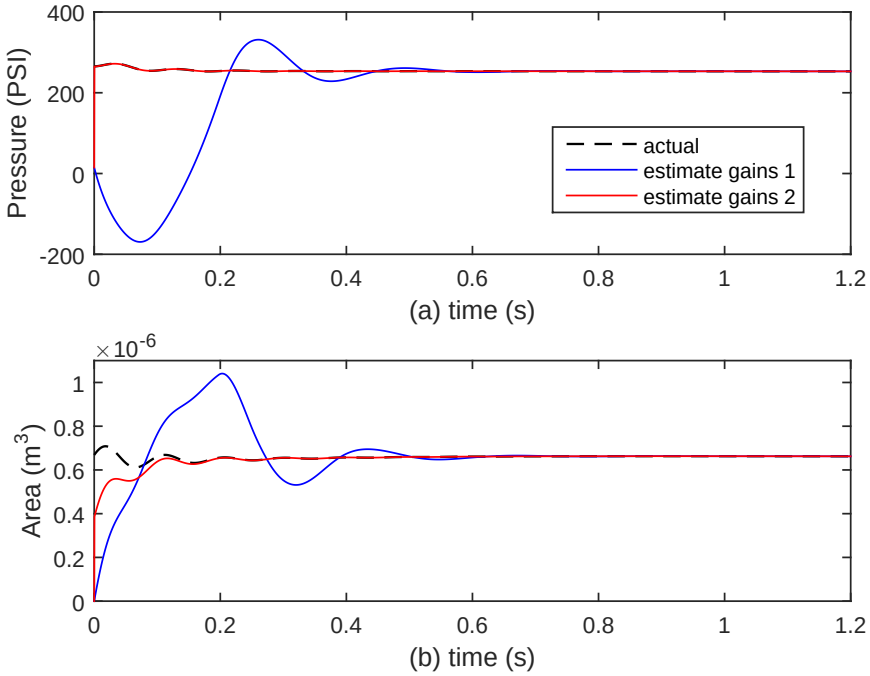

Figure 6.5: The main propulsion chamber pressure downstream of the regulator 3 orifice area. Two sets of observer gains shown. Pressure is measured while area is accurately estimated.

Next the observer is placed in the controller loop so that the observer estimate of orifice area is used as a measured feedback state for the controller. It turns out that

the controller can be engaged immediately. The controller is robust against the initial observer error before convergence. A step change and slow change in desired thrust are used to demonstrate the convergence profile and the tracking control. Once the observer converges, the area is accurately estimated, even with fast changes in area as shown in Figure 6.6a. This allows the controller to converge and track the to the desired thrust as shown in Figure 6.6b. Using the observer (6.15), the controller (6.9)

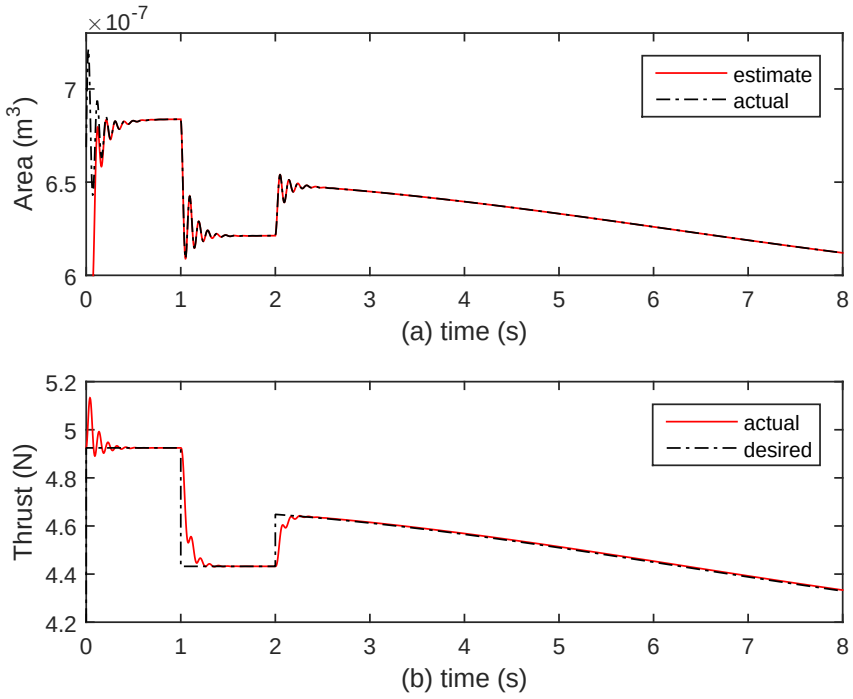

Figure 6.6: Observer estimates regulator 3 orifice area (a) as a state feedback for main propulsion thrust controller (b).

and (6.10) shows the ability to track a desired thrust based only on the feedback of pressure measurement states.

6.2.3 Reaction Thruster Control

It is expected that a fast on/off switching of the reaction thrusters is useful for making quick attitude corrections. Solenoid valves are commercially available in a variety of mass and pressure ranges and require relatively low amounts power to operate. Because of the fast switching between on and off states of the solenoid valves, developing a sliding mode controller is suitable in addition to being nonlinear and robust.

Since the input pressure is likely constant, the controller switches states fast to average a desired thrust, allowing for virtual throttling. The control goal is to drive the thrust F, to a desired thrust F^*. The desired thrust may be time varying and is provided by an upper level control system. The feedback controller is developed from the tracking error of the thrust. The tracking error is described as

$$\bar{F} = F - F^* \tag{6.16}$$

so that goal is to drive $\bar{F}$ to zero and hold it there. A sliding mode controller is designed with a dynamical sliding surface (DeCarlo, Zak, & Drakunov, 2010). The switching function is chosen as

$$\sigma = \bar{F} + \lambda \int_0^t \bar{F}(\tau) d\tau = C \tag{6.17}$$

where C is a constant, such that the time derivative with a positive gain, $\lambda > 0$, naturally drives the error to zero as

$$\dot{\bar{F}} = -\lambda \bar{F} \tag{6.18}$$

The switching surface becomes a sliding surface when $\sigma = \bar{F} + \lambda \int_0^t \bar{F}(\tau)d\tau = C$ and can be implemented in the sliding mode control as

$$u = u_0 - u_1 \text{sat}(\sigma) \tag{6.19}$$

where u is the valve area control input, u_0 is the equivalent control bias, and u_1 is a positive control gain. The equivalent control bias is calculated from the condition $\dot{\sigma} = 0$, which makes $\sigma = const$ an integral manifold (invariant set) and the term with u_1 makes it a stable attractor (S. V. Drakunov, 1993). In this case $u_0 \equiv u_1 \equiv \frac{u_{\max}}{2}$ based on the limited available area so that $0 < u < u_{\max}$.

Since the thrust of an individual thruster is difficult to directly measure, the actual thrust can be calculated by measuring the chamber pressure and using (6.2).

Simulation

The reaction thruster sliding mode control is tested in simulation for different desired thrust profiles. The simulation includes the actuator dynamics of the solenoid valve with open and close lag. This is seen in Figure 6.7, where the valve area begins to rise and fall slightly after it has been commanded. The pressure profile is also shown where the pressure begins to fall from maximum while the valve is closed. It does not fall to minimum as the valve is opened again. This produces an average pressure which is less than the maximum over time. The goal of the controller is to drive that average to the desired value. The results of the controller are shown in Figures 6.8, 6.9, and 6.10. Although it can be seen that the thrust rapidly cycles, a moving average shows the average thrust over a small finite time matches the desired thrust at any given

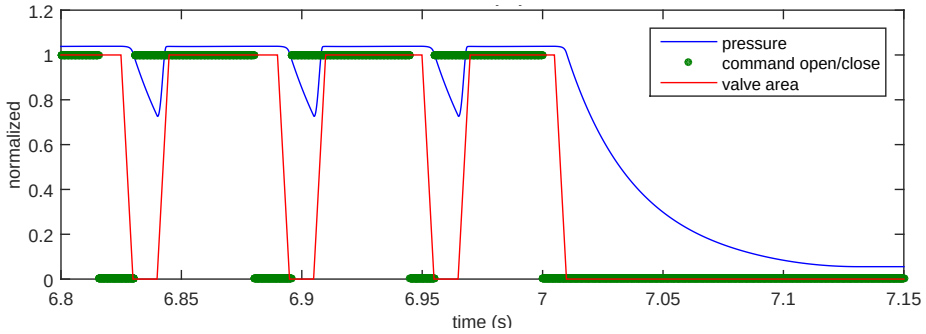

Figure 6.7: Sliding mode control virtual throttle cycle with solenoid response delay.

time. Figure 6.8 shows the thruster behavior to a constant desired thrust. Figure 6.9 shows the thruster behavior to step changes in the desired thrust. Figure 6.10 shows the thruster behavior to a variable desired thrust. It can also been seen from these figures that the controller commands a closed valve when the desired thrust is zero, and a full open valve when the desired thrust is greater than the maximum thrust.

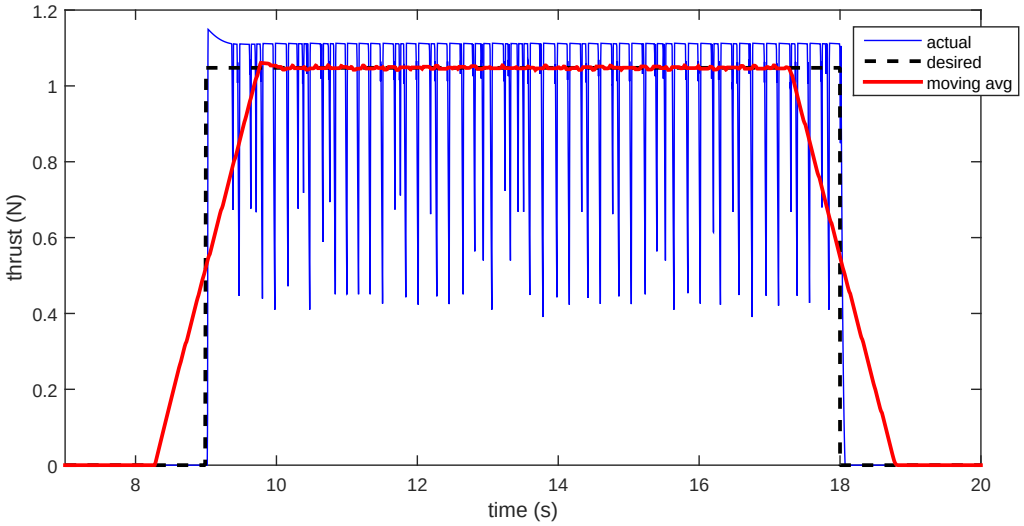

Figure 6.8: Sliding mode control virtual throttle for a constant desired thrust.

In each case, it is shown in simulation that the sliding mode controller can drive the average thrust of the reaction control thruster to a desired thrust, even with the valve

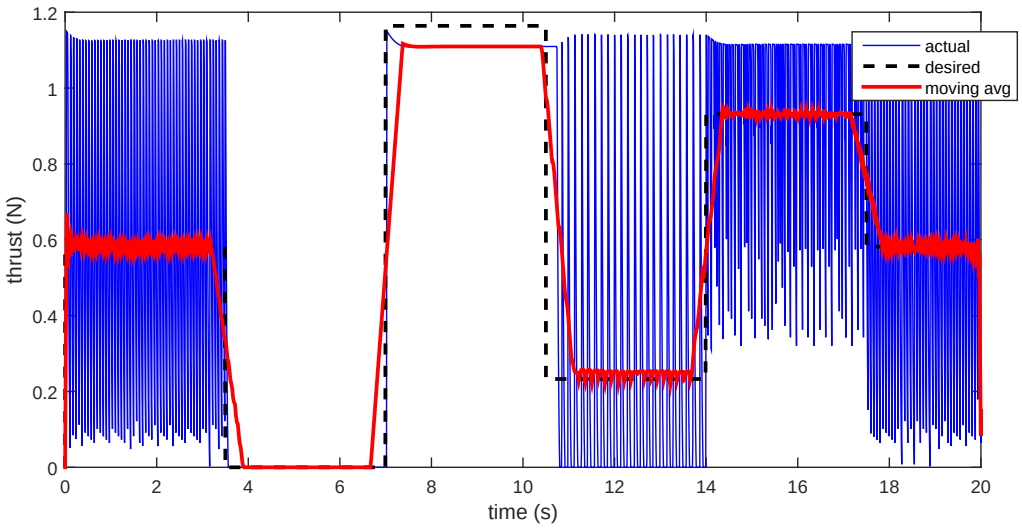

Figure 6.9: Sliding mode control virtual throttle for a variable desired thrust with step changes.

delay and the discrete input nature of the control valve. Therefore, it is possible to create a virtual throttle range between zero and maximum thrust.

6.2.4 Full Simulation

A final simulation of the full fluid model with both controllers is run to show simultaneous thrust tracking and control of all five thrusters. That is, four reaction thrusters and one main thruster. The results are shown in Figure 6.11.

6.3 Conclusion and Future Work

Two sliding mode controllers are developed to provide continuous tracking of the desired thrusts commanded by an upper level attitude control system. The added observer means that only the pressures in the system need to be measured to provide

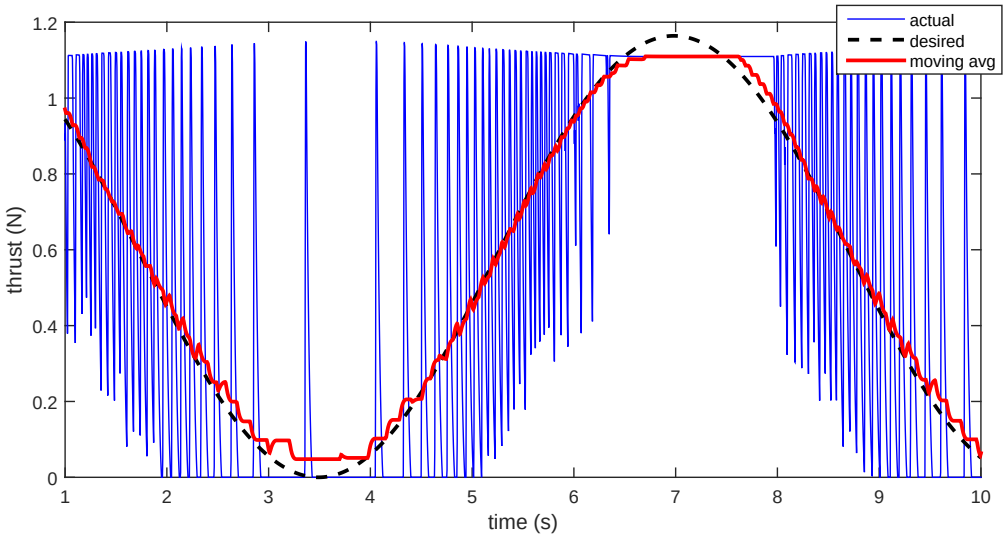

Figure 6.10: Sliding mode control virtual throttle for a variable desired thrust.

full state feedback. Simulations show the main thrust controller successfully converging to multiple desired thrusts. The sliding mode controller is also shown to remove the steady states bias and over shooting of the regulator's natural response to a new desired thrust. Simulations also show that the sliding mode controller can drive the average thrust of the reaction control thruster to a desired thrust, even with the valve delay and the discrete input nature of the control valve.

Future work would include updating the fluid model to include variation in fluid temperature and smaller atmospheric pressures to be better approximations for conditions in the space environment. The cold gas propulsion system could also be updated to include other types of flow controllers, in place of regulators and solenoid valves. The propulsion system could also improve fuel efficiency by adding heaters to increase the fluid temperatures. The pressure source could store propellant in multi-phase states, such as solid or liquid, as well as gas. Steam is an example of multi-phase storage and heated gas to improve fuel efficiency. Simulations show that

maximum available thrust at each controller can be diminished as more total thrust is output by all the thrusters. This is seen in Figure 6.10 when the desired thrust is to high the maximum thrust achieved with one thruster is approximately 1.1 N. However thruster 1 and 3 in Figure 6.11 only achieve 1 N when all thrusters are firing. This could be addressed by designing one controller for the entire system instead of designing separate controllers for the main thruster and the reaction thrusters. One controller for the entire system could possibly improve fuel efficiency with more upstream control inputs.

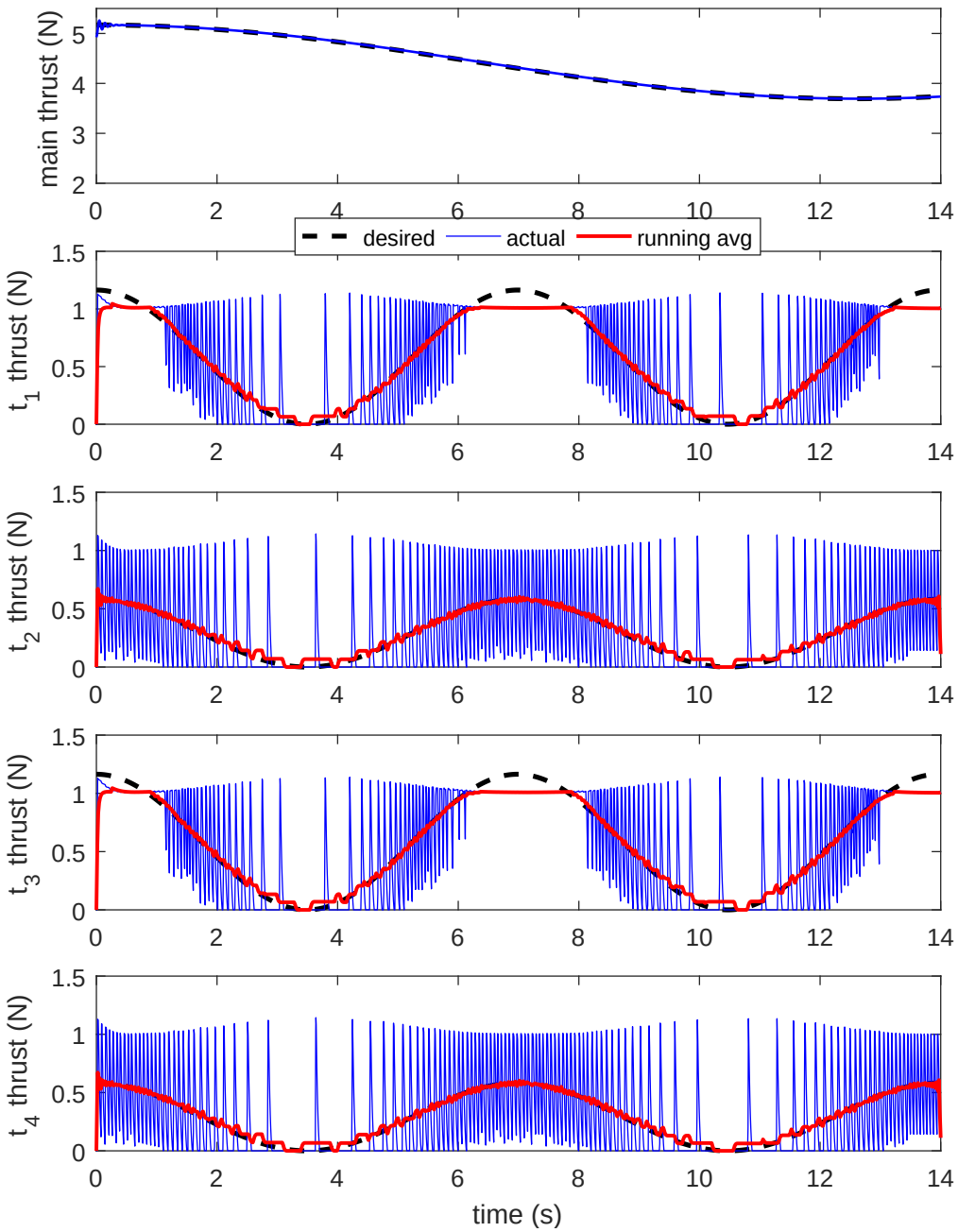

Figure 6.11: Thrust tracking and control of all five thrusters. One main thruster, and four reaction thrusters.

Chapter 7

Time Optimal Feedback Control for Spacecraft with Cold Gas Propulsion

For small spacecraft, the cold gas system may be limited to only on-off control of the main tank where the generated thrust is directly dependent on the tank pressure. As such, the thrust will slowly decrease as the propellant is expended. In this chapter a feedback control method is developed for such a spacecraft where the thrust force is directly dependent on the remaining fuel. The control law is time optimal accounting for fuel constraints and control input actuator constraints.

7.1 Full System Model

For a spacecraft in a low gravity environment the cold gas propulsion system has two main thrusters to provide thrust in each direction for translational motion in each

dimension. Two configurations are presented for comparison. A propulsion system which provides constant thrust, and a less complex propulsion system which directly feeds the tank pressure to produce thrust. The controller is designed for the direct feed case.

7.1.1 Constant Thrust

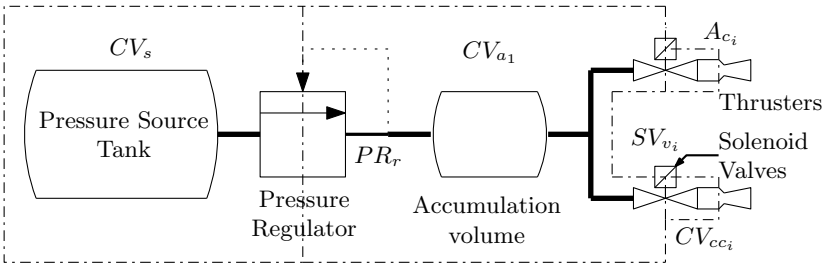

Figure 7.1: Constant thrust cold gas propulsion schematic. The dot dash lines show control volumes. Each control volume and orifice is labeled and the nomenclature is given in Table 7.1.

For one-dimensional motion the schematic for a constant thrust system is shown in Figure 7.1. The pressure regulator allows a preset constant downstream pressure, and the solenoid valve allows for two states, zero or maximum thrust.

Table 7.1: Component subscript labels for Figure 7.1 and Figure 7.2.

Control Volumes	
CV_s	source
CV_{a_1}	accumulation volume 1
CV_{cc_i}	thruster chamber $i = 1, 2$
Orifices	
PR_r	pressure regulator 1
SV_{v_i}	solenoid valve $i = 1, 2$
A_{c_i}	thruster throat area $i = 1, 2$

Using (4.2),(4.3),(4.4),(4.18) and (4.10) for each component labeled in Figure 7.1,

the model becomes a nonlinear system of first order differential equations given by,

$$\dot{P}_s = \frac{RT_s}{V_s}(-\dot{m}_r) \tag{7.1a}$$

$$\dot{m}_r = \frac{A_r P_s}{(\gamma-1)^{\frac{1}{2}}}\sqrt{\frac{2\gamma}{RT_s}\left[\left(\frac{P_{a_1}}{P_s}\right)^{\frac{2}{\gamma}} - \left(\frac{P_{a_1}}{P_s}\right)^{\frac{\gamma+1}{\gamma}}\right]} \tag{7.1b}$$

$$\tau_r \dot{A}_r = -A_r - k_r(P_{a_1} - P_r) \tag{7.1c}$$

$$\dot{P}_{a_1} = \frac{RT_{a_1}}{V_{a_1}}(\dot{m}_r - \sum_{i=1}^{2}\dot{m}_{v_i}) \tag{7.1d}$$

$$\dot{m}_{v_i} = \frac{u_i A_{v_i} P_{a_1}}{(\gamma-1)^{\frac{1}{2}}}\sqrt{\frac{2\gamma}{RT_{a_1}}\left[\left(\frac{P_{cc_i}}{P_{a_1}}\right)^{\frac{2}{\gamma}} - \left(\frac{P_{cc_i}}{P_{a_1}}\right)^{\frac{\gamma+1}{\gamma}}\right]} \tag{7.1e}$$

$$\dot{P}_{cc_i} = \frac{RT_{cc_i}}{V_{cc_i}}(\dot{m}_{v_i} - \dot{m}_{c_i}) \tag{7.1f}$$

$$\dot{m}_{c_i} = A_{c_i} P_{cc_i}\sqrt{\frac{\gamma}{RT_{cc_i}}\left(\frac{2}{\gamma+1}\right)^{\frac{\gamma+1}{\gamma-1}}} \tag{7.1g}$$

where u_i is the solenoid control input for the thrusters. The control input is restricted so that only one can fire at a time, given that both valves open will cancel the generated thrust.

7.1.2 Direct Feed

For one-dimensional motion the schematic for a direct feed system is shown in Figure 7.2. This is the least complex version of a cold gas system. With the nozzle attached directly to a pressure tank, the tank pressure becomes the thruster chamber pressure, and the thrust is directly dependent on the tank pressure state which decreases when used.

This system reduces the component complexity but it increases the order of state equations needed to determine optimal control. Again, using (4.2),(4.3),(4.4),(4.18)

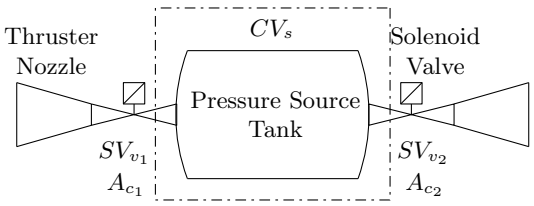

Figure 7.2: Direct feed cold gas propulsion schematic. The dot dash lines show control volumes. Each control volume and orifice is labeled and the nomenclature is given in Table 7.1.

and (4.10) for each component labeled in Figure 7.2, the model reduces to a system of two first order differential equations given as,

$$\dot{P}_s = \frac{RT_s}{V_s}\left(-\sum_{i=1}^{2}\dot{m}_{c_i}\right) \tag{7.2a}$$

$$\dot{m}_{c_i} = u_i A_{c_i} P_s \sqrt{\frac{\gamma}{RT_s}\left(\frac{2}{\gamma+1}\right)^{\frac{\gamma+1}{\gamma-1}}} \tag{7.2b}$$

where u_i is the solenoid control input for each thruster, $i = 1, 2$. Again, the control input is restricted so that only one can fire at a time.

7.1.3 Spacecraft Model

The one-dimensional motion of the spacecraft is governed by the following system

$$\begin{aligned} \dot{x}_1 &= x_2 \\ \dot{x}_2 &= F \end{aligned} \tag{7.3}$$

where x_1 is position, x_2 is velocity, and F is the thrust force. For the direct feed case, the thrust force is written in terms of the fuel pressure by substituting (4.6)-(4.10) into (4.11), as

$$F = u_i A_c \left[\left(\gamma M_e \left(\frac{2}{\gamma+1} \right)^{\frac{\gamma+1}{2(\gamma-1)}} \left(1 + \frac{\gamma-1}{2} M_e^2 \right)^{-\frac{1}{2}} \right. \right. \\ \left. \left. + \epsilon \left(1 + \frac{\gamma-1}{2} M_e^2 \right)^{-\frac{\gamma}{\gamma-1}} \right) P_s - \epsilon P_a \right] . \tag{7.4}$$

The closed loop pressure dynamics are obtained by substituting (7.2b) into (7.2a) to get

$$\dot{P}_s = -|u| A_c P_s \sqrt{\frac{\gamma R T_s}{V_s^2} \left(\frac{2}{\gamma+1} \right)^{\frac{\gamma+1}{\gamma-1}}} \tag{7.5}$$

where the control input, u is allowed to take one of three states,

$$u = \begin{cases} +1 & \text{for } u_1 = 1,\ u_2 = 0 \\ 0 & \text{for } u_1, u_2 = 0 \\ -1 & \text{for } u_2 = 1,\ u_1 = 0\ . \end{cases} \tag{7.6}$$

Introducing the thrust dynamics from (7.4) and (7.5), (7.3) is rewritten with P_s being denoted as x_3 in state space, as

$$\begin{aligned} \dot{x}_1 &= x_2 \\ \dot{x}_2 &= u f_1(x_3) \\ \dot{x}_3 &= -|u| f_2(x_3) \end{aligned} \tag{7.7}$$

where

$$f_1(x_3) = A_c \left(\left[\gamma M_e \left(\frac{2}{\gamma+1} \right)^{\frac{\gamma+1}{2(\gamma-1)}} \left(1 + \frac{\gamma-1}{2} M_e^2 \right)^{-\frac{1}{2}} + \epsilon \left(1 + \frac{\gamma-1}{2} M_e^2 \right)^{-\frac{\gamma}{\gamma-1}} \right] x_3 - \epsilon P_a \right) \tag{7.8}$$

$$f_2(x_3) = A_c x_3 \sqrt{\frac{\gamma R T_s}{V_s^2} \left(\frac{2}{\gamma+1} \right)^{\frac{\gamma+1}{\gamma-1}}} . \tag{7.9}$$

The control development in the following section will be based on the general class of systems as presented in (7.7).

7.2 Control Development

The spacecraft controller is designed for the direct feed case as presented in Section 7.1.3. The controller development method is first shown in general for a bilinear system. The control development is then applied to specific one-dimensional cases. Finally, the control development is investigated for a specific two dimensional case.

7.2.1 General Method

The general bilinear system is given in the form

$$\dot{\mathbf{x}} = A_k(u_k)\mathbf{x} \tag{7.10}$$

where $\mathbf{x} \in \mathbb{R}^n$, $u \in \mathbb{R}^m$, and $k = 1, \ldots, N$, where N is the number of discrete control states. System (7.10) is linear for each constant controller state k, and the differential

equation can be solved as

$$\mathbf{x}_{kf} = e^{A_k \Delta t_k} \mathbf{x}_{ki} \ . \tag{7.11}$$

To find the surface of points where the final control state N will drive the system to the final desired state $\mathbf{x}_{Nf} = \mathbf{x}_{\text{des}} = [0, \ldots, 0, x_{nf} \geq 0]$, solve the system (7.10) as

$$\mathbf{x}_{Ni}(\Delta t_N, x_{nf}) = (e^{A_N \Delta t_N})^{-1} \mathbf{x}_{Nf} \ . \tag{7.12}$$

The system (7.12) of parametric equations can be combined into a single equation eliminating the parameters Δt_N and x_{nf} in the form

$$\sigma_N(\mathbf{x}_{Ni}) = 0 \tag{7.13}$$

which is a manifold of points in state space where all trajectories end at $\mathbf{x}_{Nf}$ from any initial point on the manifold $\mathbf{x}_{Ni}$. The system (7.12) of parametric equations can also be combined to find the time spent in the final control state N as a function of the initial point on the manifold,

$$\Delta t_N(\mathbf{x}_{Ni}) \ . \tag{7.14}$$

To find the time spent in the previous control state $(N-1)$ from the initial point $\mathbf{x}_{(N-1)i}$ solve the system (7.10) for $\mathbf{x}_{(N-1)f}$ as

$$\mathbf{x}_{(N-1)f}(\Delta t_{(N-1)}, \mathbf{x}_{(N-1)i}) = e^{A_{(N-1)} \Delta t_{(N-1)}} \mathbf{x}_{(N-1)i} \ . \tag{7.15}$$

Since $\mathbf{x}_{(N-1)f} \equiv \mathbf{x}_{Ni}$, substitute (7.15) into (7.13) as $\sigma_N(\mathbf{x}_{(N-1)f}) = 0$ and solve for time as a function of the initial point as

$$\Delta t_{(N-1)i}(\mathbf{x}_{(N-1)i}) \; . \tag{7.16}$$

To find the time spent in the final control state N as a function of the initial point in control state $(N-1)$, substitute (7.15) into (7.14) as

$$\Delta t_N(\mathbf{x}_{(N-1)i}) \; . \tag{7.17}$$

To find the time spent in each control state N and $(N-1)$ as a function of the initial point in the next previous control state $(N-2)$, solve the system (7.10) for $\mathbf{x}_{(N-2)f}$ as

$$\mathbf{x}_{(N-2)f}(\Delta t_{(N-2)}, \mathbf{x}_{(N-2)i}) = e^{A_{(N-2)}\Delta t_{(N-2)}}\mathbf{x}_{(N-2)i} \; . \tag{7.18}$$

Since $\mathbf{x}_{(N-2)f} \equiv \mathbf{x}_{(N-1)i}$, substitute (7.18) into (7.16) as

$$\Delta t_{(N-1)}(\Delta t_{(N-2)}, \mathbf{x}_{(N-2)i}) \tag{7.19}$$

and substitute (7.18) into (7.17) as

$$\Delta t_N(\Delta t_{(N-2)}, \mathbf{x}_{(N-2)i}) \; . \tag{7.20}$$

If this is the first control state we can keep the initial time in the first control state as a free parameter. Therefore, the time spent in each of the control states N and $(N-1)$ is a function of the initial point in control state $(N-2)$ and the time spent

in the in the control state $(N-2)$. To minimize the total time from a given initial state, $\mathbf{x}_{(N-2)i}$, with the free parameter $\Delta t_{(N-2)}$, solve the following

$$\frac{d}{d\Delta t_{(N-2)}} \left(\sum_{k}^{N} \Delta t_k \right) \Bigg|_{\Delta t_{(N-2)=0}} = 0 \tag{7.21}$$

to get the manifold

$$\sigma_{(N-2)}(\mathbf{x}) = 0 \tag{7.22}$$

where (7.22) is the switching manifold that gives the time optimal state to switch from control $u_{(N-2)}$ to control $u_{(N-1)}$. The manifold (7.13) as function in state space written as

$$\sigma_N(\mathbf{x}) = 0 \tag{7.23}$$

is the switching manifold that gives the required state to switch from control $u_{(N-1)}$ to control u_N. The feedback control law is defined by these switching manifolds as

$$u = \begin{cases} u_{(N-2)} & , \quad \sigma_{(N-2)}(\mathbf{x}) > 0 \\ u_{(N-1)} & , \quad \sigma_{(N-2)}(\mathbf{x}) < 0 \text{ and } \sigma_N(\mathbf{x}) > 0 \\ u_N & , \quad \sigma_N(\mathbf{x}) < 0 \ . \end{cases} \tag{7.24}$$

7.2.2 One-Dimensional Motion

Consider a system of one-dimensional motion where the force applied in each direction depends of the amount of remaining fuel and actuating the thruster will cause the fuel to deplete. The state of the system is written as $\mathbf{x} = [x_1 \ x_2 \ x_3]^T$, where x_1 is position, x_2 is the velocity, and x_3 is the amount of fuel. In general the nonlinear

system of the form $\dot{\mathbf{x}} = f(\mathbf{x}, u)$ is written as

$$\begin{aligned} \dot{x}_1 &= x_2 \\ \dot{x}_2 &= u f_1(x_3) \\ \dot{x}_3 &= -|u| f_2(x_3) \end{aligned} \tag{7.25}$$

where $|u| \leq 1$ is the control input and $f_1(x_3)$ and $f_2(x_3)$ are nonlinear functions of the amount of remaining fuel. This system is representative of one-dimensional spacecraft motion for either translation or rotation with cold gas propulsion.

Translation The translational motion of an object is given as

$$m\ddot{x} = uF \tag{7.26}$$

where m is the mass and $|u| \leq 1$ is the control input. We define the state vector as $\mathbf{x} = [x_1 \; x_2 \; x_3]^T = [x \; \dot{x} \; p]^T$. As given in (4.19), the thrust force is $F(p) = C_1 p$ and the pressure rate of change is $\dot{p}(p) = -C_3 p$, where C_1 and C_3 are defined in (4.20). The state space equations for such a system are

$$\begin{aligned} \dot{x}_1 &= x_2 &&= x_2 \\ \dot{x}_2 &= u\tfrac{C_1}{m} p &&= u f_1(x_3) \\ \dot{x}_3 &= -|u| C_3 p &&= -|u| f_2(x_3) \end{aligned} \tag{7.27}$$

where $f_1(x_3) = \frac{C_1}{m} x_3$, and $f_2(x_3) = -C_3 x_3$.

Rotation The rotational motion of an object is given as

$$I\ddot{\theta} = u\tau \tag{7.28}$$

where $\tau = FR$ is the torque, $I = \frac{1}{2}mR^2$ is the moment of inertia of a disk, R is the radius of the disk, and $|u| \leq 1$ is the control input. We define the state vector as $\mathbf{x} = [x_1\ x_2\ x_3]^T = [\theta\ \dot{\theta}\ p]^T$. As given in (4.19), the thrust force is $F(p) = C_1 p$, and the pressure rate of change is $\dot{p}(p) = -C_3 p$, where C_1 and C_3 are defined in (4.20). The state space equations for such a system are

$$\begin{array}{rclcl} \dot{x}_1 & = & x_2 & = & x_2 \\ \dot{x}_2 & = & u\frac{2C_1}{mR}p & = & uf_1(x_3) \\ \dot{x}_3 & = & -|u|C_3 p & = & -|u|f_2(x_3) \end{array} \tag{7.29}$$

where $f_1(x_3) = \frac{2C_1}{mR}x_3$, and $f_2(x_3) = -C_3 x_3$.

If we let the constants be chosen as $C_1 = 1$, $C_2 = 1$, $m = 1$, and $R = 2$, both translation and rotation one dimensional motion can be simplified to the simplest example where $f_1(x_3) = f_2(x_3) = x_3$.

Simplest Example

To develop the method for determining the time optimal control law, the simplest form of (7.7) is used as an example where $f_1(x_3) = f_2(x_3) = x_3$. The non affine state

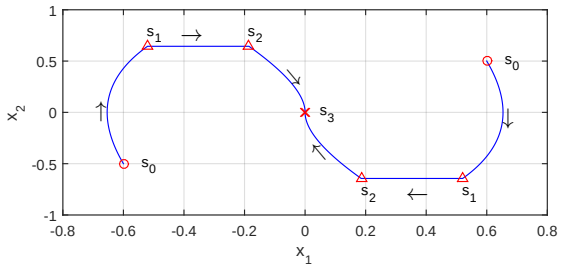

Figure 7.3: State space trajectories projected into the x_1x_2-plane with control switch points s_0, s_1, s_2, and s_3.

space model is

$$\begin{aligned} \dot{x}_1 &= x_2 \\ \dot{x}_2 &= ux_3 \\ \dot{x}_3 &= -|u|x_3 \ . \end{aligned} \tag{7.30}$$

The control input has three discrete possible states

$$u = \begin{cases} +1 & \text{for } k = 1 \\ 0 & \text{for } k = 2 \\ -1 & \text{for } k = 3 \end{cases} \tag{7.31}$$

which makes the model bilinear in the form $\dot{\mathbf{x}} = A\mathbf{x}$, for $\mathbf{x} = [x_1 \ x_2 \ x_3]^T$, where

$$A_{u_k} = \begin{bmatrix} 0 & 1 & 0 \\ 0 & 0 & -u_k \\ 0 & 0 & -|u_k| \end{bmatrix} \ . \tag{7.32}$$

The solution for this differential equation is $\mathbf{x}_f = e^{At_f}\mathbf{x}_i$. There are three possible trajectories, one for each controller state. Let Δt_+ be the time accelerating towards

$x_1 = 0$, the path from s_0 to s_1 as shown in Figure 7.3. Let Δt_0 be the time coasting towards $x_1 = 0$, the path from s_1 to s_2 as shown in Figure 7.3. Let Δt_- be the time decelerating towards $x_1 = 0$, the path from s_2 to s_3 as shown in Figure 7.3. For the region where $x_1 > 0$, these trajectories are

$$\mathbf{x}_1 = e^{A_{u_3}\Delta t_+}\mathbf{x}_0 \tag{7.33}$$

$$\mathbf{x}_2 = e^{A_{u_2}\Delta t_0}\mathbf{x}_1 \tag{7.34}$$

$$\mathbf{x}_3 = e^{A_{u_1}\Delta t_-}\mathbf{x}_2 \tag{7.35}$$

where $\mathbf{x}_0 = [x_{1_0}\ x_{2_0}\ x_{3_0}]^T$ is the initial system state at point s_0, $\mathbf{x}_1 = [x_{1_1}\ x_{2_1}\ x_{3_1}]^T$ is the system state at switching point s_1, $\mathbf{x}_2 = [x_{1_2}\ x_{2_2}\ x_{3_2}]^T$ is the system state at switching point s_2, and $\mathbf{x}_3 = [x_{1_3}\ x_{2_3}\ x_{3_3}]^T$ is the final system state at point s_3.

The goal is to drive the spacecraft from any initial position $x_1 = x_{10}$, to the desired position $x_1 = 0$. Therefore, to derive the optimal path, we begin at the origin, by finding the region such that applying deceleration at any point in the region will result in a trajectory that will cross the origin $(x_1, x_2 = 0)$. By rewriting (7.35) as $\mathbf{x}_2 = [e^{A_{u_+}\Delta t_-}]^{-1}\mathbf{x}_3$, where the final desired state is $\mathbf{x}_3 = [0\ ,\ 0\ ,\ x_{3_3} \geq 0]^T$, the system ending at point s_3 and beginning at s_2 is

$$\begin{aligned} x_{1_2} &= x_{3_3}\left(e^{\Delta t_-} - 1 - \Delta t_-\right) \\ x_{2_2} &= x_{3_3}\left(1 - e^{\Delta t_-}\right) \\ x_{3_2} &= x_{3_3}\left(e^{\Delta t_-}\right)\ . \end{aligned} \tag{7.36}$$

System (7.36) is a set of parametric equations that is manipulated to remove the

parameters x_{3_3}, and Δt_-, and written into one equation as

$$\sigma_2(\mathbf{x}) = x_1 + x_2 + (x_3 + x_2) \ln\left(\frac{x_3}{x_3 + x_2}\right) \tag{7.37}$$

where $\sigma_2(\mathbf{x}) = 0$ is a surface in state space such that decelerating from any point on that surface will pass through the desired final state. System (7.36) is also used to determine the time spent decelerating on that surface as

$$\Delta t_-(x_{2_2}, x_{3_2}) = \ln\left(\frac{x_{3_2}}{x_{3_2} + x_{2_2}}\right) . \tag{7.38}$$

Next, we look at the system coasting towards the surface $\sigma_2(\mathbf{x}) = 0$ from any point in the positive x_1 direction denoted by moving from point s_1 to s_2. Evaluating (7.34) results in the following parametric equations,

$$\begin{aligned} x_{1_2} &= x_{1_1} + x_{2_1}\Delta t_0 \\ x_{2_2} &= x_{2_1} \\ x_{3_2} &= x_{3_1} . \end{aligned} \tag{7.39}$$

The coasting time from point $\mathbf{x}_1$ to the surface $\sigma_2(\mathbf{x}_2) = 0$ is found by substituting (7.39) into (7.37) and solving for Δt_0. Similarly, the deceleration time is reevaluated as a function of $\mathbf{x}_1$ by substituting (7.39) into (7.38). The deceleration time and coasting time are given as functions of point $\mathbf{x}_1$ as

$$\Delta t_0(\mathbf{x}_1) = -\frac{1}{x_{2_1}}\left[x_{1_1} + x_{2_1} + (x_{3_1} + x_{2_1}) \ln\left(\frac{x_{3_1}}{x_{3_1} + x_{2_1}}\right)\right] \tag{7.40}$$

$$\Delta t_-(\mathbf{x}_1) = \ln\left(\frac{x_{3_1}}{x_{3_1} + x_{2_1}}\right) . \tag{7.41}$$

Lastly, we want to define the coasting and deceleration times as functions of the initial state $\mathbf{x}_0$, and the time, Δt_+, spent accelerating from point s_0 to s_1. The accelerating system is found by evaluating (7.33) as

$$\begin{aligned} x_{1_1} &= x_{1_0} + x_{2_0}\Delta t_+ - x_{3_0}\left(e^{-\Delta t_+} + \Delta t_+ - 1\right) \\ x_{2_1} &= x_{2_0} + x_{3_0}\left(e^{-\Delta t_+} - 1\right) \\ x_{3_1} &= x_{3_0}\left(e^{-\Delta t_+}\right) . \end{aligned} \tag{7.42}$$

By substituting (7.42) into (7.40) and (7.41) we get

$$\begin{aligned} \Delta t_0(\mathbf{x}_0, \Delta t_+) &= -\frac{1}{x_{2_0} + x_{3_0}(e^{-\Delta t_+} - 1)}\left[x_{1_0} + x_{2_0} + (x_{2_0} - x_{3_0})\Delta t_+ \right. \\ &\quad \left. + \left(x_{2_0} + x_{3_0}(2e^{-\Delta t_+} - 1)\right)\ln\left(\frac{x_{3_0}e^{-\Delta t_+}}{x_{2_0} + x_{3_0}(2e^{-\Delta t_+} - 1)}\right)\right] \quad (7.43) \\ \Delta t_-(\mathbf{x}_0, \Delta t_+) &= \ln\left(\frac{x_{3_0}e^{-\Delta t_+}}{x_{2_0} + x_{3_0}(2e^{-\Delta t_+} - 1)}\right) . \quad (7.44) \end{aligned}$$

The total time, Δt, from point s_0 to s_3 is the sum of the time spent in each leg written as

$$\Delta t(\mathbf{x}_0, \Delta t_+) = \Delta t_-(\mathbf{x}_0, \Delta t_+) + \Delta t_0(\mathbf{x}_0, \Delta t_+) + \Delta t_+ . \tag{7.45}$$

Note that the total time is dependent only on the initial position $\mathbf{x}_0$, and the time spent accelerating away from the initial point, Δt_+. The time optimal control goal is to minimize the total time using the only free parameter Δt_+.

To determine the time optimal surface for switching from accelerating to coasting, we analyze how the total time changes with a change in acceleration time and evaluate

at the boundary as

$$\left.\frac{d\Delta t}{d\Delta t_+}\right|_{\Delta t_+=0} = 0 \ . \tag{7.46}$$

This results in the switching surface

$$\sigma_0(\mathbf{x}) = \frac{x_3}{{x_2}^2}\left[x_1 + \frac{x_3 - x_2}{x_3 + x_2}x_2 + (x_3 - x_2)\ln\left(\frac{x_3}{x_3 + x_2}\right)\right] = 0 \ . \tag{7.47}$$

Note that for classical time optimal control the solution is bang-bang, where the control is constant acceleration and deceleration with no coasting. If this was the case, the analysis would have found $\sigma_0 \equiv \sigma_2$. However, in our case, we have found that it is always time optimal to coast for some time. This has to do with the nature of the system as the acceleration is dependent on the decreasing fuel source.

One more switching surface is required if the goal includes a desired minimum final fuel amount stated as $x_{3_f} \geq x_{3_{\min}}$. This is accomplished by analyzing the relation of $\frac{dx_2}{dx_3}$ from system (7.30) for decelerating towards the final state as

$$\int_{x_{2_0}=x_2}^{x_{2_f}=0} dx_2 = -\int_{x_{3_0}=x_3}^{x_{3_f}=x_{3_{\min}}} dx_3 \ . \tag{7.48}$$

The surface for switching from accelerating to coasting to arrive at the final state with a desired minimum fuel is

$$\sigma_1(\mathbf{x}) = x_3 - x_{3_{\min}} + x_2 = 0 \ . \tag{7.49}$$

To complete and combine the analysis for the region $x_1 < 0$, apply the transformation $(\cdot) \rightarrow -\text{sgn}(x_2)(\cdot)$ to $\{x_1, x_2, \sigma_0, \sigma_2\}$. Note that, $\text{sgn}(\cdot)\text{sgn}(\cdot) = 1$, and,

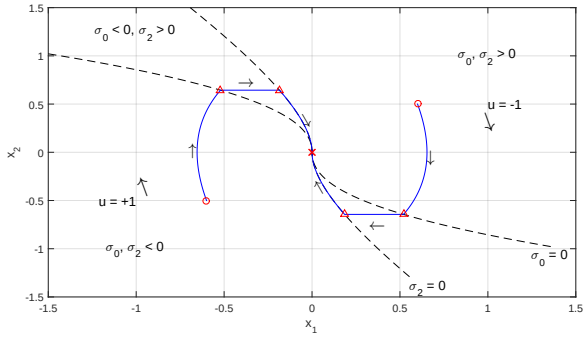

Figure 7.4: State space trajectories projected into the x_1x_2-plane. Trajectories shown for each of the three control states in relation to the switching surfaces. Switching surfaces σ_0 and σ_2 positive and negative regions shown.

$\text{sgn}(x_2)x_2 = |x_2|$. Each switching surface defined for all state space is written as

$$\sigma_0(\mathbf{x}) = \frac{x_3}{{x_2}^2}\left[x_1 + \frac{x_3 + |x_2|}{x_3 - |x_2|}x_2 - \text{sgn}(x_2)(x_3 + |x_2|)\ln\left(\frac{x_3}{x_3 - |x_2|}\right)\right] = 0 \tag{7.50}$$

$$\sigma_1(\mathbf{x}) = x_3 - x_{3_{\min}} - |x_2| = 0 \tag{7.51}$$

$$\sigma_2(\mathbf{x}) = x_1 + x_2 - \text{sgn}(x_2)(x_3 - |x_2|)\ln\left(\frac{x_3}{x_3 - |x_2|}\right) = 0\ . \tag{7.52}$$

A control law developed based on these switching surfaces is state feedback, time optimal, and fuel constrained.

The surfaces $\sigma_0(\mathbf{x}) = 0$ and $\sigma_2(\mathbf{x}) = 0$ have their positive and negative regions defined in Figure 7.4. The surface $\sigma_1(\mathbf{x}) = 0$ is defined as positive in the region above the surface in the positive x_3 direction. From this, the control law can be stated as

$$u = \begin{cases} -\frac{1}{2}[\text{sgn}(\sigma_0(\mathbf{x})) + \text{sgn}(\sigma_2(\mathbf{x}))] & \text{if } \sigma_1(\mathbf{x}) > 0 \\ -\frac{1}{2}[\text{sgn}(x_2) + \text{sgn}(\sigma_2(\mathbf{x}))] & \text{if } \sigma_1(\mathbf{x}) \leq 0\ . \end{cases} \tag{7.53}$$

From the analysis resulting in (7.51), in order to reach the origin, the desired remain-

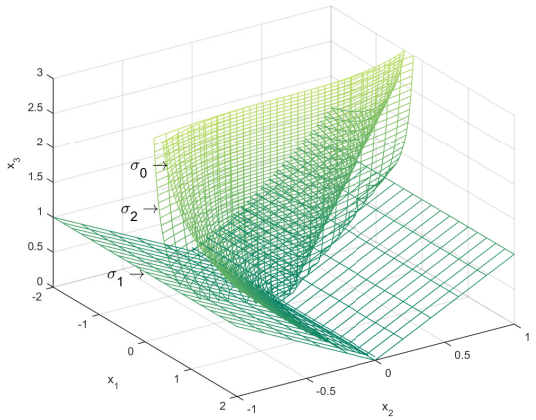

Figure 7.5: All three switching surfaces shown in three dimensional state space.

ing fuel $x_{3_{\min}}$ must be chosen within the range

$$0 \leq x_{3_{\min}} < x_{3_0} - |x_{2_0}| \tag{7.54}$$

where the origin is not accessible from the region

$$x_{3_0} - |x_{2_0}| < 0 \; . \tag{7.55}$$

A More General Example

We apply the general method to a one-dimensional motion example with linear functions $f_1(x_3) = ax_3$ and $f_2(x_3) = bx_3$, but keeping track of the linear coefficients a and b with the system written as

$$\begin{aligned} \dot{x}_1 &= x_2 \\ \dot{x}_2 &= uax_3 \\ \dot{x}_3 &= -|u|bx_3 \; . \end{aligned} \tag{7.56}$$

The system written in state space system is $\dot{\mathbf{x}} = A_{u_k}\mathbf{x}$ where the state vector is $\mathbf{x} = [x_1\ x_2\ x_3]^T$ and

$$A_{u_k} = \begin{bmatrix} 0 & 1 & 0 \\ 0 & 0 & -au_k \\ 0 & 0 & -b|u_k| \end{bmatrix} . \tag{7.57}$$

The deceleration trajectory to reach the final desired state $\mathbf{x}_3 = [0\ ,\ 0\ ,\ x_{3_3} \geq 0]^T$, is $\mathbf{x}_2 = [e^{A_{u_1}\Delta t_-}]^{-1}\mathbf{x}_3$ written out as

$$\begin{aligned} x_{1_2} &= \tfrac{a}{b^2}x_{3_3}\left(e^{b\Delta t_-} - 1 - b\Delta t_-\right) \\ x_{2_2} &= \tfrac{a}{b}x_{3_3}\left(1 - e^{b\Delta t_-}\right) \\ x_{3_2} &= x_{3_3}\left(e^{b\Delta t_-}\right) . \end{aligned} \tag{7.58}$$

This set of parametric equations manipulated to remove the parameters x_{3_3}, and Δt_- yields the deceleration switching surface

$$\sigma_2(x_1, x_2, x_3) = \frac{b^2}{a}(x_1 + x_2) + (x_3 + \frac{b}{a}x_2)\ln\left(\frac{x_3}{x_3 + \frac{b}{a}x_2}\right) = 0 . \tag{7.59}$$

The parametric equations also yield the deceleration time as

$$\Delta t_-(\mathbf{x}_2) = \frac{1}{b}\ln\left(\frac{x_{3_2}}{x_{3_2} + \frac{b}{a}x_{2_2}}\right) . \tag{7.60}$$

To determine the coasting time Δt_0, from the initial coasting state $\mathbf{x}_1$ to the surface $\sigma_2(\mathbf{x}) = 0$, substitute the coasting trajectory $\mathbf{x}_2 = e^{A_{u_2}\Delta t_0}\mathbf{x}_1$, into the switching

surface and solve for Δt_0 to yield

$$\Delta t_0(\mathbf{x}_1) = -\frac{1}{x_{2_1}}\left[(x_{1_1} + x_{2_1}) + \frac{1}{b^2}(ax_{3_1} + bx_{2_1})\ln\left(\frac{x_{3_1}}{x_{3_1} + \frac{b}{a}x_{2_1}}\right)\right] . \tag{7.61}$$

To determine the deceleration time as a function of initial coasting state $\mathbf{x}_1$, substitute the coasting trajectory equations into the deceleration time function $\Delta t_-(\mathbf{x}_2)$ to yield

$$\Delta t_-(\mathbf{x}_1) = \frac{1}{b}\ln\left(\frac{x_{3_1}}{x_{3_1} + \frac{b}{a}x_{2_1}}\right) . \tag{7.62}$$

To determine the deceleration and the coasting times as a function of the initial acceleration state $\mathbf{x}_0$ and the acceleration time Δt_+, substitute the acceleration trajectory equations $\mathbf{x}_1 = e^{A_{u_3}\Delta t_+}\mathbf{x}_0$ into the functions $\Delta t_0(\mathbf{x}_1)$ and $\Delta t_-(\mathbf{x}_1)$.

To minimize the total time

$$\Delta t(\mathbf{x}_0, \Delta t_+) = \Delta t_-(\mathbf{x}_0, \Delta t_0) + \Delta t_0(\mathbf{x}_0, \Delta t_0) + \Delta t_+ \tag{7.63}$$

with respect to the free parameter of acceleration time, solve the equation

$$\left.\frac{d\Delta t}{d\Delta t_+}\right|_{\Delta t_+ = 0} = 0 . \tag{7.64}$$

This results in the coasting switching surface

$$\sigma_0(\mathbf{x}) = \frac{ax_3}{b^2{x_2}^2}\left[b^2x_1 + \frac{ax_3 - bx_2}{ax_3 + bx_2}bx_2 + (ax_3 - bx_2)\ln\left(\frac{x_3}{x_3 + \frac{b}{a}x_2}\right)\right] = 0 . \tag{7.65}$$

The transformation to derive the surfaces for all space is $(\cdot) \rightarrow -\text{sgn}(x_2)(\cdot)$. The

switching surface for a system where $f_1(x_3) = ax_3$ and $f_2(x_3) = bx_3$ are given as

$$\sigma_2(\mathbf{x}) = \frac{b^2}{a}x_1 - \text{sgn}(x_2)\left[-\frac{b^2}{a}|x_2| + \left(x_3 - \frac{b}{a}|x_2|\right)\ln\left(\frac{x_3}{x_3 - \frac{b}{a}|x_2|}\right)\right] = 0 \tag{7.66}$$

$$\sigma_0(\mathbf{x}) = \frac{ax_3}{b^2{x_2}^2}\left[b^2x_1 + \frac{ax_3 + b|x_2|}{ax_3 - b|x_2|}bx_2 - \text{sgn}(x_2)(ax_3 + b|x_2|)\ln\left(\frac{x_3}{x_3 - \frac{b}{a}|x_2|}\right)\right] = 0\ . \tag{7.67}$$

Simulation

The model given in (7.30) using the control law given in (7.53) is simulated in MATLAB and Simulink with initial conditions $\mathbf{x}_0 = [0.6\ ,\ 0.5\ ,\ 2.5]^T$ and desired conditions $\mathbf{x}_{\text{des}} = [0\ ,\ 0\ ,\ x_{3_3} \geq 0]^T$.

Figure 7.6 shows the successful convergence of the position to the desired value using each of the three control states only once. There is an acceleration phase towards the origin, a coasting phase, and a deceleration phase to finally come to a stop at the origin. The total maneuver is completed with more fuel remaining than required.

7.2.3 Two-Dimensional Motion

We apply the general method to a two-dimensional motion example where thrust can be fired in both directions along two dimensions, but the trusters draw pressure from

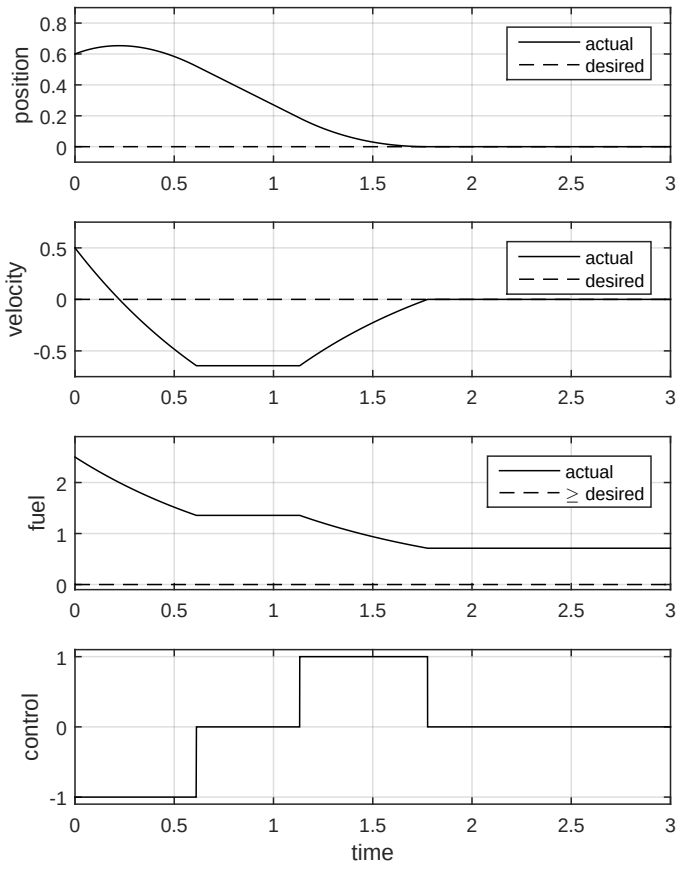

Figure 7.6: Time series of systems states and control input shows time optimal, bang-off-bang, control, placing the spacecraft at the desired position with the fuel remaining above its desired value.

the same tank. The system with state vector $\mathbf{x} = [x\ v_x\ y\ v_y\ p]^T$ is defined as

$$\begin{aligned} \dot{x} &= v_x \\ \dot{v}_x &= u_x f_1(p) \\ \dot{y} &= v_y \\ \dot{v}_y &= u_y f_1(p) \\ \dot{p} &= -(|u_x| + |u_y|) f_2(p)\ . \end{aligned} \tag{7.68}$$

where x is position in the x-direction, v_x is velocity in the x-direction, y is position in the y-direction, v_y is velocity in the y-direction, p is tank pressure, u_x is the control input for the x-direction, u_y is the control input for the y-direction. For the simple example we analyze the system for $f_1(p) = p$ and $f_2(p) = p$. For the given extremal control states $u_x = \{1,\ 0,\ -1\}$ and $u_y = \{1,\ 0,\ -1\}$, the number of possible control states is $N = 9$. However, rather than include all possible combinations we reduce the number of combined control states to $N = 5$ where either both are accelerating, one is accelerating, both are coasting, one is decelerating, or both are decelerating.

The bilinear model can be written as $\dot{\mathbf{x}} = A_{kl}\mathbf{x}$, where

$$A_{kl} = \begin{bmatrix} 0 & 1 & 0 & 0 & 0 \\ 0 & 0 & 0 & 0 & u_{x_k} \\ 0 & 0 & 0 & 1 & 0 \\ 0 & 0 & 0 & 0 & u_{y_l} \\ 0 & 0 & 0 & 0 & -(|u_{x_k}| + |u_{y_l}|) \end{bmatrix} \tag{7.69}$$

and where $k = 1, 2, 3$ and $l = 1, 2, 3$. If both directions are decelerating to the desired point $\mathbf{x}_{3_f} = [0\ 0\ 0\ 0\ p_f \geq 0]^T$ we can find the deceleration surface by solving $\mathbf{x}_{3_i} = [e^{A_{33}\Delta t_{33}}]^{-1}\mathbf{x}_{3_f}$

$$\begin{aligned} x &= -\tfrac{1}{2}p_f t + \tfrac{1}{4}p_f e^{2t} - \tfrac{1}{4}p_f \\ v_x &= -\tfrac{1}{2}p_f e^{2t} + \tfrac{1}{2}p_f \\ y &= -\tfrac{1}{2}p_f t + \tfrac{1}{4}p_f e^{2t} - \tfrac{1}{4}p_f \\ v_y &= -\tfrac{1}{2}p_f e^{2t} + \tfrac{1}{2}p_f \\ p &= p_f e^{2t}\ . \end{aligned} \tag{7.70}$$

This set of parametric equations cannot uniquely be manipulated to remove the pa-

rameter t. There are two solutions to remove the parameters where one is strictly in terms of the x-direction and one is strictly in terms of the y-direction. The decelerating surfaces are

$$\begin{aligned} \sigma_{33} &= 4x - 2v_x - (p + 2v_x)\ln\left(\tfrac{p}{p+2v_x}\right) = 0 \\ \sigma_{33} &= 4y - 2v_y - (p + 2v_y)\ln\left(\tfrac{p}{p+2v_y}\right) = 0 \end{aligned} \tag{7.71}$$

and the time spent decelerating on these surfaces are

$$\begin{aligned} t_{33} &= \tfrac{1}{2}\ln\left(\tfrac{p}{p+2v_x}\right) \\ t_{33} &= \tfrac{1}{2}\ln\left(\tfrac{p}{p+2v_y}\right) \ . \end{aligned} \tag{7.72}$$

Since these are separate surfaces, one for each of the x and y directions, if one reaches the origin before the other, the system needs to be solved for one direction decelerating and one direction stationary. We solve the equation $\mathbf{x}_{3_i} = [e^{A_{32}\Delta t_{32}}]^{-1}\mathbf{x}_{3_f}$ for $\mathbf{x}_{3_f} = [0\ 0\ 0\ 0\ p_f \geq 0]^T$ as

$$\begin{aligned} x &= -p_f t + p_f e^t - p_f \\ v_x &= -p_f e^t + p_f \\ y &= 0 \\ v_y &= 0 \\ p &= p_f e^t \ . \end{aligned} \tag{7.73}$$

This decelerating surface is now equivalent to the one-dimensional case as

$$\sigma_{32} = x - v_x - (p + v_x)\ln\left(\frac{p}{p + v_x}\right) = 0 \tag{7.74}$$

with the time spent decelerating as

$$t_{32} = \ln\left(\frac{p}{p + v_x}\right) . \tag{7.75}$$

The two switching surfaces, σ_{33} and σ_{32}, provide a state feedback opportunity for when to decelerate for either one or two dimensions. The switching surfaces are shown in Figure 7.7 for one direction. The state space trajectory for each direction is

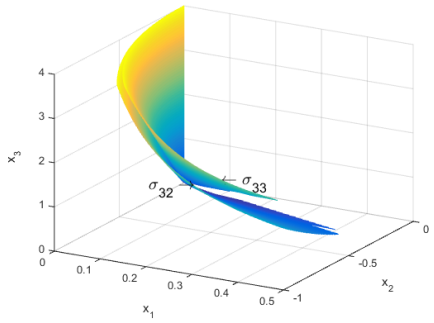

Figure 7.7: Decelerating switching surfaces for one direction. σ_{33} for both directions decelerating and σ_{32} is for only one direction decelerating. x_1 and x_2 are the position and velocity superimposed for either x or y directions. x_3 is the fuel for thrust in both directions.

shown in Figure 7.8. Here, the initial conditions are different for x and y directions so that the initial x is further from the desired position. As both brake, the trajectory of each moves along the σ_{33} surface. When the desired y position is reached, the thrust in that direction is set to zero. This changes the rate of fuel decay, so if the thrust continues in the x direction, it will arrive short of the desired position. Because there is only error in the x direction, the σ_{32} can be used as the braking surface. The x direction control will have to coast to first reach σ_{32}, and then it can continue to

brake until it reaches the desired position.

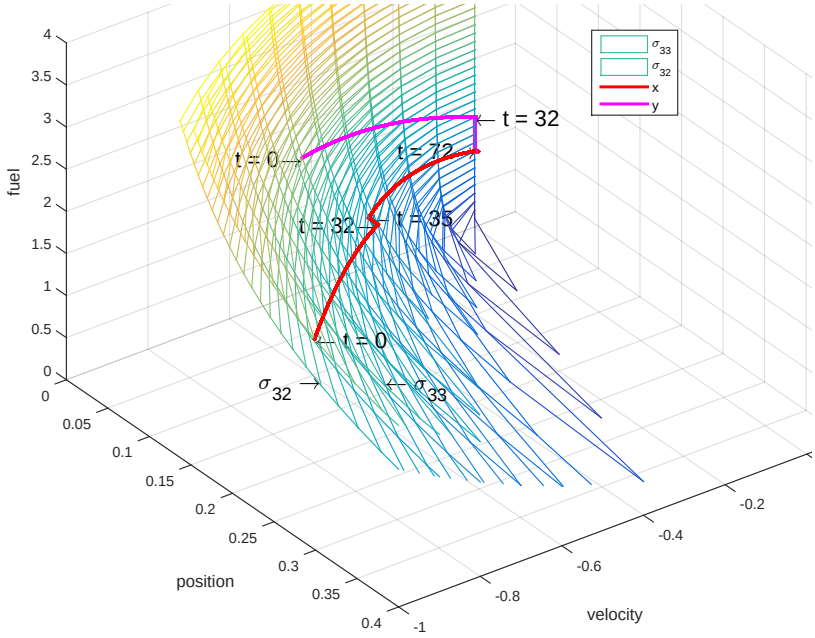

Figure 7.8: State space trajectories for x and y directions are superimposed on switching surfaces σ_{33} and σ_{32}.

The investigation stops here with a way to have state feedback for control in two dimensions of a system with decreasing thrust. Because the deceleration surface is not a function of all states, it is not clear how to derive the total time as a function of all initials conditions. Therefore, it is not clear if a time optimal solution can be found for the two-dimensional case.

7.3 Conclusions and Future Work

Cold gas propulsion is a viable system for many spacecraft, including the reduced complexity of the direct feed configuration. This system provided the motivation to analyze such class of systems where the remaining fuel directly impacted the control

thrust that could be applied. The results showed that it is possible to develop a time optimal state feedback control law for such a system.

Classical time optimal analysis for a system with constant thrust results in a bang-bang control profile with one switching point from acceleration to deceleration. Classical fuel optimal analysis for a constant thrust system results in a bang-off-bang control profile for acceleration, coasting, and then deceleration. However, optimal analysis for the direct feed system found that the switching surface for bang-bang was neither time optimal nor fuel optimal. It turned out that a coasting period was always time optimal, so a second surface was derived to find the time optimal coasting region. Consequently, by shifting from bang-bang to bang-off-bang, total fuel used was also reduced as well as the total time.

Future work includes generalizing the control development method in terms of any functions $f_1(x_3)$ and $f_2(x_3)$ for system (7.7), including linear and nonlinear functions, and expanding the optimal feedback control for spacecraft attitude and translation control in all three dimensions.

Chapter 8

Conclusion

An investigation was done into control of spacecraft with small thrust input and into thrust control of cold gas propulsion systems. Several control algorithms were designed and tested for such systems. For spacecraft with small continuous thrust, it was successfully that robust feedback control of a spacecraft for orbital maneuvers is possible. For spacecraft with cold gas propulsion systems, a full system fluid model was developed along with several control algorithms for thrust control. Nonlinear feedback controllers were designed and tested in simulation to track desired thrusts for several thrusters in a full cold gas propulsion system given measurements of only the pressure states of the system. For a spacecraft where the thrust is dependent on a depleting fuel source, a time optimal feedback controller was designed and tested in simulation to drive the spacecraft to a desired position. It was interesting to learn that the time optimal solution for such a system included a coasting stage, which is not found in classical optimal control.

The research for small thrust orbital control could continue by applying the con-

trol laws to multidimensional orbital trajectories, and investigating optimal control opportunities. Cold gas propulsion systems could be improved by investigating other control actuators and other cold gas propellant storage options to improve fuel efficiency. Future work for the direct feed cold gas propulsion is to apply the control method to multidimensional attitude and translation control.

References

Anis, A. (2012). Cold Gas Propulsion System An Ideal Choice for Remote Sensing Small Satellites. In B. Escalante (Ed.), *Remote sensing - advanced techniques and platforms* (chap. 20). InTech. Retrieved from http://www.intechopen.com/books/remote-sensing-advanced-techniques-and-platforms/cold-gas-propulsion-system-an-ideal-choice-for-remote-sensing-small-satellites doi: 10.5772/37149

Artstein, Z. (1983, jan). Stabilization with relaxed controls. *Nonlinear Analysis: Theory, Methods & Applications*, *7*(11), 1163–1173. Retrieved from http://linkinghub.elsevier.com/retrieve/pii/0362546X83900494 doi: 10.1016/0362-546X(83)90049-4

Åström, K., & Furuta, K. (2000, feb). Swinging up a pendulum by energy control. *Automatica*, *36*(2), 287–295. Retrieved from http://linkinghub.elsevier.com/retrieve/pii/S0005109899001405 doi: 10.1016/S0005-1098(99)00140-5

Barral, S., Miedzik, J., & Ahedo, E. (2008). A model for the active control of low frequency oscillations in Hall thrusters. *44th Joint Propulsion Conference*(July), 1–9. Retrieved from http://pag.ifpilm.pl/publi/AIAA{_}2008{_}4632.pdf

Barucci, M. a., Yoshikawa, M., Michel, P., Kawagushi, J., Yano, H., Brucato, J. R., ... Ulamec, S. (2008, apr). MARCO POLO: near earth object sample return mission. *Experimental Astronomy*, *23*(3), 785–808. Retrieved from `http://link.springer.com/10.1007/s10686-008-9087-8` doi: 10.1007/s10686-008-9087-8

Battin, R. H. (1999). *An Introduction to the Mathematics and Methods of Astrodynamics* (Revised ed.). American Institute of Aeronautics and Astronautics.

Benson, T. (Ed.). (2014). *The Beginner's Guide to Rockets.* NASA GRC. Retrieved 2014, from `http://exploration.grc.nasa.gov/education/rocket/rktthsum.html`

Betts, J. T., & Erb, S. O. (2003, jan). Optimal Low Thrust Trajectories to the Moon. *SIAM Journal on Applied Dynamical Systems*, *2*(2), 144–170. Retrieved from `http://epubs.siam.org/doi/abs/10.1137/S1111111102409080` doi: 10.1137/S1111111102409080

Bombardelli, C., & Peláez, J. (2011a, jul). Ion Beam Shepherd for Asteroid Deflection. *Journal of Guidance, Control, and Dynamics*, *34*(4), 1270–1272. Retrieved from `http://arc.aiaa.org/doi/abs/10.2514/1.51640` doi: 10.2514/1.51640

Bombardelli, C., & Peláez, J. (2011b, may). Ion Beam Shepherd for Contactless Space Debris Removal. *Journal of Guidance, Control, and Dynamics*, *34*(3), 916–920. Retrieved from `http://arc.aiaa.org/doi/abs/10.2514/1.51832` doi: 10.2514/1.51832

Brophy, J., Ganapathi, G., Garner, C., & Gates, J. (2004). Status of the Dawn Ion Propulsion System. *40th Joint Propulsion Conference*. Retrieved from `http://arc.aiaa.org/doi/pdf/10.2514/6.2004-3433`

Brophy, J., Marcucci, M., Ganapathi, G., Gates, J., & Garner, C. (2005). Implementation of the Dawn Ion Propulsion System. *41st Joint Propulsion Conference*. Retrieved from `http://trs-new.jpl.nasa.gov/dspace/handle/2014/38349`

Brophy, J. R. (2002). Nasa's Deep Space 1 Ion Engine. *Review of Scientific Instruments*, *73*(2), 1071–1078. doi: 10.1063/1.1432470

Choueiri, E. Y. (2001). Fundamental difference between the two Hall thruster variants. *Physics of Plasmas*, *8*(11), 5025. Retrieved from `http://link.aip.org/link/PHPAEN/v8/i11/p5025/s1{&}Agg=doi` doi: 10.1063/1.1409344

Cornu, N., Marchandise, F., Darnon, F., & Estublier, D. (2007). The PPS ® 1350-G Qualification Demonstration : 10500 hrs on the Ground and 5000 hrs in Flight. *43rd Joint Propulsion Conference*.

Curtis, H. D. (2005). *Orbital Mechanics for Engineering Students* (First ed.). Else.

Darnon, F., Arrat, D., D'Escrivan, S., Chesta, E., & Pillet, N. (2007). An overview of Electric Propulsion activities in France. *43rd Joint Propulsion Conference*.

DARPA. (2008). *DARPA DMACE Challenge.* Retrieved 2017-02-01, from `http://archive.darpa.mil/dmace/PhotoGallery/CUBESAT.JPG`

DeCarlo, R. A., Zak, S., & Drakunov, S. V. (2010). Variable Structure, Sliding-Mode Controller Design. In *The control handbook: a volume in the electrical engineering handbook series* (pp. 50.1–50.21). CRC Press, Inc.

Drakunov, S. (1992). Sliding-mode observers based on equivalent control method. *Decision and Control, 1992., Proceedings of the ...* (9), 2368–2369. Retrieved from `http://ieeexplore.ieee.org/xpls/abs{_}all.jsp?arnumber=371368`

Drakunov, S., Hanchin, G., Su, W., & Özgüner, Ü. (1997). Nonlinear control of a rodless pneumatic servoactuator, or sliding modes versus Coulomb friction.

Automatica, *33*(97), 1401–1408. Retrieved from http://www.sciencedirect.com/science/article/pii/S0005109897000150

Drakunov, S. V. (1993). Sliding Mode Control of the Systems with Uncertain Direction of Control Vector. In *Proceedings of the 32nd ieee conference on decision and control (cdc)* (pp. 2477–2478). December 15-17, San Antonio, Texas.

Drakunov, S. V. (2008). Feedback Concept Using Controlled Virtual Point Following. In *proceedings of the aas/aiaa space flight mechanics meeting.* Galveston, Texas: Univelt, Inc.

Emelyanov, S. (1967). *Variable Structure Control Systems.* Nauka, Moscow (in Russian).

Faubourg, L., & Pomet, J.-B. (2000). Control Lyapunov Functions for Homogeneous "Jurdjevic-Quinn" Systems. *ESAIM: Control, Optimisation and Calculus of Variations*, *5*(June), 293–311. Retrieved from http://www.esaim-cocv.org/article{_}S1292811900001123 doi: 10.1051/cocv:2000112

Filippov, A. F. (1988). *Differential Equations with Discontinuous Righthand Sides* (Vol. 18; F. M. Arscott, Ed.). Dordrecht: Springer Netherlands. Retrieved from http://link.springer.com/10.1007/978-94-015-7793-9 doi: 10.1007/978-94-015-7793-9

Függe-Lotz, I. (1953). *Discontinuous Automatic Control.* Princton University Press.

Furumo, J. G. (2013). *Cold-gas Propulsion for Small Satellite Attitude Control, Station Keeping, and De-orbit* (Tech. Rep.). University of Hawaii at Mnoa. Retrieved from http://www.spacegrant.hawaii.edu/fellowshipsS2013.html

Garner, C., & Rayman, M. (2010). In-flight operation of the dawn ion propulsion system: Status at one year from the vesta rendezvous. *46th Joint Propulsion*

Conference. Retrieved from http://arc.aiaa.org/doi/pdf/10.2514/6.2010-7111

Gurfil, P. (2007, apr). Nonlinear feedback control of low-thrust orbital transfer in a central gravitational field. *Acta Astronautica*, *60*(8-9), 631–648. Retrieved from http://linkinghub.elsevier.com/retrieve/pii/S0094576506003742 doi: 10.1016/j.actaastro.2006.10.001

Jurdjevic, V., & Quinn, J. (1978, jun). Controllability and stability. *Journal of Differential Equations*, *28*(3), 381–389. Retrieved from http://linkinghub.elsevier.com/retrieve/pii/0022039678901353 doi: 10.1016/0022-0396(78)90135-3

Kamran, N. N. (2016). *Sliding Mode Observers for Distributed Parameter Systems: Theory and Applications* (Unpublished doctoral dissertation). Embry-Riddle Aeronautical university.

Kellett, C., & Praly, L. (2004). Nonlinear control tools for low thrust orbital transfer. *Proceedings of the 6th IFAC Symposium on Nonlinear Control Systems*, *1*, 79–86. Retrieved from http://onlinelibrary.wiley.com/doi/10.1002/cbdv.200490137/abstracthttp://w.sigpromu.org/reports/Document709.pdf

Kienitz, K. H., & Bals, J. (2005). Pulse modulation for attitude control with thrusters subject to switching restrictions. *Aerospace Science and Technology*, *9*(7), 635–640. doi: 10.1016/j.ast.2005.06.006

Kirk, D. E. (2004). *Optimal Control Theory: An Introduction*. Mineola, New York: Dover Publications.

Kitchen-McKinley, S. J., Drakunov, S. V., Mueller, R. P., & DuPuis, M. A. (2016). Modeling and Control of Cold Gas Propulsion for Spacecraft Attitude Control.

In *Asce earth and space.* Orlando, FL: ASCE.

Komurasaki, K., & Kuninaka, H. (2007). An Overview of Electric Propulsion Activities in Japan. *43rd Joint Propulsion Conference*. Retrieved from http://erps.spacegrant.org/uploads/images/images/iepc{_}articledownload{_}1988-2007/2003index/0339-0303iepc-full.pdf

Koppel, C. R., Marchandise, F., Prioul, M., Estublier, D., & Darnon, F. (2005). The SMART-1 Electric Propulsion Subsystem. *41st Joint Propulsion Conference*.

Kvell, U., Puusepp, M., Kaminski, F., Past, J.-E., Palmer, K., Grönland, T.-A., & Noorma, M. (2014). Nanosatellite orbit control using MEMS cold gas thrusters. *Proceedings of the Estonian Academy of Sciences*, *63*(2S), 279–285. Retrieved from http://www.scopus.com/inward/record.url?eid=2-s2.0-84901312579{&}partnerID=tZOtx3y1 doi: 10.3176/proc.2014.2S.09

Louwerse, M. C. (2009). *Cold gas micro propulsion* (Thesis, University of Twente, Enschede, The Netherlands). doi: 10.3990/1.9789036529037

Lu, E. T., & Love, S. G. (2005, nov). Gravitational tractor for towing asteroids. *Nature*, *438*, 177–178. Retrieved from http://www.ncbi.nlm.nih.gov/pubmed/16281025 doi: 10.1038/438177a

Makled, A. E., AL-Sanabawy, M. A., & Bakr, M. A. (2009). Theoretical and Experimental Evaluation of Cold Gas System Components. In *Aerospace sciences & aviation technology* (pp. 1–17).

Mueller, J., Hofer, R., & Ziemer, J. (2010). Survey of propulsion technologies applicable to cubesats. In *Joint army-navy-nasa-air force (jannaf)* (pp. 1–58). Colorado Springs, Colorado: Jet Propulsion Laboratory, National Aeronautics

and Space Administration. Retrieved from http://trs-new.jpl.nasa.gov/dspace/handle/2014/41627

Polk, J., Kakuda, R., Anderson, J., & Brophy, J. (1999). Validation of the NSTAR ion propulsion system on the Deep Space One mission: overview and initial results. *Joint Propulsion Conference Los Angeles, California, USA*. Retrieved from http://trs-new.jpl.nasa.gov/dspace/handle/2014/17734

Rayman, M., Varghese, P., Lehman, D., & Livesay, L. (2000). Results from the Deep Space 1 technology validation mission. *Acta Astronautica*, *47*(2-9), 475–487. Retrieved from http://www.sciencedirect.com/science/article/pii/S0094576500000874

Ross, I. M., Gong, Q., & Sekhavat, P. (2007, jul). Low-Thrust, High-Accuracy Trajectory Optimization. *Journal of Guidance, Control, and Dynamics*, *30*(4), 921–933. Retrieved from http://arc.aiaa.org/doi/abs/10.2514/1.23181 doi: 10.2514/1.23181

Sanders, G., Larson, W., Sacksteder, K., & Mclemore, C. (2008). NASA In-Situ Resource Utilization (ISRU) Project: Development and Implementation. *AIAA SPACE 2008 Conference & Exposition*(September), 1–16. Retrieved from http://arc.aiaa.org/doi/abs/10.2514/6.2008-7853 doi: 10.2514/6.2008-7853

Sanders, G. B., & Larson, W. E. (2013). Progress Made in Lunar In Situ Resource Utilization under NASA ' s Exploration Technology and Development Program. *Journal of Aerospace Engineering*, *26*(1), 5–17. doi: 10.1061/(ASCE)AS.1943-5525.0000208.

Schaub, H., & Junkins, J. L. (2003). *Analytical Mechanics of Space Systems*. American

Institute of Aeronautics and Astronautics.

Sengupta, A., Anderson, J. a., Garner, C., Brophy, J. R., Groh, K. D., Banks, B., & Karniotis, T. a. (2009, jan). Deep Space 1 Flight Spare Ion Thruster 30,000-Hour Life Test. *Journal of Propulsion and Power*, *25*(1), 105–117. Retrieved from `http://arc.aiaa.org/doi/abs/10.2514/1.36549` doi: 10.2514/1.36549

Sontag, E. D. (1989, jan). A universal' construction of Artstein's theorem on nonlinear stabilization. *Systems & Control Letters*, *13*(2), 117–123. doi: 10.1016/0167-6911(89)90028-5

Sridhar, K., Finn, J., & Kliss, M. (2000, jan). In-situ resource utilization technologies for Mars life support systems. *Advances in Space Research*, *25*(2), 249–255. Retrieved from `http://linkinghub.elsevier.com/retrieve/pii/S0273117799009552` doi: 10.1016/S0273-1177(99)00955-2

Stich, S. (2013). *Asteroid Redirect Mission and Human Space Flight Briefing to National Research Council Committee for Study on Human Space Flight Technical Panel.*

Sutton, G. P., & Biblarz, O. (2001). *Rocket Propulsion Elements* (Seventh ed.). Wiley-Interscience.

Thorne, J. (1996). *Optimal Continuous-Thrust Orbit Transfers.* (Doctoral Dissertation, Airforce Institute of Technology). Retrieved from `http://oai.dtic.mil/oai/oai?verb=getRecord{&}metadataPrefix=html{&}identifier=ADA314771`

Utkin, V. I. (1977). Variable structure systems with sliding modes. *IEEE Transactions on Automatic Control*, *22*(2), 212–222. doi: 10.1109/TAC.1977.1101446

Utkin, V. I. (1978). *Sliding Modes and their Application in Variable Structure Systems*. MIR Publishers.

Utkin, V. I. (1992). *Sliding Modes in Control and Optimization*. Berlin, Heidelberg: Springer Berlin Heidelberg. Retrieved from http://link.springer.com/10.1007/978-3-642-84379-2 doi: 10.1007/978-3-642-84379-2

VACCO. (2014). *NASA C-POD Micro Propulsion System Data Sheet*. Retrieved 2017-02-01, from http://www.cubesat-propulsion.com/reaction-control-propulsion-module/

Wie, B. (2008). *Space Vehicle Dynamics and Control* (Second Edi ed.). American Institute of Aeronautics and Astronautics.

Wiesel, W., & Alfano, S. (1985). Optimal many-revolution orbit transfer. *Journal of Guidance, Control, and Dynamics*, 155–157. Retrieved from http://arc.aiaa.org/doi/pdf/10.2514/3.19952

Zagaris, C. (2012). *Trajectory Control and Optimization for Responsive Spacecraft* (Master's Thesis, Airforce Institute of Technology). Retrieved from http://oai.dtic.mil/oai/oai?verb=getRecord{&}metadataPrefix=html{&}identifier=ADA558201